ABSTRACT

Title of thesis: ROBOTIC SIMULATION OF FLEXIBLE-BODY
                     SPACECRAFT DYNAMICS IN A SATELLITE
                     SERVICING TESTBED

                     Justin Cory Brannan
                     Master of Science, 2014

Thesis directed by: Dr. Craig Carignan
                     Department of Aerospace Engineering

Satellite failures that once led to end-of-life may eventually be addressed using robotic servicing platforms. The ability to model and simulate the physical interaction between two free-floating spacecraft is a key aspect of robotic servicing, and understanding how large appendages such as solar panels, antenna arrays and booms affect the combined system dynamics may be critical to mission operations. This research presents a model of the coupled rigid- and flexible-body satellite dynamics that can be implemented on a robotic satellite simulator. The coupled dynamics are validated against a commercially available dynamics software package, and robot hardware-in-the-loop tests are conducted to demonstrate how the dynamics model is able to predict the response of a robot mass simulator outfitted with physical appendages. Through both validation efforts, a flexible-body simulation is developed to observe the resulting dynamics of a given satellite system on-orbit.

ROBOTIC SIMULATION OF FLEXIBLE-BODY SPACECRAFT DYNAMICS IN A SATELLITE SERVICING TESTBED

by

Justin Cory Brannan

Thesis submitted to the Faculty of the Graduate School of the
University of Maryland, College Park in partial fulfillment
of the requirements for the degree of
Master of Science
2014

Advisory Committee:
Research Associate Professor Dr. Craig Carignan, Chair
Associate Professor Dr. David Akin
Department Chair Dr. Norman Wereley

Acknowledgments

I would like to thank Dr. David Akin for providing such a unique environment at the Space Systems Laboratory, which has fueled my curiosity within the aerospace field over the past six years. Without his support of this project under the METS II contract, none of the research proposed in this thesis would be possible. A special thank you also goes to Dr. Norman Wereley for his support of this research and for personally visiting NASA to experience first-hand the technology I have been developing over the past two years.

An immense amount of thanks goes to my advisor, Dr. Craig Carignan who has truly gone above and beyond to help make this research effort what it is today. From conception to final correlation efforts, Craig has been there every step of the way for advice on any technical, career or logistic matters over the past couple of years. I could not have asked for a more passionate and ambitious mentor to help bridge the gap between the Space Systems Laboratory and NASA Goddard Space Flight Center (GSFC).

A sincere thank you also goes out to the many people who supported my research at NASA's Satellite Servicing Capabilities Office. First and foremost, support from Brian Roberts has been instrumental in forming a successful research project and developing the connection between the University of Maryland and NASA GSFC. The initial project proposal stemmed from a concern about the initial interaction between spacecraft, first introduced by Bo Naasz, for which I am also thankful. A great deal of thanks also goes to the entire Robotic Demonstration

Table of Contents

List of Figures

Nomenclature

M_{system}	Total mass matrix of a system
M_{hub}	Mass matrix describing a rigid-body satellite hub
M_{flex}	Mass matrix describing a particular flexible-body appendage
Q_{system}	Total quadratic velocity vector of a system
Q_{hub}	Quadratic velocity vector describing a rigid-body satellite hub
Q_{flex}	Quadratic velocity vector describing a particular flexible-body appendage
$\bar{u}_{input}$	Input forces and torques experienced by the client satellite, in body frame
$\bar{F}_{ext}$	External force experienced by the client vehicle, in body frame
$\bar{T}_{ext}$	External torque experienced by the client vehicle, in body frame
$\bar{Q}_{ext}$	External modal force experienced by the client vehicle, in body frame
$\ddot{\bar{x}}$	Second derivative of the client satellite's state, in body frame
m_s	Mass of rigid-body satellite hub
I_{3x3}	Identity matrix (3x3)
$\tilde{\bar{r}}_{cm_s}$	Cross product matrix form of satellite hub center of mass, in body frame
I_{o_s}	Area moment of inertia of satellite hub, about satellite center of mass
w_s	Angular velocity of satellite hub
r	Position of a point on a deformable body, represented in inertial frame
R	Vector location of the body coordinate system origin, in inertial frame
A	Rotation matrix from inertial frame to body frame
$\bar{u}$	Position of a point on a flexible-body, relative to the body frame origin
$\bar{u}_o$	Undeformed position of a point on a flexible-body, expressed in body frame
$\bar{u}_f$	Deformed position of a point on a flexible-body, expressed in body frame
S	Mode shape matrix, describing the deformation of a flexible-body
q_f	Modal degree-of-freedom of a flexible-body
b	Damping matrix describing a flexible-body
k_{ff}	Stiffness matrix describing a flexible-body
EI	Structural rigidity of a flexible-body
L_a	Length of a satellite appendage
ϕ	Mode shape description of a particular type of deformation of a flexible-body
m_{eff}	Effective system mass, used to calculate damping
w_{n_i}	Natural frequency of mode i, for a given type of deformation
x_a	Distance along the length of an appendage
$f_{i_{<Hz>}}$	Frequency of mode i, provided in Hz
μ_a	Mass of an appendage divided by its length
L_s	Satellite hub length
$I_{o_{prin}}$	Principal axes of inertia, about the object's center of mass
δ_{tip}	Static deflection of the appendage tip
$F_{tipmass}$	Effective force of a mass being hung from the tip of an appendage
ζ	Damping ratio value used to describe the damped response of a flexible-body
x_{peak}	Peak magnitude, used in calculation of damping ratio

List of Abbreviations

RRM	Robotic Refueling Mission
DARPA	Defense Advanced Research Projects Agency
SSCO	Satellite Servicing Capabilities Office
NASA	National Aeronautics and Space Administration
GSFC	Goddard Space Flight Center
COFS	Control of Flexible Structures
MMS	Magnetospheric Multiscale Mission
SCOLE	Spacecraft Control Laboratory Experiment
FEM	Finite Element Method
GOES	Geostationary Operational Environmental Satellite
NASTRAN	NASA Structure Analysis
ADAMS	Automated Dynamic Analysis of Mechanical Systems
DOF	Degree-of-freedom
MATLAB	Matrix Laboratory
TDRSS	Tracking and Data Relay Satellite System
RDT	Robotic Demonstration and Testing
HIL	Hardware-in-the-loop

Chapter 1: Introduction

1.1 Motivation

NASA's Robotic Refueling Mission (RRM), deployed on the International Space Station, is currently demonstrating how to refuel satellites that were not intended to be serviced. This capability would have the potential to repair disabled satellites that are otherwise beyond the reach of human servicing, extending the life of current spacecraft. Other organizations, such as the Defense Advanced Research Projects Agency (DARPA) and the Japanese, German and Canadian space agencies, are conducting similar flight experiments, realizing the potential to drastically reduce the total cost of future endeavors and increase both the reliability and safety of access to space.

Performed under the Satellite Servicing Capabilities Office (SSCO) at NASA Goddard Space Flight Center, this research aims to offset the costs of follow-on spacecraft by overcoming failures, such as the depletion of fuel, that can lead to satellite end-of-life. To accomplish this task, it is necessary to study how multiple spacecraft, such as a robotic servicer and client satellite, would interact on-orbit. Although RRM currently utilizes the International Space Station's Dextre robotic arm to manipulate a series of interfaces resembling actual client satellites, one even-

tual goal might be to launch a free-flying robotic vehicle similar to that shown in Figure 1.1 that could perform repair and refueling tasks on-orbit.
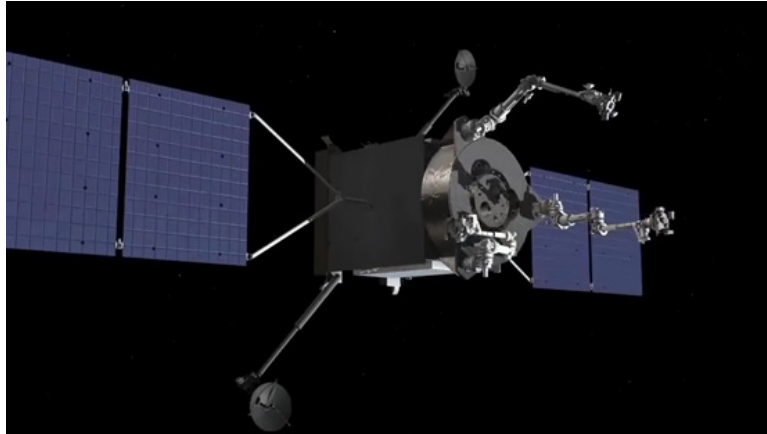
Figure 1.1: Potential concept for a robotic servicing vehicle (Courtesy of SSCO).

In pursuit of this mission, University of Maryland's Space Systems Laboratory has partnered with NASA's Satellite Servicing Capabilities Office to demonstrate technology that would be necessary for a nominal end-to-end robotic refueling or repair mission. Since there is limited heritage regarding the interaction between multiple spacecraft on-orbit, it is important to study how various satellite systems would react to the initial contact and ensuing robotic interaction of a servicing vehicle.

To develop this technology, a series of industrial robots can be utilized to simulate the relative motion between a servicing spacecraft and client satellite. By using a robotic simulator to mimic the dynamics of a given satellite (Fig. 1.2), it is possible to conduct end-to-end tests of various mission objectives such as rendezvous and proximity operations or grapple sequences between two representative bodies on the ground.
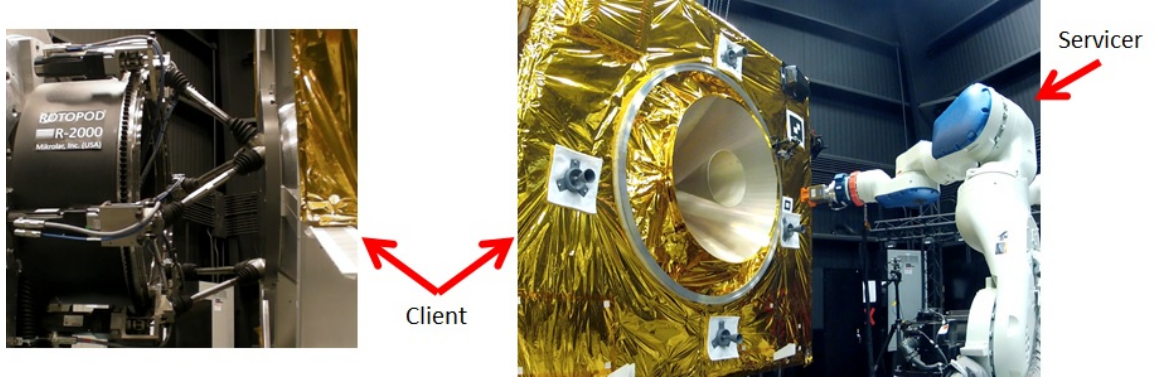
Figure 1.2: Robotic demonstration units mimicing the interaction between a robotic servicing vehicle and client satellite.

Currently, only the rigid-body dynamics of the servicing spacecraft and client satellite are implemented on these robotic demonstration units. The current simulator therefore neglects the effect of appendages such as solar panels or booms. How do the flexible-body dynamics affect the dynamics of the spacecraft system, though, and more importantly, how does it affect a potential servicing mission? To answer these questions, it is necessary to improve the fidelity of the current rigid-body model that simulates how the spacecraft system will react to forces imparted on the spacecraft.

1.2 Research Objectives

The proposed research in this thesis aims to investigate the interaction of a robotic servicing vehicle with a "non-cooperative" satellite that was not meant to be serviced. More specifically, this research effort includes modeling the dominant response of a given flexible-body satellite to an input profile similar to what it might

experience during a nominal satellite servicing mission. To accomplish this task, it is necessary to validate the highly coupled, rigid- and flexible-body dynamics by studying the system response to various types of input. Furthermore, by conducting a real-time hardware-in-the-loop simulation, it will be possible to observe the response of a given flexible-body satellite and characterize the potential impact of structural flexibility on an end-to-end satellite servicing mission.

1.3   Concept Overview

A prime directive in satellite servicing will be to prevent any potential damage to the client satellite due to the interaction forces exerted by a servicing vehicle. Figure 1.3 shows the interpretation of these interaction forces, modeled as a combination of force and torque inputs that act either directly on the satellite hub or appendages. These input types classify a majority of expected input profiles that could be caused by a servicing spacecraft during a repair or refueling mission, such as during the initial grappling of a client satellite. Various servicing maneuvers might also pose a threat due to the interaction forces between these two spacecraft.

In the pursuit of this complex problem, it will be necessary to develop a model of a rigid-body satellite hub with flexible appendages. By observing the first system modes, it will be possible to capture the dominant contributors to the overall system motion in the given spacecraft system scenario. Additional modes and a damping term are also introduced to increase the fidelity of the spacecraft model.

Multiple test cases will be developed to encompass the expected input profiles
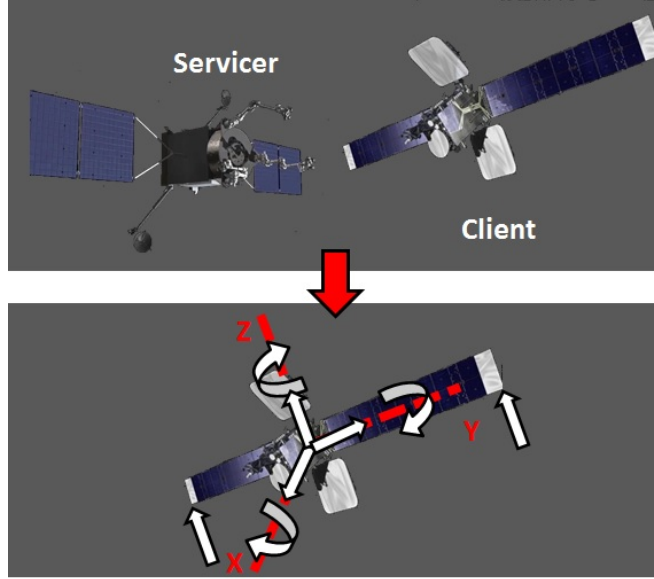
Figure 1.3: Representation of spacecraft interaction as input forces experienced by client satellite (Courtesy of SSCO and Intelsat).

during a nominal servicing mission, and the developed flexible-body model will predict the response of the client satellite over time. These results will then be validated against both software and hardware platforms to assess the ability to model a physical system on-orbit. As part of this validation effort, the derived rigid- and flexible-body dynamics will be implemented on a real-time system to conduct simulations of the physical interaction between two spacecraft and visualize the system response.

1.4 Thesis Structure

Chapter 2 begins with a discussion on background information and previous work done in the field. Chapter 3 introduces a method of defining flexible motion,

and explains the derivation of a coupled rigid- and flexible-body dynamics model. Chapter 4 introduces an independent software platform that is used to validate the dynamics model for basic test cases, and Chapter 5 integrates the derived dynamic model into a hardware-in-the-loop simulation which proves the ability to correlate the response of a physical system. Finally, Chapter 6 presents conclusions based on the software and hardware validation efforts and investigates the possibility for future work to expand on this research.

Chapter 2: Background and Previous Work

Although extensive research has been done to understand the orientation of a given spacecraft for the purposes of attitude control, little research has been conducted related to deriving the coupled rigid- and flexible-body dynamics that describe the interaction between multiple satellites. This is because only a few spacecraft have been designed to come in contact with another vehicle on-orbit, such as the berthing of various spacecraft to the International Space Station, the coupled motion of the Dextre robotic arm, and the Shuttle Remote Manipulator System (Figure 2.1). In order to develop a model of such a complicated interaction between spacecraft, it is necessary to investigate both force-based and energy-based methods that have been used to derive similar systems, and determine a suitable way to simulate a nominal satellite servicing mission.

2.1   Coupled Dynamics Model

The study of flexible-body dynamics on-orbit has been pursued for decades, including NASA's Control of Flexible Structures (COFS) flight experiment program [1] and the Magnetospheric Multiscale Mission (MMS), which incorporates a set of flexible booms on multiple spinning spacecraft to measure the Earth's mag-

Figure 2.1: Shuttle docked with the International Space Station (Courtesy of *www.abc.net.au*).

netosphere. The primary concern in both of these examples (shown in Fig. 2.2), however, is only how to control the spacecraft attitude. In proximity operations, even minor disturbances in displacement can mean the difference between a successful docking/capture or an impact and potential loss of contact. Studies such as Ploen's rigid-body description of a formation flying system [2] and Tobbe's dynamic analysis of a variable mass, flexible structure [3] have been working towards a method of describing and controlling more complicated systems, but neither of these focus on the coupled rigid- and flexible-body dynamics.

In order to derive the dynamics associated with a satellite servicing mission, it is necessary to compare the combined rigid- and flexible-body dynamics from multiple different applications [4]. A few contributors include Meirovitch's assessment of NASA's SCOLE and COFS missions, where flexible-body equations are applied to a laboratory environment and actual structures on-orbit [5], as well as the study of
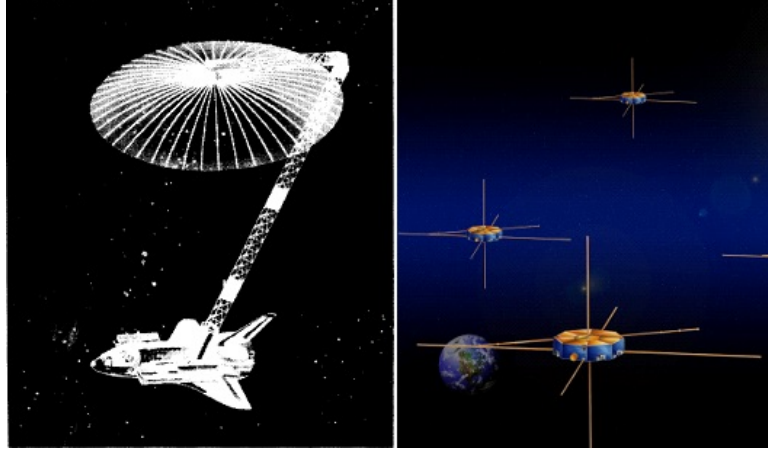
Figure 2.2: COFS II concept [1] and artist rendition of MMS (Courtesy of NASA).

high speed spacecraft maneuvers [6]. While the dynamics associated with a satellite servicing mission include a first approximation of a grapple sequence, the initial study proposed in this research does not feature high speed motion or an orbital dynamics representation of the surrounding environment. Thus, a more general solution is desired.

The dynamics developed in this research are based on Shabana's flexible-body dynamics [7], which starts by describing the kinetic and potential energy of the flexible satellite body. The system's equations of motion are then derived by applying the principle of virtual work, and can be expressed in either inertial or body coordinates [8]. A similar procedure has been shown to work well in predicting spacecraft motion, as applied to the reorientation of a flexible spacecraft [9], the control of a two-link robot manipulator [10] and the dynamics of an antenna pointing control system [11].

Commercial software packages such as Modelica^{TM} are built upon these coupled dynamics, but are not implementable on a real-time testbed. In the pursuit of

9

this goal, the proposed research develops a reduced-order model of the coupled dynamics to conduct hardware-in-the-loop simulations. The result of these simulations will be used to assess the impact of flexible-body excitation on a robotic servicing mission.

2.2   Beam Model

In order to derive the equations of motion for the spacecraft system, it is necessary to develop a model of the flexible-body appendages such as solar panels, antennae and/or booms that are attached to the client satellite. For appendages with complicated geometries, finite element methods (FEM) are typically used. However, for simpler shapes, more intuitive analytical methods such as the assumed modes method can be utilized to represent the relevant modal deformation effects [8]. Since the eventual goal is to implement a real-time simulation using simple appendage geometries, a full finite element model was not needed for this first validation effort. Instead, the assumed shape of an Euler-Bernoulli beam is used to represent each satellite appendage, and cantilever boundary conditions are assumed to exist between the satellite appendage and rigid-body hub. For simplicity, only the first few modes are used to capture the dominant response of the system. Furthermore, each appendage is assumed to only have a single flexible degree-of-freedom, meaning that each appendage will only deform along a single axis. This holds true for certain classes of appendages, and thus provides a valid simplification for this initial study of the potential impact of exciting the flexible-body motion on the overall mission.

2.3 Summary and Research Direction

So little information was known about the coupled dynamics of complex, rigid- and flexible-body systems prior to the 1980s that it was necessary to conduct multiple experiments on the Space Shuttle just to understand how such a complex system would behave in space. Similar to how Meirovitch and Quinn [5] had to combine both analytical and FEM approaches to derive an interpretation for the equations of motion, this research effort requires the use of both of these approaches. First, a flexible-body model is developed, utilizing the Rayleigh-Ritz method [12] to assume a mode shape that describes the deformation of each appendage over time. Finite element methods, although a valid alternative, are instead used as an independent verification tool of the overall system response, described in Chapter 4.

Chapter 3:   Modeling Rigid- and Flexible-Body Dynamics

In order to develop the coupled equations of motion that describe a particular satellite system, it will be necessary to separately derive the rigid- and flexible-body components. These components are a function of the geometry and structural properties of the spacecraft hub and flexible appendages, and can be combined to describe the response of a realistic satellite such as the GOES-class spacecraft shown in Figure 3.1.
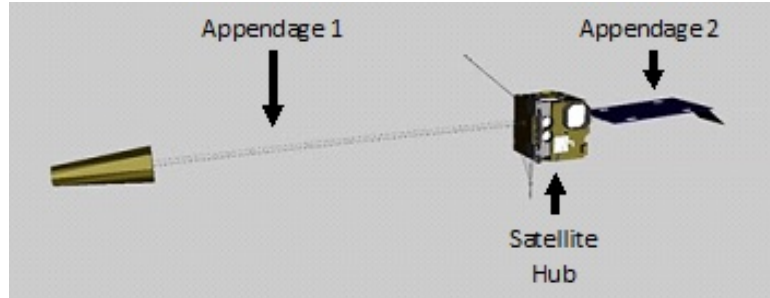
Figure 3.1: Visualization of GOES-class satellite.

This system includes a central satellite hub and multiple appendages including a solar panel, boom and two antennae. For the purpose of this research, only the dominant effects of these appendages are studied, so the effect of the antennae is assumed to be negligible due to its small mass compared to the boom and solar panel. The generalized equations of motion of this rigid-body and two-appendage

system is thus given by (3.1). The total mass matrix of the particular system is given by $[M_{system}]$, which contains components of the rigid-body satellite hub (M_{hub}), first flexible appendage (M_{flex_1}) and second flexible appendage (M_{flex_2}). Similarly, $[Q_{system}]$ is a summation of the quadratic velocity terms including the effect of the satellite hub (Q_{hub}) and two appendages (Q_{flex_1}, Q_{flex_2}). These include the Coriolis and centrifugal forces associated with the translational and rotational degrees-of-freedom as well as the active forces associated with modal coordinates.

$$[M_{system}] [\ddot{\bar{x}}] = [Q_{system}] + [\bar{u}_{input}] \tag{3.1}$$

$$M_{system} = M_{hub} + M_{flex_1} + M_{flex_2} \tag{3.2}$$

$$Q_{system} = Q_{hub} + Q_{flex_1} + Q_{flex_2} \tag{3.3}$$

The initial contact of a servicing satellite is modeled as a combination of input forces $(\bar{F}_{ext}, \bar{Q}_{ext})$ and torques $(\bar{T}_{ext})$ on the client vehicle, summarized as:

$$[\bar{u}_{input}] = \begin{bmatrix} \bar{F}_{ext} \\ \bar{T}_{ext} \\ \bar{Q}_{ext} \end{bmatrix} \tag{3.4}$$

The ensuing system response includes translational, rotational and modal components, as shown as the second derivative of the satellite's state:

$$[\ddot{\bar{x}}] = \begin{bmatrix} \ddot{\bar{R}} \\ \bar{\alpha} \\ \ddot{q}_f \end{bmatrix} \quad\quad (3.5)$$

Note that for the duration of this derivation, a bar on top of a particular variable designates that the given value is described in body frame. Thus, the linear acceleration of the satellite in the body frame is given by $\ddot{\bar{R}}$ and the angular acceleration by $\bar{\alpha}$. Since the modal coordinate is frame-independent, no distinction between body and inertial frame representation is necessary, so the modal acceleration term can simply be represented by $\ddot{q}_f$. The dimensions of the state, $[\bar{x}]$, and input vector, $[\bar{u}_{input}]$, will be of size $(6 + mn)$, where n modes are observed for each of a satellite's m appendages.

The equations of motion can then be manipulated [13] to propagate the state over time as follows:

$$[\ddot{\bar{x}}] = [M_{system}]^{-1} \left([\bar{u}_{input}] + [Q_{system}] \right) \quad\quad (3.6)$$

This calculation is carried out by a fourth-order Runge-Kutta method which outputs the state over time. From the propagated state, it is possible to extract the resulting flexible-body motion by observing the satellite hub pose and rates as well as the deformed tip position and rates of each appendage.

The derivation of the combined rigid- and flexible-body dynamics are hereby defined, as applied to a multi-spacecraft mission where both relative translation and orientation are critical to mission success. The goal is to find the overall equations

of motion that describe how the external forces from a servicing spacecraft influence the flexible-body motion of a client satellite.

3.1   Rigid-Body Description

A description of the rigid- and flexible-body satellite dynamics is captured by the mass matrix and quadratic velocity vector which describe the system. The dynamics of the rigid-body satellite hub itself can be described by these two components, which only incorporate translational and rotational motion. For this analysis, m_s is the mass of the satellite hub, I_{3x3} is a three-by-three identity matrix, $\bar{r}_{cm_s}$ is the position of the center of mass of the satellite hub relative to the body frame origin, and I_{o_s} is the satellite hub area moment of inertia, about the center of mass of the entire satellite. Furthermore, w_s is described as the satellite hub angular velocity vector, where the "$\sim$" denotes the cross product matrix form of the vector.

$$M_{hub} = \begin{bmatrix} m_s I_{3x3} & -m_s \tilde{\tilde{r}}_{cm_s} \\ m_s \tilde{\tilde{r}}_{cm_s} & I_{o_s} \end{bmatrix} \tag{3.7}$$

$$Q_{hub} = \begin{bmatrix} m_s \tilde{w}_s \left(\tilde{w}_s \bar{r}_{cm_s} \right) \\ \tilde{w}_s I_{o_s} w_s \end{bmatrix} \tag{3.8}$$

3.2   Deformable Body

The first step in deriving the flexible appendage dynamics that contribute to the overall system equations of motion is to understand how to describe the

location of a point on a flexible-body. It can be shown that by using a reference frame as shown in Figure 3.2, the position of a point on a deformable body, r, can be expressed in an inertial frame [8] as shown in (3.9). Here, R is a vector describing the location of the body coordinate system origin relative to the inertial frame, A is the rotation matrix from inertial frame to body frame, and $\bar{u}$ is the position of a point on the flexible-body, expressed in body frame. The position of a point on the flexible-body can be subdivided into the undeformed (rigid) position $(\bar{u}_o)$, relative to the body frame origin, and the deformed position of the flexible-body $(\bar{u}_f)$. In other words, the undeformed position is the location of the point of interest before the body deforms, whereas $\bar{u}_f$ is a measure of how much the point on the flexible-body deforms at a particular time. In the example of the satellite hub with two appendages attached, the flexible-body is one of the appendages, the undeformed position could describe the location of the appendage tip before any deformation occurs, and the deformed position would describe the amount that the tip deforms at any particular instant in time. Finally, the mode shape matrix that describes the deformation of each appendage is expressed as a (3 x n) matrix, S, and the modal state of the flexible-body is given by an (n x 1) vector, q_f.

$$r = R + A\bar{u} = R + A(\bar{u}_o + \bar{u}_f) = R + A\bar{u}_o + ASq_f \qquad (3.9)$$
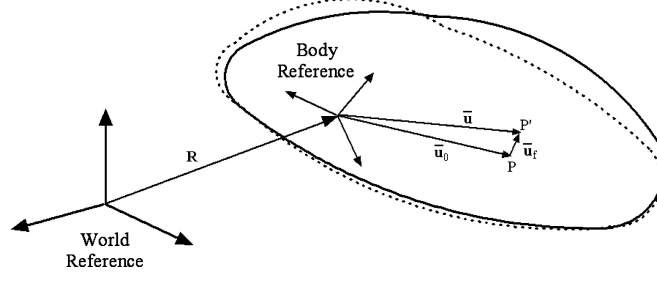
Figure 3.2: Flexible-body reference system (Courtesy of Schiavo) [8].

3.2.1 Flexible-Body Equations of Motion

From this description, it is possible to derive the flexible-body equations of motion for a single flexible appendage, using the principle of virtual work [7]. By transforming the mass matrix and quadratic velocity vector to body coordinates [8], the following components can be derived, where m_{RR}, $\tilde{\bar{S}}_t$, $\bar{S}$, $\bar{I}_{\theta\theta}$, $\bar{I}_{\theta f}$, m_{ff}, Q_v^R, Q_v^θ, and Q_v^f are modal integrals, which are defined in Appendix A.

$$
M_{flex} = \begin{bmatrix} m_{RR} & \tilde{\bar{S}}_t^T & \bar{S} \\ \tilde{\bar{S}}_t & \bar{I}_{\theta\theta} & \bar{I}_{\theta f} \\ \bar{S}^T & \bar{I}_{\theta f}^T & m_{ff} \end{bmatrix} \tag{3.10}
$$

$$
Q_{flex} = \begin{bmatrix} Q_v^R \\ Q_v^\theta \\ Q_v^f - k_{ff}q_f - b_{ff}\dot{q}_f \end{bmatrix} \tag{3.11}
$$

These two components can be combined using (3.1) to fully describe the response of a single flexible-body appendage to input forces and torques. A damping term, b_{ff}, has been added to Schiavo's description [8] to more accurately describe

17

a realistic system, and a matrix describing the stiffness of the flexible-body, k_{ff}, is given as a function of the appendage's length, L_a, and structural rigidity, EI, by the following equation [6, 14, 15].

$$k_{ff} = EI \int_0^{L_a} \left(\frac{d^2 S}{dx^2}\right)^T \left(\frac{d^2 S}{dx^2}\right) dx \tag{3.12}$$

where E is the modulus of elasticity and I is the cross-sectional inertia of the appendage.

3.2.2 Coupled Equations of Motion

In order to develop a model of an entire satellite, it is necessary to combine the rigid-body dynamics of the satellite hub with the combined rigid- and flexible-body dynamics that describe each appendage. Thus, a spacecraft system including a rigid-body hub and two flexible appendages can be modeled using the system mass matrix and quadratic velocity vector, shown in (3.13) and (3.17).

$$M_{system} = \begin{bmatrix} M_{RR} & M_{R\theta} & \bar{S}_1 & \bar{S}_2 \\ M_{R\theta}{}^T & M_{\theta\theta} & \bar{I}_{\theta f1} & \bar{I}_{\theta f2} \\ \bar{S}_1{}^T & \bar{I}_{\theta f1}{}^T & m_{ff1} & 0_{nxn} \\ \bar{S}_2{}^T & \bar{I}_{\theta f2}{}^T & 0_{nxn} & m_{ff2} \end{bmatrix} \tag{3.13}$$

$$M_{RR} = m_s I_{3x3} + m_{RR_1} + m_{RR_2} \tag{3.14}$$

$$M_{R\theta} = m_s \tilde{r}_{cm_s}^T + \tilde{\bar{S}}_{t_1}^T + \tilde{\bar{S}}_{t_2}^T \tag{3.15}$$

18

$$M_{\theta\theta} = I_{o_s} + \bar{I}_{\theta\theta_1} + \bar{I}_{\theta\theta_2} \tag{3.16}$$

$$Q_{system} = \begin{bmatrix} m_s \tilde{\omega}_s \left(\tilde{\omega}_s \bar{r}_{cm_s} \right) + Q_{v_1}^R + Q_{v_2}^R \\[2mm] \tilde{\omega}_s I_{o_s} \omega_s + Q_{v_1}^\theta + Q_{v_2}^\theta \\[2mm] Q_{v_1}^f - k_{ff_1} q_{f_1} - b_{ff_1} \dot{q}_{f_1} \\[2mm] Q_{v_2}^f - k_{ff_2} q_{f_2} - b_{ff_2} \dot{q}_{f_2} \end{bmatrix} \tag{3.17}$$

where the subscript "1" or "2" refers to the first or second appendage, attached to the satellite hub.

3.2.3   Specifying Number of Modes

It is important to note that in the general case, the independent effects of axial, torsional or lateral motion can each be described by a single mode shape description for each axis, ϕ_x, ϕ_y and ϕ_z. These effects can be combined together [7] to form the mode shape matrix, S, which includes multiple types of deformation and numbers of modes.

It is assumed during this research effort that the desired number of modes observed in one appendage matches that of the other appendage, which is not necessarily the case for more complicated sets of appendage types. In addition, it is assumed that the modal components of each appendage do not directly affect one another, as shown by the zero entries in the coupled mass matrix of the system presented in the previous section. In higher-fidelity models, this cross-coupling cannot be ignored.

The derived equations thus far apply to a satellite with rigid and flexible components, where an arbitrary number of modes of each appendage can be observed by altering the corresponding terms within the system mass matrix and quadratic velocity vector. For example, to model the first two modes of an appendage with a single flexible degree-of-freedom (i.e., only lateral motion observed), q_f is a vector of dimension 2, and m_{ff} becomes a 2x2 matrix, describing the pure modal component of the mass matrix. In this case, the mode shape matrix would be a 3x2 matrix given by (3.18), where ϕ_{z1} describes the first mode shape, ϕ_{z2} describes the second mode shape and $\phi_{x1} = \phi_{x2} = \phi_{y1} = \phi_{y2} = 0$ since it is assumed that the appendage only has a single flexible degree-of-freedom.

$$S = \begin{bmatrix} \phi_{x1} & \phi_{x2} \\ \phi_{y1} & \phi_{y2} \\ \phi_{z1} & \phi_{z2} \end{bmatrix} \tag{3.18}$$

3.2.4 Damping Model Derivation

For this research effort, the effective damping of a satellite appendage is modeled as a viscous damper, with viscosity b_{ff} and the natural frequency of mode i given by w_{n_i}:

$$b_{ff_i} = 2m_{eff_i}w_{n_i}\zeta \tag{3.19}$$

$$w_{n_i} = \sqrt{\frac{k_{ff_i}}{m_{eff_i}}} \qquad (3.20)$$

Note that the effective mass of the system, m_{eff} varies depending on the rigid-body coupling, but approaches the appendage mass as the satellite hub approaches an infinite mass. This is further explored in Appendix B, but can be explained by the transition of the appendages from a cantilever to a free-free boundary condition, as the satellite hub mass changes relative to the appendage mass.

To simulate the damped response of a given system, it is assumed that the damping ratio characteristic of the system, ζ, is known and input to the model. In some cases, this value can be extracted from experimental data of the physical system, but values between $0.25\% - 2.5\%$ [16] are observed in test cases presented throughout this research. This damping term simulates the minimal structural and molecular friction effects which contribute to damping in the environment experienced by spacecraft on-orbit.

3.3   Summary

A model of the coupled rigid- and flexible-body dynamics has been developed which can describe an arbitrary number of appendages and modes. An example of the mass matrix and quadratic velocity vector components of a satellite with two appendages is shown, along with the addition of stiffness and damping terms to form the overall equations of motion that describe the system.

Once the equations of motion describing a particular system are developed,

a method of propagating the state over time must be utilized. In this way, it is possible to simulate the response of a spacecraft to a set of input forces and torques acting on the spacecraft hub and appendages.

Chapter 4: Flexible-Body Modeling and Simulation

Now that the coupled rigid- and flexible-body dynamics have been developed to describe the interaction between a robotic servicing vehicle and client satellite, it is essential to validate whether or not the predicted system response is accurate. The first validation effort includes comparing the results of a continuous beam model, derived from the presented rigid- and flexible-body dynamics, against independently developed models.

To accomplish this task, finite element models of the spacecraft system have been developed utilizing both NASTRAN^{TM} and ADAMS^{TM} software platforms. Although finite element analysis is an alternate approach to the assumed modes method, the simulations in ADAMS^{TM} are not conducted in real-time, and thus can only be used as a verification tool. By comparing the simulation output of these models with that of the model developed in the previous chapter for the same input, it will be possible to validate the derived equations of motion.

A description of the continuous beam and finite element models are hereby given, followed by a set of test parameters derived from realistic satellite properties. Multiple test cases are introduced and the predicted response from both models are compared with and without damping, for a variety of input profiles.

4.1 Continuous Beam Model

In order to conduct initial testing of the derived equations of motion, a MATLAB software algorithm was developed, incorporating the dynamics of a satellite hub with flexible appendages. An input profile including time-varying forces and torques is used to simulate the interaction a client satellite might have with a servicing spacecraft. The resulting flexible-body motion includes the satellite pose and rates as well as the modal deflection of the satellite appendages. This simulation allows for the number and location of the appendage(s) to be changed, along with the direction of the single flexible degree-of-freedom.

Each appendage is modeled as a cantilever beam fixed to the satellite hub, and the modal displacement is described by an assumed mode shape, ϕ. Figures 4.1 and 4.2 show the first two assumed modes for a single appendage with a length of 5 meters, which can be described by the sinusoidal function, representing an Euler-Bernoulli beam with fixed-free boundary conditions [17]:

$$\phi_i = \cosh\left(\frac{\lambda_i x_a}{L_a}\right) - \cos\left(\frac{\lambda_i x_a}{L_a}\right) - k_{c_i}\left(\sinh\left(\frac{\lambda_i x_a}{L_a}\right) - \sin\left(\frac{\lambda_i x_a}{L_a}\right)\right) \qquad (4.1)$$

$$k_{c_i} = \frac{\sinh(\lambda_i) - \sin(\lambda_i)}{\cosh(\lambda_i) + \cos(\lambda_i)} \qquad (4.2)$$

where both variables λ_i and k_{c_i} are constants (provided in Table B.1) which are dependent on the mode shape and boundary conditions, where a point on the flexible-body is located a distance, x_a, along an appendage of length L_a.
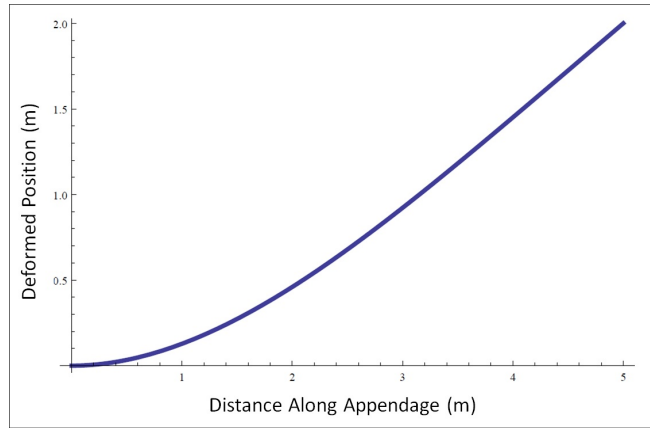
Figure 4.1: First mode shape of appendage modeled as an Euler-Bernoulli beam.
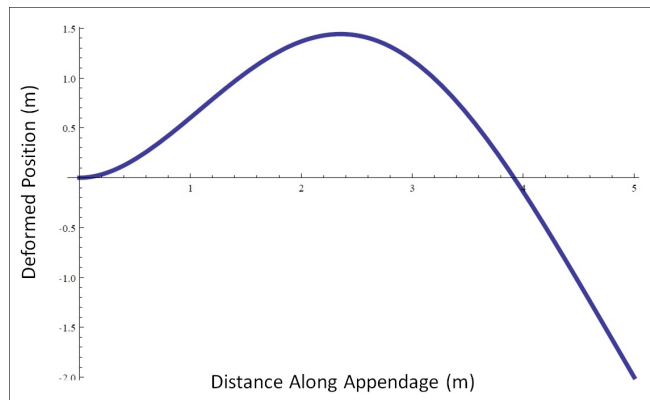
Figure 4.2: Second mode shape of appendage modeled as an Euler-Bernoulli beam.

It is important to note that modeling the appendages as Euler-Bernoulli beams assumes that each flexible body can be accurately represented as a slender beam, and that only low frequency responses are encompassed in the simulation. In addition, this assumption only holds valid for small shear deformations, a constant cross section, uniform beam, and only includes transverse inertia and stiffness terms. This model thus does not contain tension, axial forces or rotary inertia effects and only low frequency system responses can be observed.

An additional simplifying assumption includes the fact that the appendages only deform in a single direction. In other words, the modal displacement of each appendage is assumed to only deform about a single axis, to simulate the single-degree-of-freedom flexible-body model proposed in this research. Furthermore, only the first two modes of either beam are observed in this research, which enables the analysis of four non-rigid system modes (this is further explained in Appendix B). For the system described in this research, modeling the first four flexible-body modes captures the dominant response of the flexible-body. In the most general case, an analysis would have to be conducted to determine how many modes must be modeled to capture the dominant response of a given system.

4.2   Finite Element Model

In order to validate the combined rigid- and flexible-body dynamics, an additional model was constructed in ADAMS^{TM} to check that the resulting motion accurately represents a given system. This independent simulation platform features

a finite element model imported from NASTRAN^{TM} that consists of a concentrated mass located at the center of a free-free beam (Fig. 4.3), where a theoretical satellite hub is shown to better visualize how the finite element model represents the same system as the continuous beam model.

A quick study was conducted (Tables B.3 and B.4) to determine that eighty elements per appendage were sufficient to accurately capture the flexible-body motion. Although the finite element model contains multiple degrees-of-freedom for each appendage, the higher-order modes were not included in the response in order to more accurately represent the simplified continuous beam model. Since the continuous beam model response includes two modes of interest per appendage, the first four non-rigid system modes were enabled in ADAMS^{TM}. Thus, by matching the frequency response, structural parameters, and system mass and inertia values, it is possible to utilize this ADAMS^{TM} model as an alternate representation of the given satellite system.
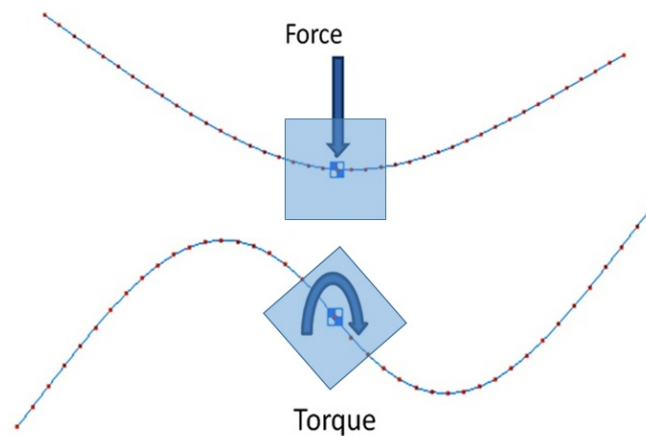
Figure 4.3: Finite element representation of a satellite with two appendages.

The correlation between the continuous beam and ADAMS^{TM} finite element models will act as a comprehensive check of the flexible-body implementation onto a real-time system. This validation will considerably build confidence in the ability to accurately simulate the response of a client satellite to various input profiles that would be evident during the interaction with a robotic servicer.

4.3   Design of Satellite Test Parameters

To correlate the predicted flexible-body response according to the continuous beam and finite element models, it is necessary to design a nominal set of satellite parameters to use as inputs to both models. Structural parameters similar to the TDRSS or GOES spacecraft were initially investigated, however it was determined that simpler spacecraft models would allow for a more intuitive system response for the first iteration of the flexible-body simulation. Although the satellite hub geometry for either spacecraft can be approximated as a cube shape, the appendages are simplified to resemble slender rods of uniform density and modulus.

Simple ratios between the mass and length of a specific appendage versus the main satellite hub were estimated for similar classes of spacecraft, and numerous values of flexural rigidity were compared [1,3,9,18]. It was decided that the first mode of the simplified satellite's appendage should be 0.25 Hz to mimic actual appendage data [16]. Assuming that each appendage is modeled as a uniform cylindrical beam with a cross-sectional area designed to match this frequency (found using (B.2)), the corresponding structural rigidity can be calculated follows:

$$EI = \left(\frac{2\pi f_{i_{<Hz>}}}{\lambda_i{}^2} \right)^2 \left(\mu_a L_a{}^4 \right) \tag{4.3}$$

where E is Young's modulus, I is the cross-sectional inertia, $f_{i_{<Hz>}}$ is the frequency of mode i, and μ_a is the mass of an appendage divided by its length [17].

The result of this calculation is given in Table 4.1, along with the rest of the satellite parameters used in this simulation. Note that the appendage inertia value includes the principal axes of mass moment of inertia about the center of mass of the appendage. The simulation itself converts this value to the effective inertia of the appendage about the center of mass of the overall satellite system. For the given satellite orientation, the center of mass of the hub is coincident with the center of mass of the satellite system.

Table 4.1: Spacecraft hub and appendage parameters.

	m (kg)	L (m)	$I_{o_{prin}}$ (kg-m^2)	EI (N-m^2)
Hub	500	1	83, 83, 83	-
Appendage	100	5	208, 0.006, 208	2495

4.4   Test Case Definition

During the initial testing in MATLAB, numerous input variables were changed within the model including the forces and torques experienced by the spacecraft as well as its initial conditions. This research focuses on testing satellites with two appendages in order to provide a symmetric response that is more readily agreeable with intuition. A coordinate system was developed to describe a particular test

case and corresponding satellite configuration, which includes the location of each appendage relative to the satellite hub and the flexible degree-of-freedom. As an example, Figure 4.4 shows a two-appendage case where both appendages are located along the y-axis and are allowed to deform in the z-direction.
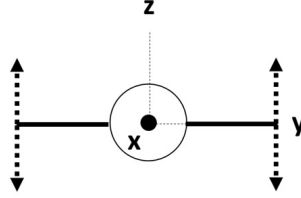
Figure 4.4: Flexible-body coordinate system showing single-DOF flexible motion.

Three types of test cases were developed based on whether the system excitation was due to an external force, torque, or modal input. An arbitrary input profile can be described by a linear combination of these three types of exogenous input, which means that the validation of these three cases is sufficient to prove the accuracy of the predicted flexible-body motion.

The first of these test cases includes exciting the system with an impulsive force in the z-direction. The expected initial response is shown in Figure 4.5, which shows how the appendages oscillate symmetric to one another, as the satellite hub translates in the positive z-direction over time.

In order to excite the second system mode, an input torque is exerted about the x-axis (Fig. 4.6). Although no translation is present in the ensuing motion, the flexible appendages cause a different type of oscillatory response, this time in the overall orientation of the vehicle. Although the two appendages will continuously oscillate asymmetrically, an impulsive input results in an average non-zero angular

velocity about the x-axis.
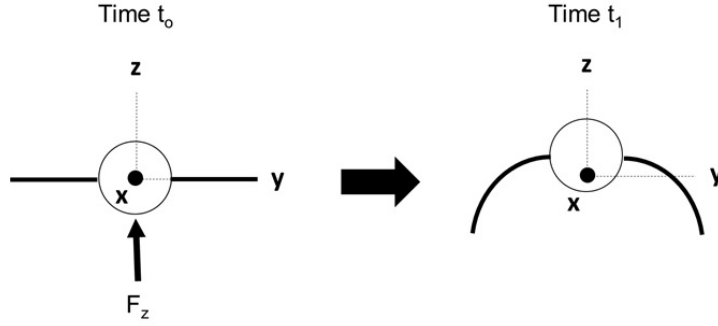
Figure 4.5: Symmetric response to an input force in the z-direction.
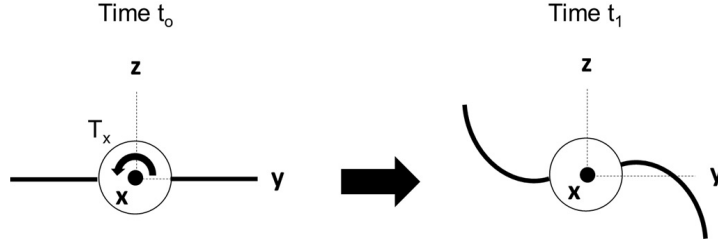
Figure 4.6: Asymmetric response to an input torque about the x-axis.

The third and final test case involves giving the appendages initial modal conditions. One example of such conditions can excite the first system mode, where the two appendages start displaced in the same direction by the same amount as is shown in the first picture in Figure 4.7. Likewise, displacing the appendages in opposite directions before beginning the simulation can excite the second mode of the system. Furthermore, an initial modal velocity can excite the first flexible system modes and will result in a steady-state translational or rotational velocity that mimics the force or torque input cases, corresponding to whether the initial modal velocity of the two appendages are in equal or opposite directions.

31

Figure 4.7: Response to an initial modal position, exciting the first or second mode.

Note that for the duration of this Chapter, the first and third flexible-body system modes will be referred to as the "symmetric" modes since they result from the appendages oscillating symmetrically from one another. Similarly, the second and fourth flexible-body system modes will be referred to as the "asymmetric" modes.

4.5   Simulations

Now that a set of test cases has been defined, it is of interest to directly compare the response of a given system, as predicted by the continuous beam and finite element models. First, the pure modal response is correlated for a satellite hub with infinite mass in order to simulate a classic, cantilever beam case. Then, the undamped response of a finite mass satellite hub is observed, for both the force and torque input test cases. Following this correlation, a damping term is introduced, followed by a combined force and torque input case to summarize the entire validation effort. For all test cases produced, the described input profile acts impulsively, for the first second of the simulation.

4.5.1 Infinite Mass Satellite

The first correlation effort between the continuous beam and ADAMS^{TM} finite element models includes the comparison of the first two mode shapes, when the mass of the satellite is set to 10^6 kg, a near-infinite hub mass compared to the appendage mass (100 kg). This simulation will test the purely modal response of each appendage, which behaves like a cantilever beam. In this context, the rigid-body dynamics are isolated from the modal response because of the near-infinite satellite hub mass.

The response of the flexible-body dynamics to a one second force step input is shown in Figure 4.8, where only the symmetric modes are excited. The first plot in this figure is showing the rigid-body hub velocity over time as affected by the external force and resulting appendage motion, whereas the second plot portrays the deformed position of the first appendage tip relative to the hub as a function of time. Since the second appendage response is exactly the same as the first appendage for symmetric system modes, it is only necessary to include the response of a single appendage for this test case.

As expected, the near-infinite mass hub produces a nearly static rigid-body response even though the appendages are each excited at 0.25 Hz. A near-perfect correlation is evident in Figure 4.8, as the ADAMS^{TM} finite element model predicts the same response as the continuous beam model derived in Chapter 3.

It is also of interest to observe the pure modal response of the system due to a torque impulse, which excites the asymmetric system modes. This response, shown
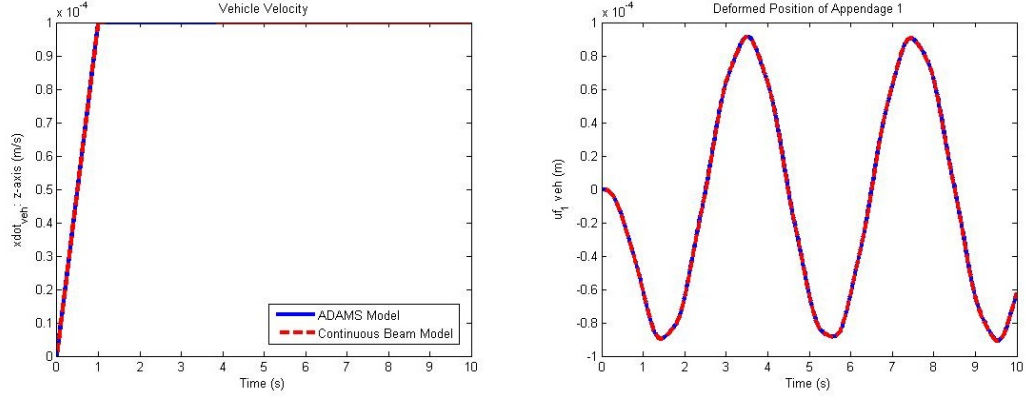
Figure 4.8: Response of infinite mass satellite to force excitation.

in Figure 4.9, again shows small rigid-body motion due to the large mass and inertia of the satellite hub. In this case, the angular velocity is plotted versus time since the excited asymmetric modes cause an overall orientation shift for the satellite. The response of the first appendage is given in the second plot in Figure 4.9, and the second appendage is known to exhibit the exact opposite response over time, such that its response is always the negative of the first appendage. Again, the response as predicted by the ADAMS^{TM} finite element model correlates with the response according to the continuous beam model.
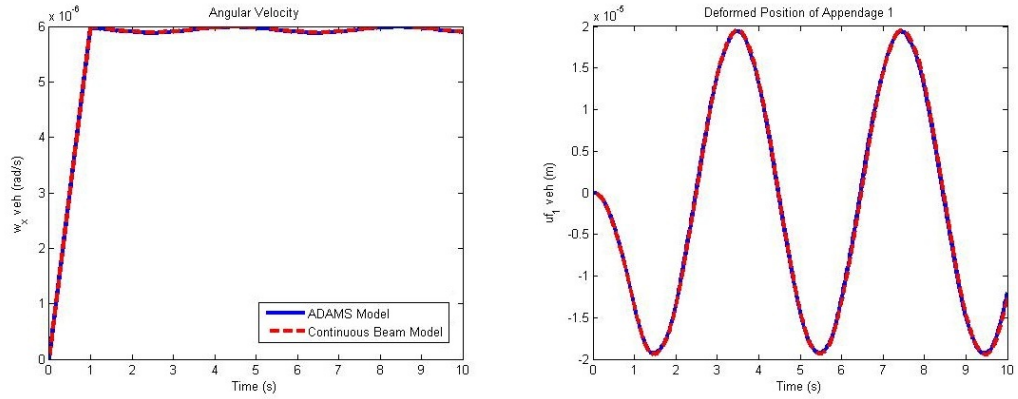
Figure 4.9: Response of infinite mass satellite to torque excitation.

34

4.5.2 Undamped Force Input

The first test case incorporates the satellite parameters given in Table 4.1 and highlights the response of only the first system mode, where the appendages oscillate symmetric to one another. This first mode is excited by a step input force of 100 N that is exerted for one second, directly on the satellite hub in the positive z-direction as referenced by the coordinate system shown in Figure 4.4. As expected, this force impulse results in an overall oscillatory motion with a non-zero steady-state velocity of the satellite as shown in Figure 4.10. The ability to simulate this simplified motion is shown by the nearly perfectly aligned responses predicted by the continuous beam and ADAMS^{TM} finite element models. Both the satellite hub velocity and deformed position of an appendage are compared, which shows the validation of both the modal response of the appendage(s) and the coupled rigid- and flexible-body response of the satellite hub.
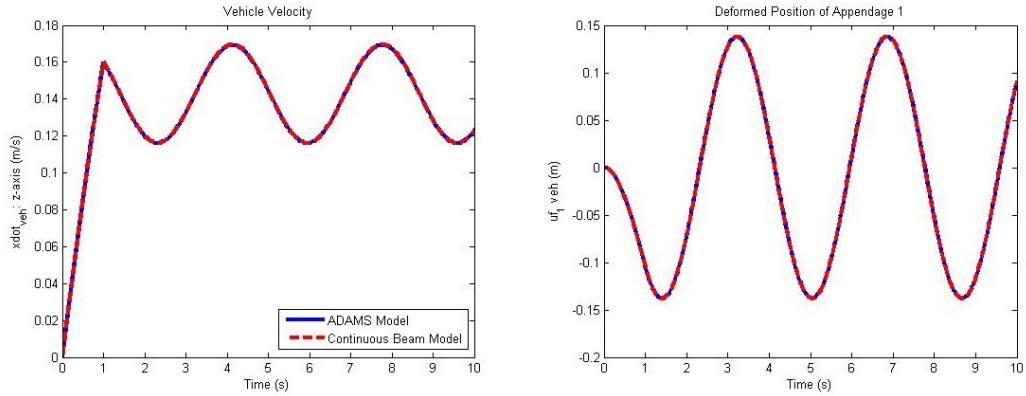
Figure 4.10: Force input test case response for single cantilever mode per appendage.

Once the single system mode response is correlated, the model is expanded

to include the first two symmetric system modes, excited by the same force profile. Figure 4.11 shows the response of this higher-fidelity model, where the second symmetric mode contributes in a minor but non-negligible way to portray a more realistic motion profile.
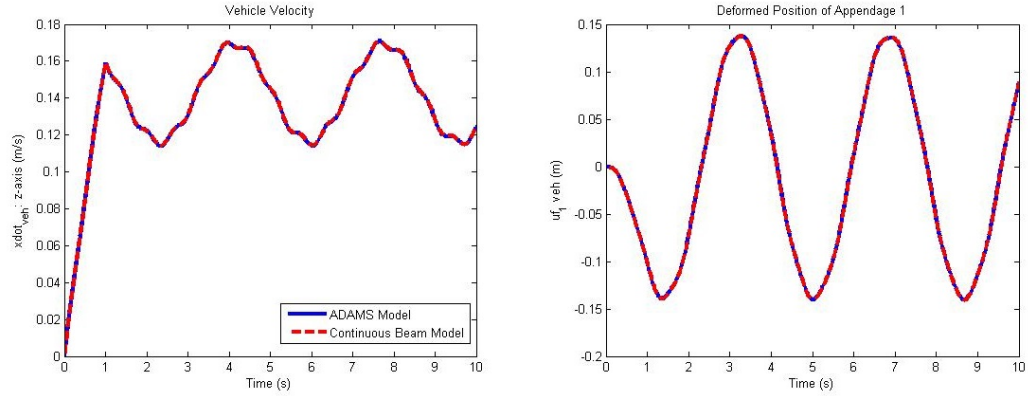
Figure 4.11: Force input test case response including two cantilever modes per appendage.

To prove that the predicted response contains the expected two modes, a power spectral density analysis was conducted, as seen in Figure 4.12. From this analysis, it is clear that the input excites two separate frequencies, in this case a 0.25 Hz signal and a 1.57 Hz signal. These, along with the asymmetric mode frequencies, are tabulated in Figure B.1, which compares the predicted mode shape frequencies for appendages with either cantilever or free-free boundary conditions. This analysis has thus proven that the resulting motion of the satellite system indeed exhibits the two oscillation frequencies that were expected, acting as an additional check of the implemented flexible-body dynamics for the satellite and two-appendage system.

Although it is possible to include additional modes to the flexible-body model,
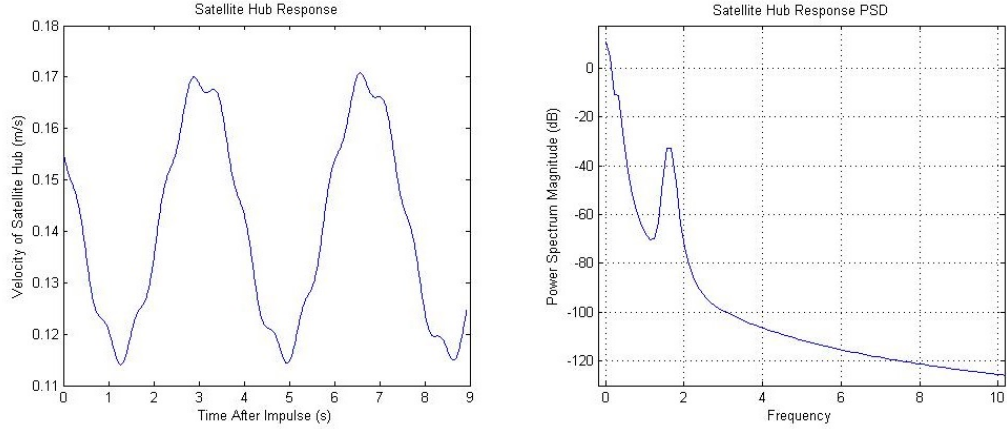
Figure 4.12: Power spectral density analysis showing modal frequencies of system response to a force input.

it is clear that the added effect of the second mode is approximately an order of magnitude less than that of the first mode. From this observation, it is possible to conclude that the dominant system response can be captured by only the first couple of modes, as the contribution of higher modes would continue to drop off for the current system. Note that for more complicated appendage geometries, this might not be the case. For example, NASA Langley's Large Hoop Antenna has over 70 significant modes which contribute to the performance of the system [19].

4.5.3 Undamped Torque Input

The second test case features exciting the asymmetric system modes, by applying an impulsive torque input of 1 N-m to the satellite hub. For this correlation effort, the angular velocity of the satellite and deformed position of an appendage are directly measured and compared, encompassing both the rotational and modal components excited by this input. Similar to the last test case, the torque input

is experienced for one second which causes a "pinwheel" effect, where the satellite rotates back and forth, oscillating in the clockwise and counter-clockwise directions with a non-zero steady-state rotation depending on the direction of the initial input profile. The corresponding oscillation is evident in both plots shown in Figure 4.13, where the response is heavily dominated by the beam's first asymmetric system mode.
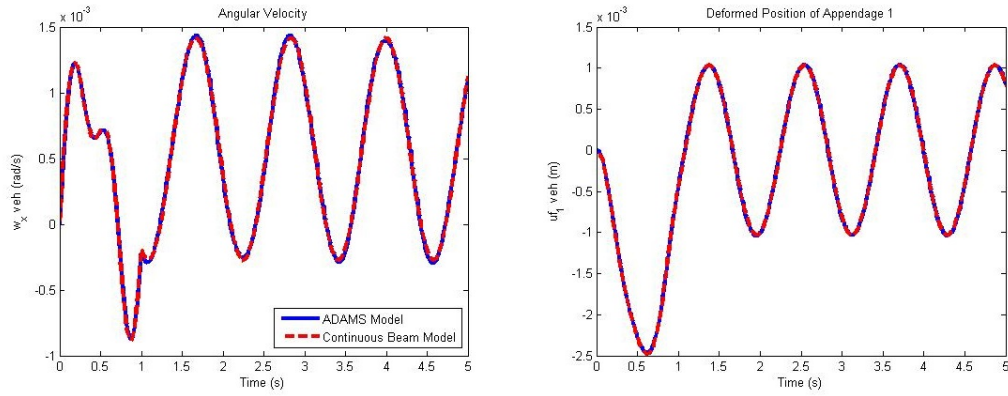
Figure 4.13: Torque input test case response including two cantilever modes per appendage.

4.5.4   Damped Response

After the undamped system responses have been correlated for both the force and torque input cases, a damping term is added to better model how a physical system would react to an exogenous input. For the purpose of this research, a viscous damping term is derived and added to the system equations of motion, where the damping ratio corresponding to a given satellite appendage is input to the model.

As a first attempt, (4.4) and (4.5) were used to add a viscous damping term

38

to the derived flexible-body model:

$$b_{ff} = 2m_{ff}w_n\zeta \tag{4.4}$$

$$w_n = \sqrt{\frac{k_{ff}}{m_{ff}}} \tag{4.5}$$

Although only a slight discrepancy is observed in the modal response of the system due to a force input (seen in Fig. 4.14), the asymmetric system response due to a torque input (Fig. 4.15) clearly shows that this implementation is not accurate, as neither the angular velocity nor deformed tip positions match with the finite element model predictions.
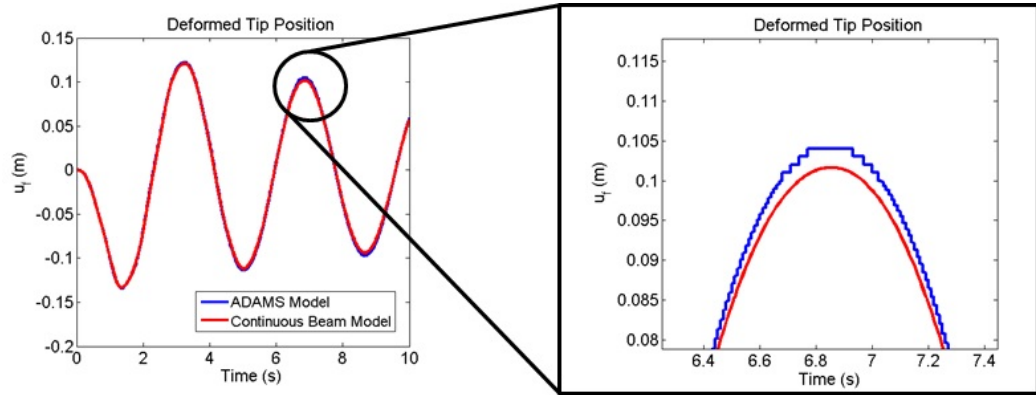
Figure 4.14: Iteration 1: Damped force input test case response for $\zeta = 0.025$.

The discrepancy shown in this first attempt is due to the fact that the non-infinite satellite hub mass affects the system response frequency. This is further explained in Figure B.2, however the key is that the appendage mass term must be replaced by the effective mass of a given satellite system as indicated previously in (3.19) and (3.20). The effective mass is only equal to the appendage mass in the case of an infinite satellite hub mass.
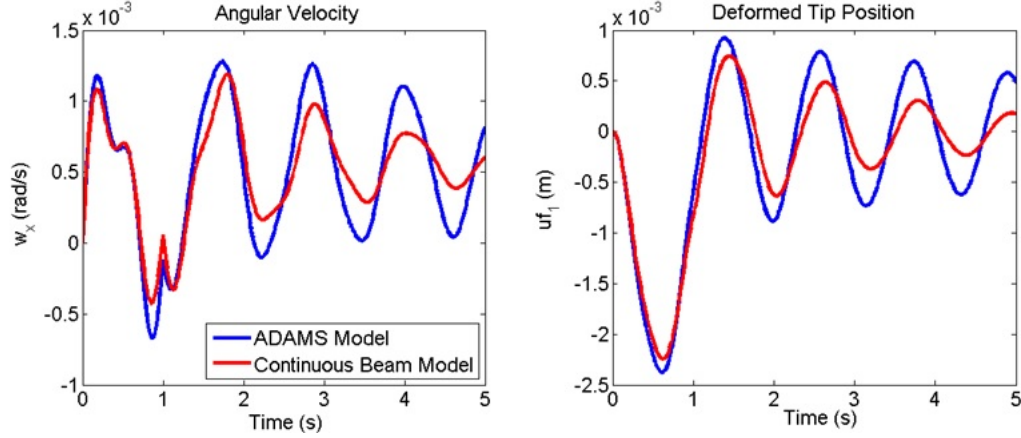
Figure 4.15: Iteration 1: Damped torque input test case response for $\zeta = 0.025$.

As explained in the planar analysis included in Appendix B, it is less straightforward to determine the effective mass for the torque input case. For this reason, an approximation was used to alter the damped response. Solving (4.5) for m_{ff} and substituting into (4.4) gives:

$$b_{ff} = 2k_{ff}\frac{\zeta}{w_n} \qquad (4.6)$$

This indicates that the damping term, b_{ff}, is inversely proportional to the natural frequency of the system, w_n. Thus, by compensating for the change in frequencies between the infinite versus finite mass satellite hub, it is possible to approximate the effect of the finite satellite hub mass on the frequency of the overall flexible-body satellite. As an example, the GOES-class satellite with an infinite mass satellite hub exhibits a 0.25 Hz frequency for the first asymmetric mode, whereas the system featuring a finite (500 kg) mass hub exhibits a 0.86 Hz frequency. By multiplying the damping term given in (4.4) by the inverse ratio of the frequencies, $\left(\frac{0.25}{0.86}\right)$, it is possible to approximate the appropriate value for b_{ff}, which is about

three times smaller than predicted in the first attempt.

The implementation of this second iteration damping term resulted in the damped system response shown in Figure 4.16, due to a 100 N force impulse, and Figure 4.17, due to a 1 N-m torque impulse. It is clear that the correlation is almost exact for the damping adjustment based on effective mass, and it is recommended that further investigation be made to increase the fidelity of this damping model by deriving the effective mass and frequency for a given, arbitrary system. An initial (planar) analysis is provided in Appendix B, however even this analysis only accounts for the simple force or torque input cases presented during this research.
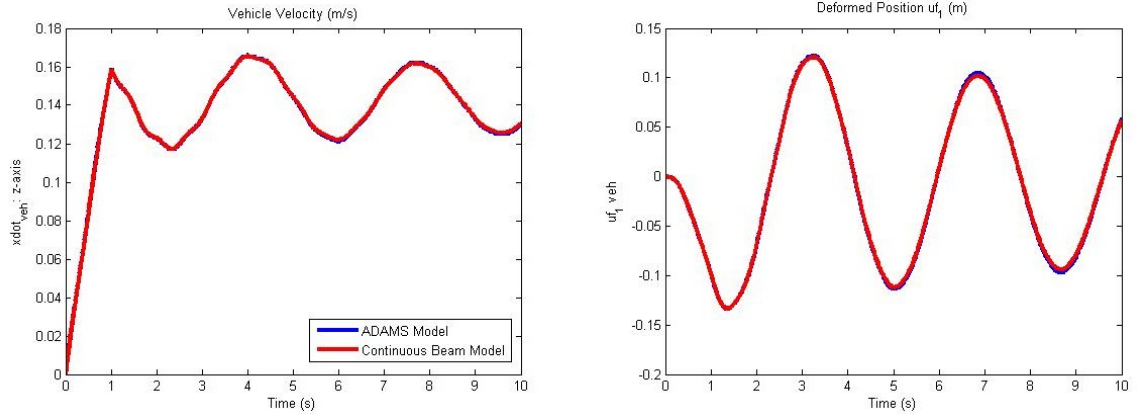
Figure 4.16: Iteration 2: Damped force input test case response for $\zeta = 0.025$.

4.5.5 Complex Input Profile

The last test case incorporates both force and torque input profiles to show how the flexible-body model can be used to simulate a more realistic system response. This more complicated interaction between spacecraft can be modeled by a weighted sum of inputs, and subsequently correlated in the same manner. For each test case,
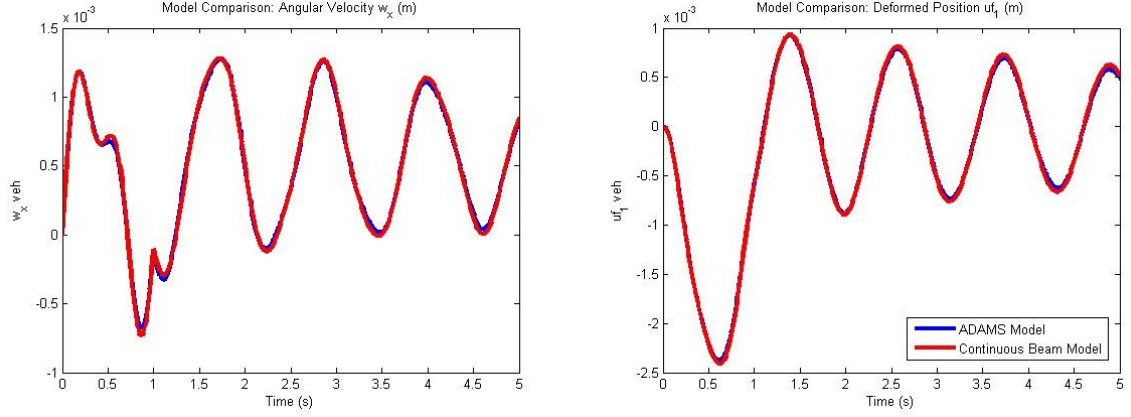
Figure 4.17: Iteration 2: Damped torque input test case response for $\zeta = 0.025$.

a force impulse of 200 N and a torque impulse of 200 N-m are applied simultaneously to the satellite hub for one second, and the vehicle velocity, deformed position and angular velocity are compared.

Since the continuous beam model assumes that each appendage can be represented as a cantilever beam, it is expected that this model only maintains its accuracy while the satellite hub mass remains large compared to the appendage mass. To investigate this further, multiple different values of satellite mass are used, and both the undamped and damped system responses are compared for each case.

4.5.5.1 Example Test Cases

For the first test case with a complex input, a near-infinite mass satellite hub (10^6 kg) is used to establish a baseline comparison, where the continuous beam model is expected to maintain a high degree of accuracy. The comparison in results for the undamped system is shown in Figure 4.18, where the predicted responses

according to the ADAMS^{TM} finite element or continuous beam models overlap with seemingly little error. The corresponding damped response for this satellite hub mass is shown in Figure 4.19, where the damping term is based on an infinite mass hub. Again, the rigid-body velocity and rotation match, along with the modal position of the appendage for the duration of the simulation. Note that in these first graphs, the two models match so closely that it is difficult to see the finite element model response.
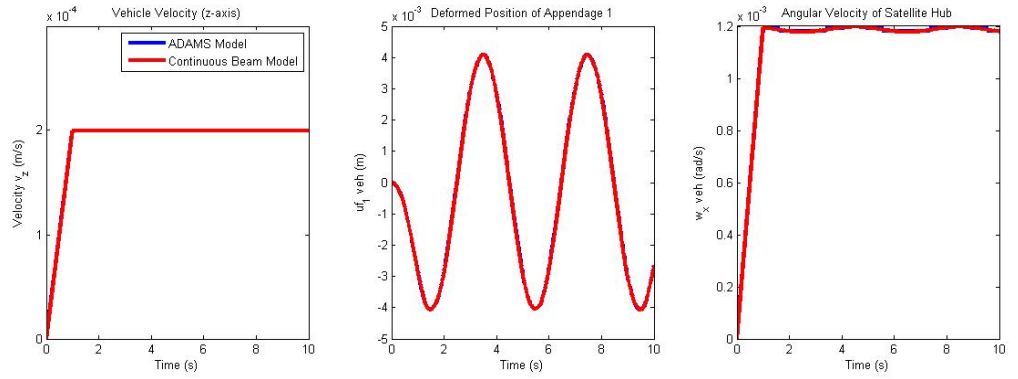
Figure 4.18: Undamped, complex test case response with $m_s = 10^6$ kg.
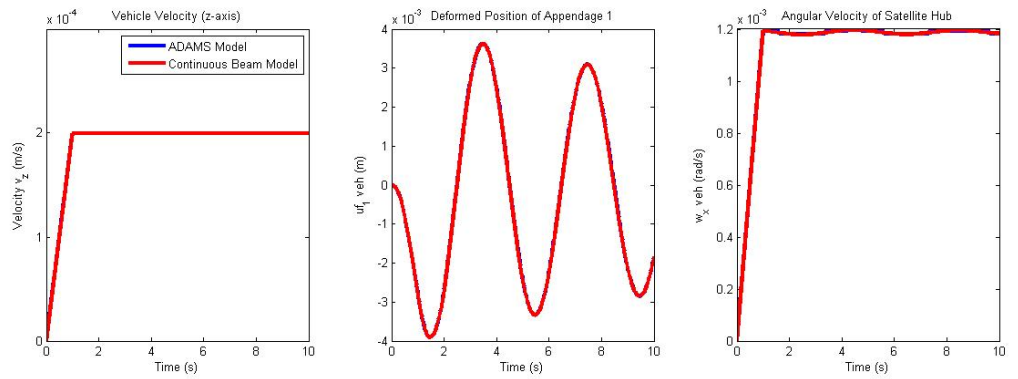
Figure 4.19: Damped, complex test case response with $m_s = 10^6$ kg.

For the second complex input test case, a satellite mass of 10^4 kg was input

to the continuous beam and finite element models, keeping the appendage characteristics the same as the previous test case, according to Table 4.1. Although the undamped system response shown in Figure 4.20 still shows a near-perfect correlation, the damped response of the system, shown in Figure 4.21, shows a small discrepancy between the two models. This is beginning to show the error introduced by the first iteration damping term, as the more complicated input profile directly affects the effective mass and corresponding natural frequency of the system. Since the approximation used in the second iteration damping term only compensates for a single mode shape, a more sophisticated damping model must be produced in the future to account for the linear combination of modes experienced due to the complex input profile.
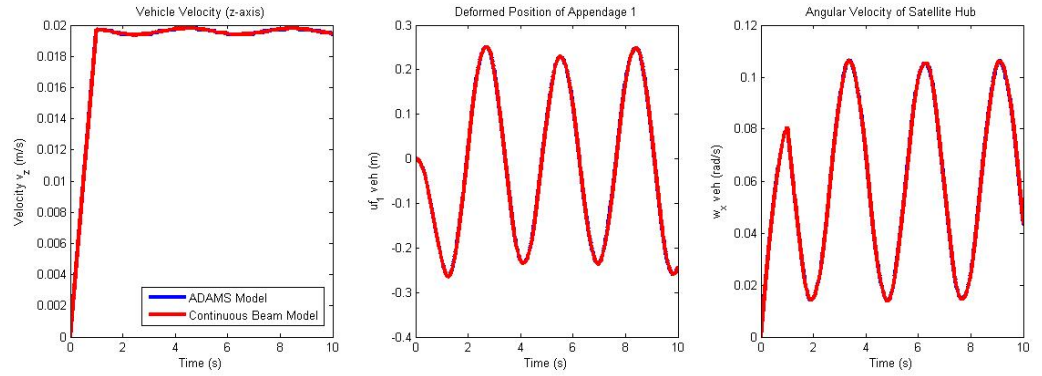
Figure 4.20: Undamped, complex test case response with $m_s = 10^4$ kg.

For the third complex input test case, a satellite mass of 500 kg was used in either model, again keeping the appendage characteristics the same as the previous test case. The undamped system response is seen in Figure 4.22, where the linear and angular velocity of the satellite hub, and deformed position of a single appendage are
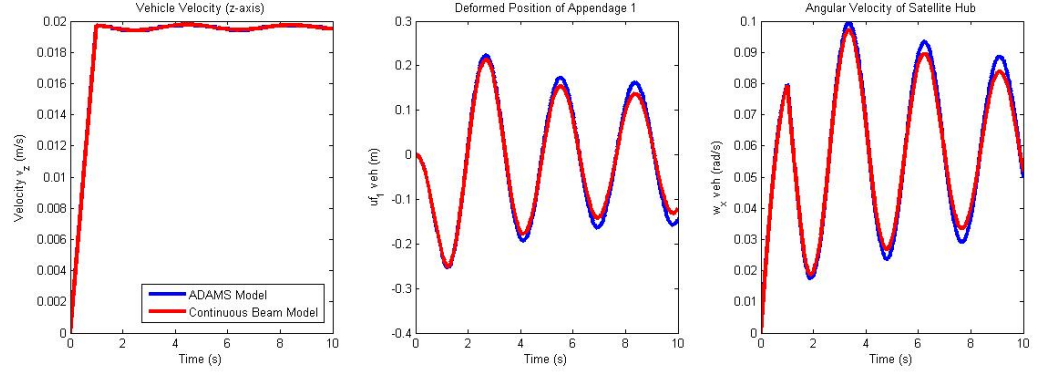
Figure 4.21: Damped, complex test case response with $m_s = 10^4$ kg.

plotted over time. Note that this complex input causes motion along the y-axis as well, which is the cause of the seemingly decaying vehicle velocity in the z-direction. As the velocity in the z-direction decreases, the y-axis component increases as the vehicle rotates in the YZ plane. The combined force and torque input causes a non-intuitive response, where the two appendages neither oscillate symmetrically nor asymmetrically relative to one another. This causes a combined translation and rotation, which causes the satellite to move in a spiral pattern, outwards.
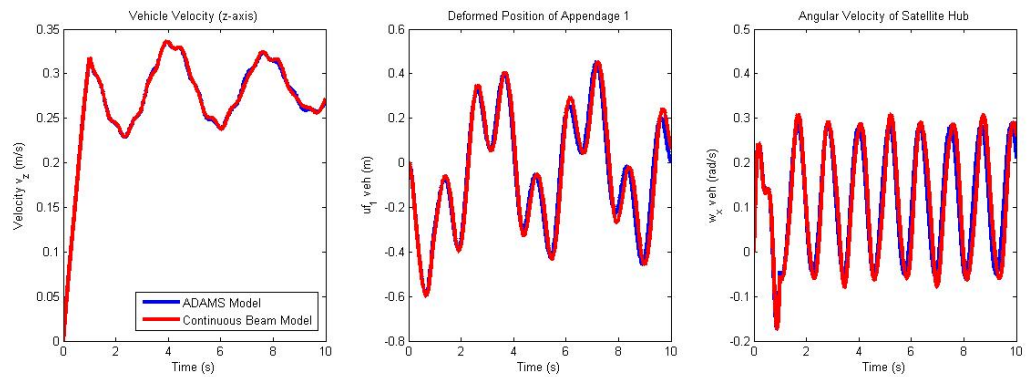
Figure 4.22: Undamped, complex test case response with $m_s = 500$ kg.

The damped response in Figure 4.23 continues to show progressive discrep-

ancy, where the current damping term approximation cannot compensate for this more complicated input profile. Although the damped system response does not correlate with the predicted response according to the finite element model, it is clear that the dominant response of the undamped case is still captured for the 500 kg satellite mass case. Only a small frequency discrepancy seems to exist between the two predicted responses as seen in Figure 4.22, which is likely attributable to the boundary conditions either model is assuming between the appendages and satellite hub. The difference between a free-free and cantilever beam directly affects the mode shape and frequency response of the system, and it is recommended that the transition between these two boundary conditions be studied if it is desired to solve this small discrepancy.
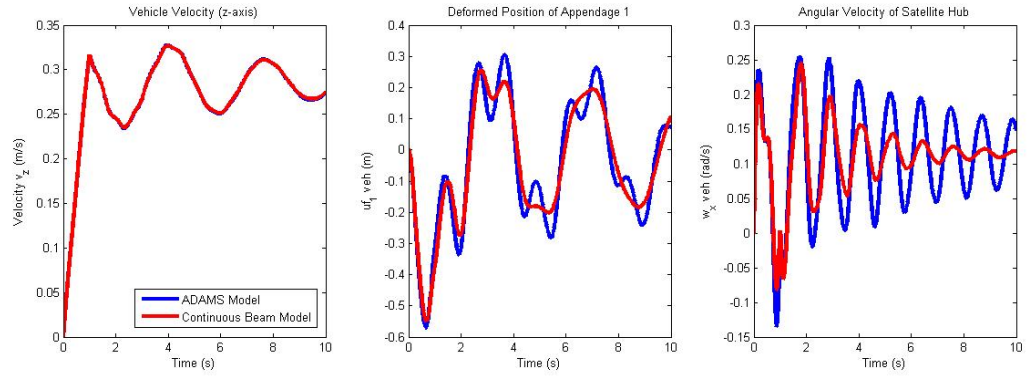
Figure 4.23: Damped, complex test case response with $m_s = 500$ kg.

4.5.6 Results and Discussion

All of the validation efforts conducted during this research rely heavily on the correlation of frequency between the predicted models. Thus, to summarize

the software validation effort presented, a set of tables was developed to provide a side-by-side comparison of the predicted system frequencies in different test cases. The system frequency is tabulated over a range of satellite hub masses for each category, as shown in Tables 4.2 and 4.3. Note that for each case, the appendage characteristics remain constant, so that the 500 kg satellite hub has a 5:1 ratio to the appendage mass, whereas the 2000 kg satellite hub maintains a 20:1 ratio. Realistic satellites vary in terms of this ratio, which is an additional reason why multiple hub masses were simulated.

It should be noted that the values provided in these tables are estimated from the continuous beam and finite element model predicted responses, and should only be used as a comparison to summarize general trends in the data. Due to the time-varying inertias and highly nonlinear coupled rigid- and flexible-body dynamic equations, it was not possible to use an eigenvalue analysis to calculate the system frequencies for each of these test cases. Instead, the frequencies were approximated by observing the time between peaks in the linear or angular velocity time response plots.

Table 4.2: Comparison of predicted first symmetric system mode frequency for GOES-class satellite.

m_s	Continuous Beam Model (Cantilever)	Finite Element Model (Free-free)
0.001 kg	0.39 Hz	0.486 Hz
500 kg	0.27 Hz	0.276 Hz
2000 kg	0.25 Hz	0.257 Hz
10^6 kg	0.25 Hz	0.250 Hz

Table 4.3: Comparison of predicted first asymmetric system mode frequency for GOES-class satellite.

m_s	Continuous Beam Model (Cantilever)	Finite Element Model (Free-free)
0.001 kg	1.2 Hz	1.105 Hz
500 kg	0.86 Hz	0.858 Hz
2000 kg	0.57 Hz	0.568 Hz
10^6 kg	0.25 Hz	0.251 Hz

By observing the system response for an infinite mass satellite hub (approximated by $m_s = 10^6$ kg), an important baseline comparison is achieved. Since the continuous beam model assumes that the mode shape of each appendage is represented by a cantilever beam, it is expected that this model will match the response as predicted by the non-real-time finite element approach. The correlation for a large satellite hub mass is because the appendage is well represented by a cantilever boundary condition whose base does not move. However, as the satellite hub mass decreases, the assumption that each appendage can be characterized by cantilever boundary conditions begins to break down, and instead become more accurately modeled as a beam with free-free boundary conditions. The difference between the mode shapes of these two boundary conditions is captured in Figure 4.24, where a key difference between a cantilever and free-free beam is the slope of the beam at the attachment point to the satellite. Although only half of the satellite system with a cantilever beam is shown, it is clear that the two boundary conditions do not match. Thus these two models do not predict the same motion of a satellite system with small mass (0.001 kg) relative to the appendage, as seen in Table 4.2.
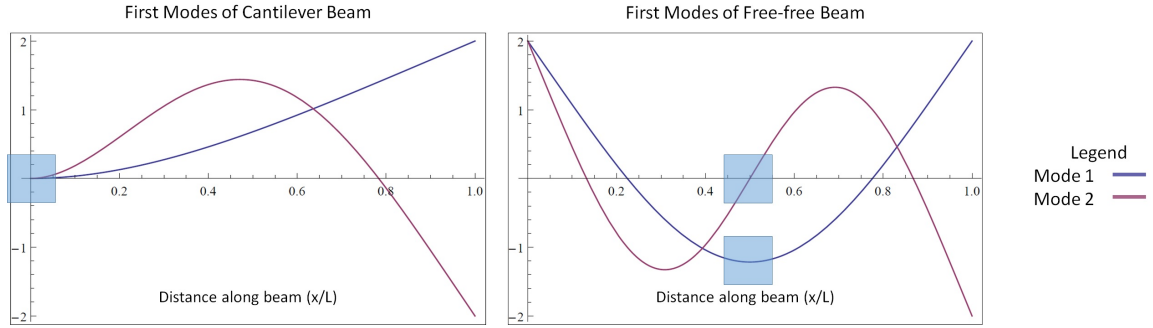
Figure 4.24: Comparison of cantilever versus free-free mode shapes.

An additional, direct comparison of the first two modes is given in Figures 4.25 and 4.26, which portray the given mode shapes as applied to a five meter long appendage. The satellite hub would be located at the origin in either figure, both of which show how different the two boundary conditions are, especially in the case of the second system mode.
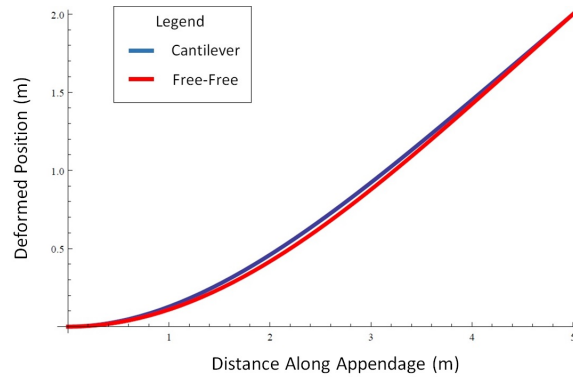
Figure 4.25: Comparison of first symmetric flexible mode for cantilever versus free-free boundary conditions.

At some point between a satellite hub mass of 500 kg and 0.001 kg, the free-free boundary condition of the ADAMS^{TM} model can no longer accurately approximate the same system response as the cantilever boundary condition used in the contin-
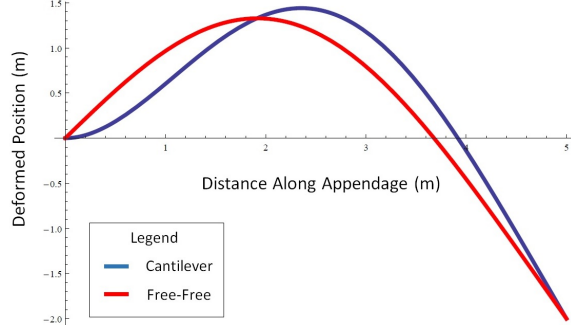
Figure 4.26: Comparison of first asymmetric flexible mode for cantilever versus free-free boundary conditions.

uous beam model. The mode shapes associated with these varying satellite mass ratios can significantly differ for a more complicated input profile, which consequently alters the natural frequency of the system for each case. An initial analysis describing the estimated effect of the coupled rigid- and flexible-body system on the system frequency is calculated [20] for both the symmetric (B.15) and asymmetric (B.19) test cases, however further research in this area is relegated to future work.

Since the class of satellites being studied during this research maintain higher satellite hub-to-appendage mass ratios, it is perhaps a reasonable assumption to use cantilever boundary conditions in the continuous beam model. It is noted though that the correlation presented only holds valid for certain ranges of mass ratios, and thus, the continuous beam model is expected to maintain greater accuracy for higher satellite hub-to-appendage mass ratios.

4.6   Summary

This validation effort featured four types of simulations including the undamped, damped, single and two-mode system response, where the spacecraft appendages were modeled either as two continuous cantilever beams or as a single free-free, finite element beam. Each set of these simulations was repeated for a force or torque input, where the single or dual-modes associated with the given input were observed (symmetric mode(s) for force input and asymmetric mode(s) for torque input). Excitation due to initial deflection of the appendages was shown to be the same as the force or torque input cases except that the center of mass of the spacecraft does not translate in the case of symmetric initial modal conditions, and does not rotate in the case of asymmetric initial modal conditions.

An additional analysis was conducted where a linearly weighted sum of inputs was experienced by the satellite system. The system response to this more complicated input profile was shown to be highly dependent on the ratio of masses between the satellite hub and appendages, and it was determined that the continuous beam model maintains its accuracy as long as the appendages can be represented as cantilever beams.

In all of the described test cases characterized by the parameters given in Table 4.1, it was shown that the continuous beam model derived from the coupled rigid- and flexible-body equations given by (3.1) agreed with the predicted response from an independently derived model. The introduction of a complex input provided a more realistic profile, and introduced additional insight about the transition of

mode shapes that characterize each appendage for more complicated inputs and different satellite geometries. Regardless, it has been proven that this model is able to accurately capture the coupled rigid- and flexible-body response of the given spacecraft system for certain ranges of satellite hub-to-appendage mass ratios, where the cantilever boundary condition remains a valid representation of the appendage flexible-body dynamics.

Chapter 5: Hardware-in-the-Loop Validation

An end-to-end validation effort was conducted to demonstrate how a simulation of the coupled rigid- and flexible-body dynamics can be used to model a physical system and successfully predict the motion of a given satellite system. This validation is achieved by using a robotic demonstration unit, the Motoman SIA-10 (Fig. 5.1) to interact with its environment and mimic the motion of a client satellite. By conducting a hardware-in-the-loop simulation, more realistic force and torque profiles can be input to the system, where the robot acts as a display to better visualize the resulting satellite motion.
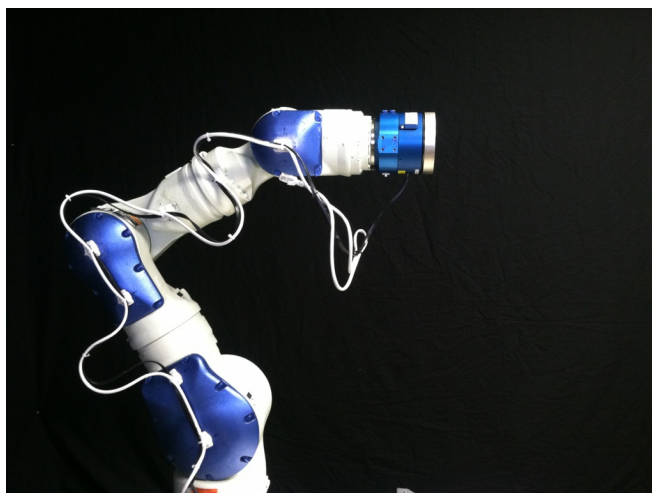
Figure 5.1: The Motoman SIA-10 robot used to visualize spacecraft motion.

Two cases will be conducted to correlate the result of the continuous beam

model to the response of a physical system. This validation effort is outlined in Figure 5.2, where the physical system response is compared to the predicted response of the full rigid- and flexible-body simulated response derived in this thesis.
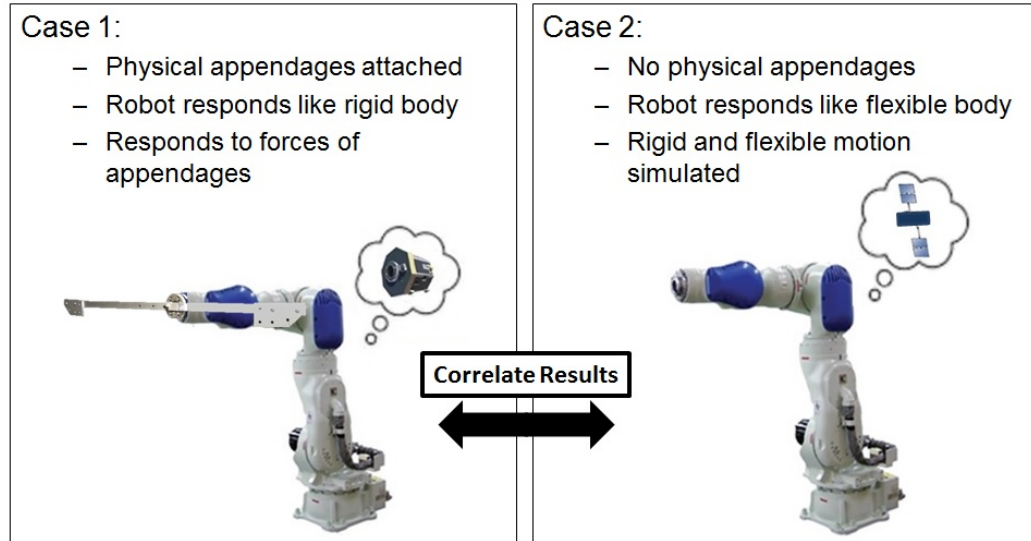
Figure 5.2: Correlation between predicted and actual flexible-body dynamics.

5.1 Case 1: Physical Appendages

The first test setup is shown in Figure 5.3, where two physical appendages are attached to the Motoman SIA-10 robot. This first effort aims to understand how a rigid-body satellite response is affected by the added flexible-body dynamics from two attached, physical appendages. Although the robot is only following the response of a rigid-body system, the interaction forces due to the oscillation of the physical appendages affect the rigid-body to create a coupled rigid- and flexible-body system, further depicted in Figure 5.4. This diagram shows how an external input such as a force or torque is applied to the satellite system, measured by a force/torque

sensor. The flexible appendage motion is also captured by the force/torque sensor, which is located between the robot tool tip and interface plate used to attach the two physical appendages. The measured forces resulting from the oscillatory motion of the appendages are input to the rigid-body dynamic script which predicts the response of the satellite system. This predicted motion is visualized by the robot, which is continuously influenced by the appendage oscillations in real-time.
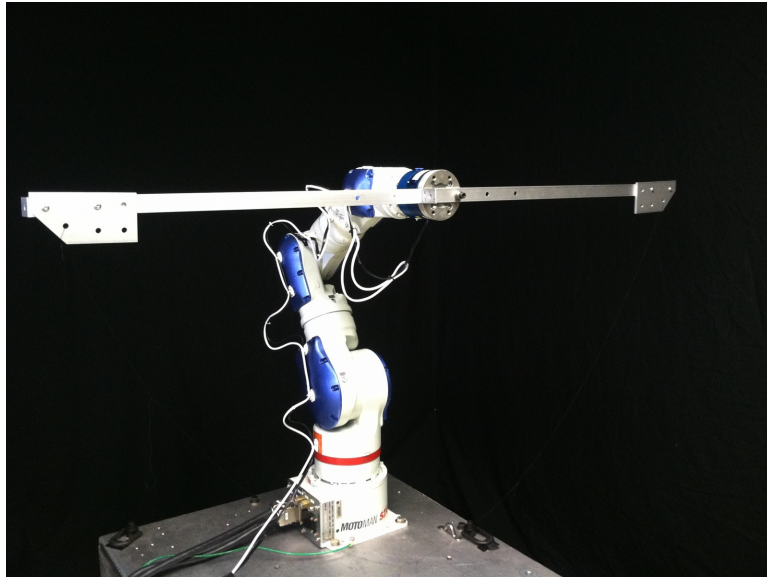
Figure 5.3: Motoman SIA-10 robot with physical appendages attached.

5.2 Case 2: Simulated Appendages

The second test features no physical appendages, where the robot now simulates the response of both the rigid-body hub and flexible satellite appendages. Figure 5.5 portrays an overview of this system, where the input force and/or torque profile is input to the combined rigid- and flexible-body satellite model, which was developed in Chapter 3. The predicted system response is input into the robot con-
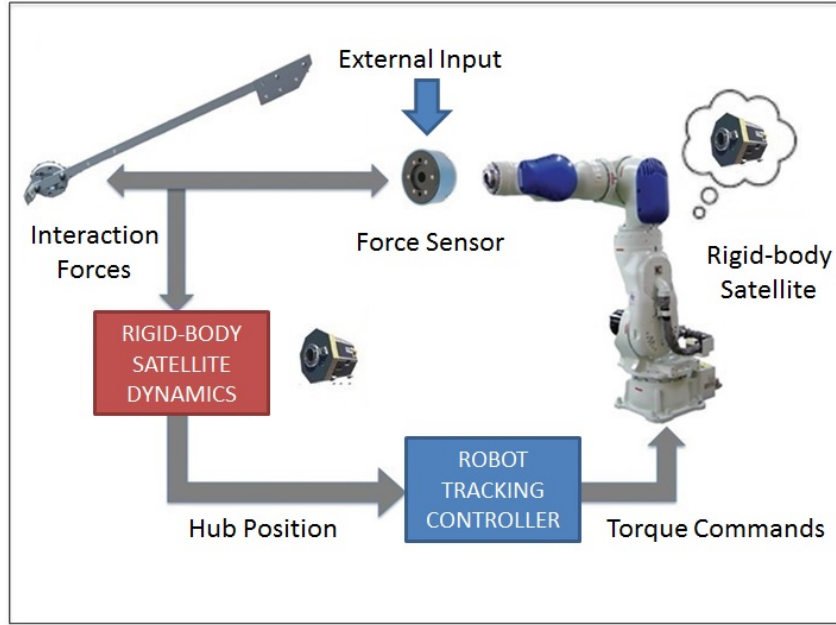
Figure 5.4: Diagram of rigid-body simulation with physical appendages.

troller so that the Motoman SIA-10 tracks the response of this more complicated
spacecraft, and the resulting dynamics can be compared to the response of the ac-
tual appendages from Case 1. Note that the capability to replay the same input
profile in both cases was not available in the current robot software package. Thus
although the data from Case 1 included the measured data as affected by unmodeled
effects such as delay in the robot system, the response as predicted by Case 2 was
actually the output of the flexible-body dynamics simulation prior to being input
to the robot controller. For this reason, the response did not include any delays or
inaccuracies due to the robot tracking controller.

In this second test, since the Motoman robotic demonstration units only show
the motion of the satellite hub, it is of interest to produce a visualization script
to depict the flexible system motion over time as shown in Figure 5.6. This added

Figure 5.5: Diagram of flexible-body simulation with no physical appendages attached.

capability makes it easier to compare how the appendages react to a given set of inputs, and allows for a direct comparison between the predicted and actual flexible-body response.

5.3 Summary of Parameters

In order to conduct Case 2, it is necessary to create a model of the physical appendages used in Case 1. After deriving the structural parameters that characterize the appendage's flexible-body dynamics, this model can be input to the coupled dynamics simulation to predict how the actual system responds to various input forces and torques.

A summary of the satellite hub and appendage parameters used in Cases 1

57

Figure 5.6: Visualization of physical appendages attached to the Motoman SIA-10 robot.

and 2 is given in Table 5.1, where the satellite hub is assumed to have a simple cube shape and the geometry of each appendage resembles a cylindrical boom. Note that the two modeled appendages are assumed to have the same structural properties and be symmetrically oriented about the satellite hub.

Table 5.1: Satellite parameters used for Cases 1 and 2.

	m (kg)	L (m)	$I_{o_{prin}}$ (kg-m^2)	EI (N-m^2)	ζ
Satellite	50	1	8.33, 8.33, 8.33	-	-
Appendage	0.8341	0.635	0.112, 5.26e-5, 0.112	0.4608	0.00715

The constructed appendages used in Case 1 (seen in Fig. B.3) each feature a tip mass, which is approximated as a distributed mass along the beam. The beam's effective mass, structural rigidity and damping ratio are derived in Appendix B, and are shown in Table 5.1. Although each parameter is determined by observing

the response of the physical system in Case 1, the actual values are input into the flexible-body model to find the predicted response, during Case 2.

5.4 Demonstration of Predicted Physical System Response

The hardware validation effort will be split into two parts. In the first part, the robot remains static (or inactive) to simulate an infinite mass satellite hub, where the appendages behave very similar to cantilever beams. The pure modal response can then be compared to the predicted appendage motion, without the involvement of any rigid-body coupling. In the second part, the robot is activated to validate the coupled rigid- and flexible-body dynamics.

5.4.1 Validation of Flexible-Body Dynamics

As a check of the pure modal satellite dynamic response, a simulation is conducted where the robot remains inactive. With the robot simulating a near-infinite satellite hub mass, the two appendages are given an initial modal position and the uncoupled flexible-body dynamics are observed.

Unfortunately, since the appendage tip location was not measured directly, it was necessary to instead correlate the wrench (force and torque) profile experienced by the satellite hub during this correlation effort. This measurement can be thought of as an estimate of the loads that the attachment point between the satellite hub and appendage would have to endure for a given input profile. In Cases 1 and 2, this value is simply read from the force/torque sensor between the robot and appendages,

and by extracting this quantity from the continuous beam, flexible-body simulation results it is possible to directly compare the modal response of the system.

The results of this correlation effort are summarized in Figure 5.7, which shows both the predicted and measured forces experienced by the satellite hub. The close correlation proves how the physical system has been successfully modeled using the aforementioned derived structural parameters. The fact that the predicted and actual responses diverge slightly as the simulation continues is an expected result, likely attributed to the accuracy of the measured structural parameters.

This hypothesis is proven by referring to the plot of measured structural rigidity, in Figure B.5, which shows that the two appendages are characterized by different stiffness values. Since the predicted response assumes each appendage is characterized by the average stiffness value between the two appendages, there is a slight discrepancy in frequency between the predicted and actual responses, shown in Figure 5.7. Since the first appendage is slightly less stiff than the average value used for the simulation, given in Table 5.1, the physical system has a slightly lower frequency than the predicted value. Likewise, the second appendage was proven to have a higher stiffness and thus exhibits a higher frequency than the predicted response from the MATLAB, continuous beam simulation.

5.4.2   Validation of Coupled Dynamics

Now that the purely modal response of the physical appendages has been correlated with the predicted response from the derived continuous beam model, the
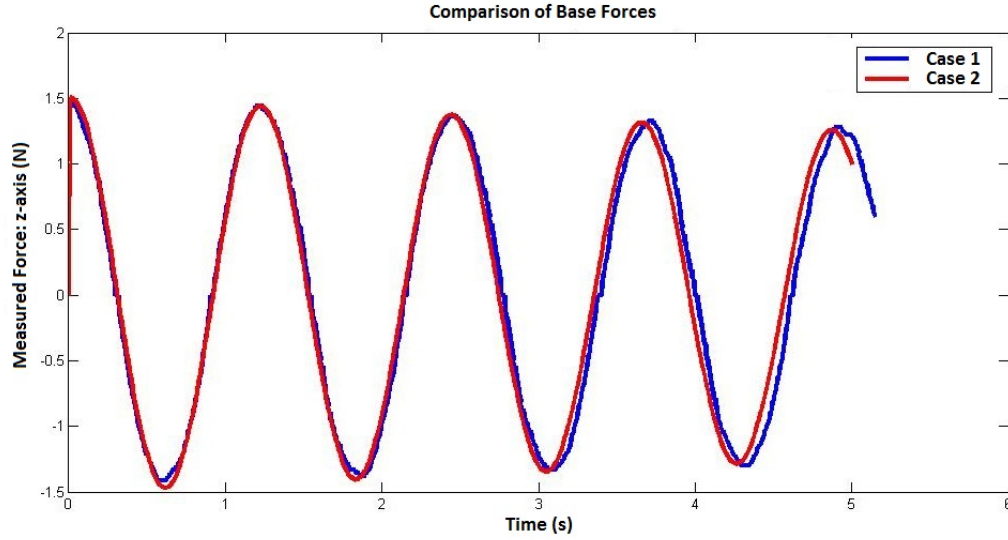
Figure 5.7: Comparison between simulated and physical response of the system to an initial modal position.

fully coupled rigid- and flexible-body dynamics must be validated against hardware. To accomplish this task, a set of test cases are developed which directly excite the physical or simulated appendages. Instead of introducing an external force or torque to the satellite hub itself, a more exaggerated motion can be accomplished by applying forces directly to the appendages. To apply this input, a piece of thread was tied to the end of each appendage, and a short-duration pull excited the symmetric modes. A pulley system was used to excite the asymmetric modes, such that a single pull of the thread would cause the two appendages to oscillate asymmetrically to one another. Since these two types of excitation occur over a short time interval, either input profile can be simulated by the combination of a force (or torque) input to the satellite hub and an initial modal position for each appendage.

For this validation effort, the force input recorded during the hardware-in-the-

loop test in Case 1 is input into the coupled flexible-body dynamics used in Case 2. Although the exact force input is entered into Case 2, the initial modal position must be estimated from video recordings of each test. This measurement is made directly after the external impulse ends, characterized by the location of the first peak in the force/torque measurements. Since only the external input profile is input to the simulation in Case 2, this is also the time that the force/torque input profile from Case 1 stops being read in to the flexible-body script. In this way, the entire profile of external forces are input to Case 2, and the resulting motion is compared with the physical response of Case 1.

5.4.2.1   Symmetric Modes Excited for 50 kg Satellite Hub

The first example of this coupled dynamics validation effort involves a 50 kg satellite hub, with parameters described in Table 5.1. Figure 5.8 shows the correlation between Case 1, or the measured hardware data, and Case 2, which includes the simulated system response as predicted by the flexible-body dynamics model. A delay is shown to exist beween the hardware and simulated responses due in part by the robot bandwidth, which is known to be approximately 2-3 Hz. Although this bandwidth is above the frequency the robot is trying to react to, (a 1 Hz oscillation of the appendages), a greater bandwidth would help to mitigate the non-negligible delay.

By approximating this delay, the data can be shifted to observe the true correlation plot, seen in Figure 5.9. From the comparison of hub position, it is clear that
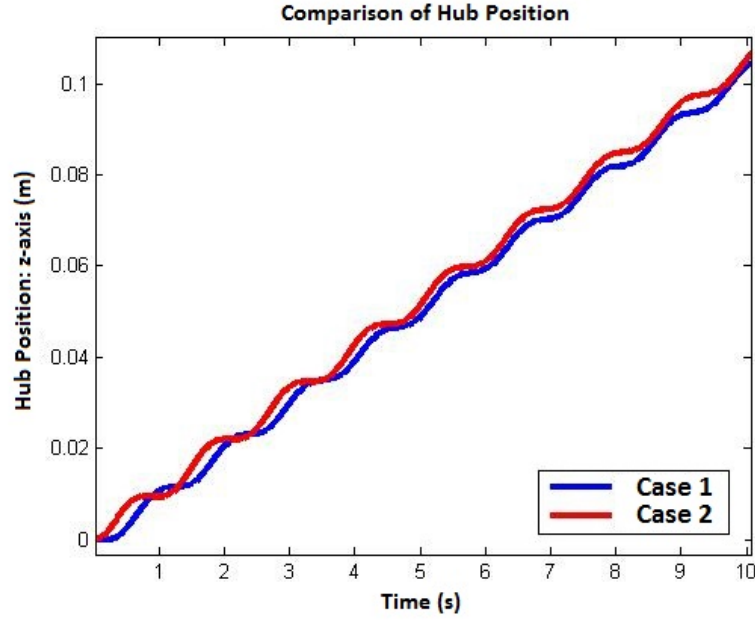
Figure 5.8: Delay between simulated and physical system symmetric flexible-body response for 50 kg satellite hub (initial deflection of 10 cm).

the resulting motion of the flexible-body system from Case 1 matches the simulated response from Case 2, with a slight discrepancy in frequency. This difference in results can be better understood by observing the plot of the error in hub position, where the difference between these two cases is plotted over time. Note that over the given simulation time, there only seems to be a maximum magnitude difference of approximately 6 mm (3% of total translation), which further proves the ability to capture the dominant motion of the system.

The plot of error in hub position, also from Figure 5.9, indicates the presence of a beat frequency, which is caused by a slight difference in oscillation frequency between the two appendages, as was present in Figure 5.7. This frequency discrepancy is again explained by the difference in the stiffness of either appendage shown
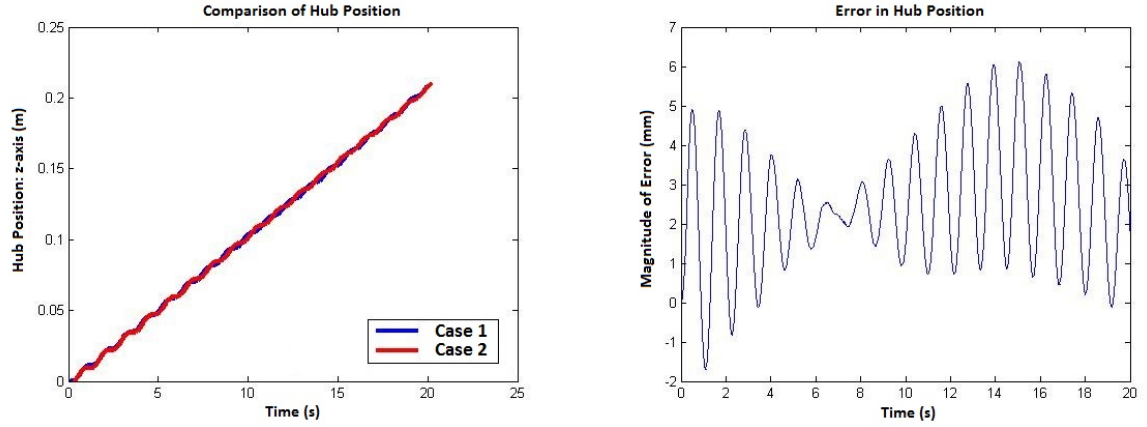
Figure 5.9: Correlation between simulated and physical system symmetric flexible-body response for 50 kg satellite hub (initial deflection of 10 cm).

in Figure B.5, which shows a clear distinction between the experimentally calculated values of structural rigidity for the two constructed appendages, made of a low-grade aluminum. The difference in measured structural rigidity of approximately 0.3 N-m^2 corresponds to a difference of 0.028 Hz in the calculated frequency of the two appendages.

From close observation of the hub position error plot in Figure 5.9, it is estimated that the half-cycle of this beat frequency is around 18 seconds. This would give a period of 36 seconds, which corresponds to a frequency of about 0.028 Hz. Thus, it is plausable that this difference in measured structural rigidity is indeed the cause of the frequency discrepancy.

Although this difference is likely the main contributor to the frequency discrepancy, another possibility that could have affected this response includes the method used to mount each appendage. Since both appendages were mounted onto the Motoman robot as seen in Figure 5.3, there is a slight overlap such that the

two screws each pass through both appendages, as an attempt to form a more rigid attachment. This overlap and the position, being either underneath or on top of the opposing appendage, could also affect the difference in performance.

Thus, the discrepancy between responses of either Case seen in Figure 5.9 is attributed to the fact that the predicted response from Case 2 does not include the non-symmetric traits actually present in the physical hardware.

5.4.2.2   Symmetric Modes Excited for 100 kg Satellite Hub

As an additional example, a similar input profile from the previous example is input into both Case 1 and Case 2, this time with a larger, 100 kg mass satellite hub. Since the satellite hub is assumed to have the same geometry as the previous case, the inertia used in this example can be found by directly scaling the value in Table 5.1 for the 50 kg mass satellite hub. In other words, instead of using a principle axis of inertia of 8.33 kg-m^2, this example uses an input of 16.7 kg-m^2.

The response shown in Figure 5.10 shows better correlation than the previous case, however introduces additional sources of error in the test setup. Although the general response seems to agree and the same beat frequency exists from the previous example, an additional source of error is evident in the parabolic shape of the hub position error over time.

The most likely cause of the slightly mismatched hub position profile between the two cases is a small difference in initial position of either appendage. For the actual input, this means that the two appendages were not pulled with the same
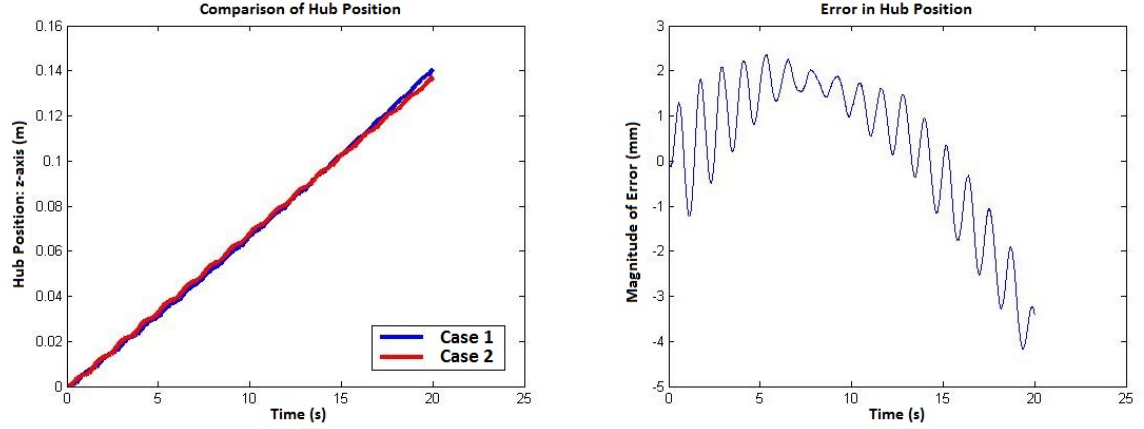
Figure 5.10: Correlation between simulated and physical system symmetric flexible-body response for 100 kg satellite hub (initial deflection of 8 cm).

force, causing a non-zero torque input in addition to the expected symmetric appendage motion. Upon closer inspection of the video and recorded data set of the given example, a non-zero torque input is indeed experienced, as seen in Figure 5.11. Note that the increasing torque measurement over time is due to the fact that the appendages do not oscillate perfectly symmetric to one another. As the simulation continues, the oscillation of the two appendages become more asymmetric, causing more energy to go into rotation instead of purely translation. Although this exact profile was input to the flexible-body model for Case 2, this means that the initial conditions of either appendage were not the same in the physical system, in Case 1. This discrepancy is not modeled in Case 2 due to the difficulty of predicting the exact initial modal position of either appendage, and it is recommended that a direct measurement of modal position is used in future test scenarios to improve the correlation effort.
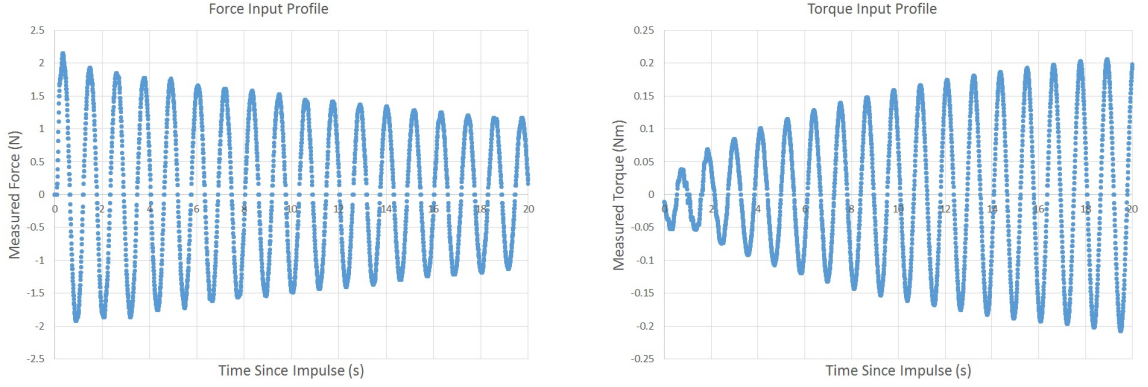
Figure 5.11: Measured input profiles for 100 kg satellite hub exhibiting symmetric flexible-body excitation due to an initial force impulse.

5.4.2.3 Asymmetric Modes Excited for 250 kg Satellite Hub

An example of exciting the asymmetric modes was also produced, where the two appendages were pulled with equal and opposite forces. This type of input results in 180° asymmetric appendage motion and a net torque appled to the hub. The excitation on the system can be thought of as a combination of an initial modal position and a torque impulse exerted on the satellite hub.

For this test case, a larger (250 kg) satellite hub is used with the same geometry and corresponding principle axes of inertia of 41.7 kg-m². These parameters were entered into Cases 1 and 2, and the corresponding responses (predicted or actual) are compared in Figure 5.12. From this plot, it is clear that the dominant response of the physical, measured system data is captured by the simulated, predicted response.

Similar to the symmetric flexible-body response from the previous example, the frequency discrepancy is attributed to a lack of symmetry in the applied input profile. In this case, a slightly imperfect asymmetric excitation causes a small frequency

67
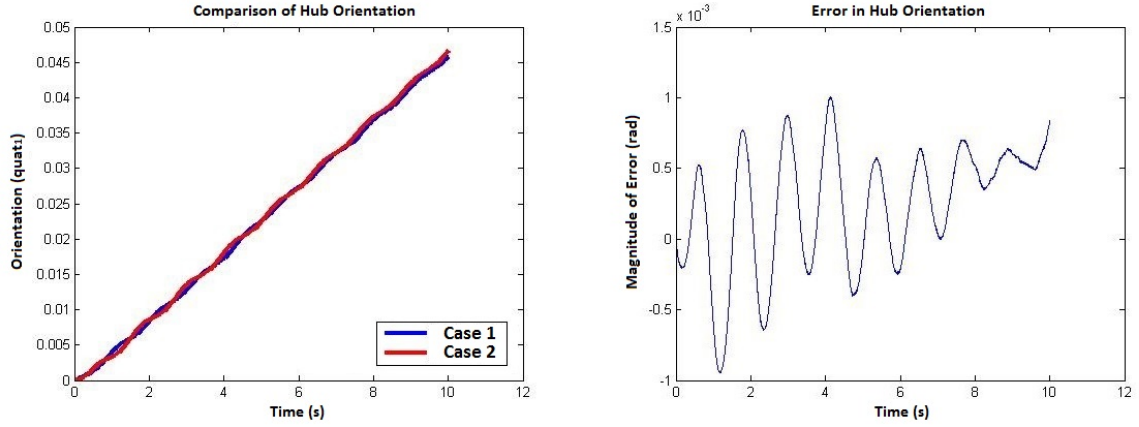
Figure 5.12: Correlation between simulated and physical system asymmetric flexible-body response for 250 kg satellite hub (initial deflection of 8 cm).

shift, as again the appendages oscillate at different frequencies, mostly due to the inaccuracies of how the input is applied to each appendage and the slight difference in structural rigidity between the two appendages.

By observing the force and torque input profiles as experienced by the satellite hub (Fig. 5.13), it is evident that the symmetric flexible-body modes are slightly excited in addition to the expected, asymmetric modes. Note that a dead-band of 0.1 N was used to limit the effect of noise, which is evident in Figure 5.13. Even though the magnitude of the force profile is small compared to the torque experienced by the satellite hub over time, this non-negligible value proves to affect the system response, changing the frequency of the orientation plot compared to the predicted response of Case 2, as seen in Figure 5.12.
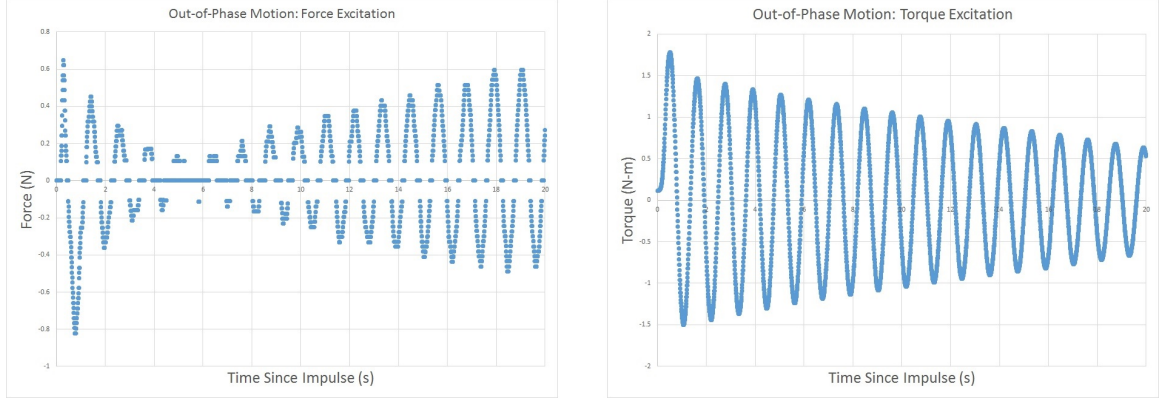
Figure 5.13: Force and torque input measured from asymmetric flexible-body response for 250 kg satellite hub.

5.4.3   Results and Discussion

A summary of the hardware validation effort is shown in Tables 5.2 and 5.3, which provide a side-by-side comparison of the predicted and actual system frequencies in the test cases presented in this research. Recall that the predicted system frequencies are estimated from the continuous beam and finite element model results, and should only be used as a comparison to summarize general trends in the data. The physical hardware frequencies are calculated from the experimental data, and might be subject to additional external influences that are not captured in the predicted responses.

Although the infinite mass case could be simulated by keeping the robot rigid, it was not possible to simulate a near-zero satellite hub mass. This was due to the limitation of the robot motion, as the Motoman SIA-10 is only capable of simulating the response of a satellite greater than approximately 25 kg.

69

Table 5.2: First symmetric system mode frequency comparison for physical hardware.

m_s	Continuous Beam Model (Cantilever)	Finite Element Model (Free-free)	Physical System
0.001 kg	1.31 Hz	1.53 Hz	-
50 kg	0.83 Hz	0.830 Hz	0.89 Hz
100 kg	0.82 Hz	0.826 Hz	0.88 Hz
10^6 kg	0.82 Hz	0.822 Hz	0.82 Hz

Table 5.3: First asymmetric system mode frequency comparison for physical hardware.

m_s	Continuous Beam Model (Cantilever)	Finite Element Model (Free-free)	Physical System
0.001 kg	3.6 Hz	3.608 Hz	-
50 kg	0.83 Hz	0.833 Hz	-
100 kg	0.83 Hz	0.827 Hz	0.89 Hz
10^6 kg	0.82 Hz	0.822 Hz	0.82 Hz

With the addition of data representing the physical system, it is important to discuss the inaccuracies that lead to discrepancies when compared to the predicted response. For example, Tables 5.2 and 5.3 show that the physical system exhibits a higher frequency than the predicted motion, calculated by either the continuous beam or finite element model.

One possible cause of this frequency discrepancy is in the estimation of structural parameters, such as the stiffness calculation for each appendage. An additional contribution to this difference can be attributed to the inevitable excitation of more than the first couple of system modes during the physical hardware tests. Such an excitation could also be caused by the non-uniform tip mass on each appendage, seen

in Figure 5.3. These higher order modes contribute a higher frequency to the overall system response when compared to the pure symmetric or asymmetric appendage response predicted by the cantilever beam or finite element models.

Regardless of these discrepancies, a general trend in the data still exists, that the accuracy of the continuous beam model is directly related to the ratio of satellite hub-to-appendage mass. Since the physical hardware features appendages with much smaller mass compared to the satellite hub, the predicted system frequency shown in Table 5.3 does not seem to change much between the test cases. It would be necessary to use heavier appendages in future tests to increase the range of hub-to-appendage mass ratios, since it is not possible to simulate a smaller mass satellite hub due to the control bandwidth limitations of the Motoman SIA-10 robot.

5.5   Summary

The equations of motion derived in Chapter 3 have been used to successfully model a physical system that resembles a spacecraft with realistic structural parameters. Although the software validation provided confidence in our ability to conduct a flexible-body simulation, the additional hardware validation effort further demonstrated the ability to model a physical system and simulate its response over time.

By comparing the response of a physical system in Case 1 to the predicted response shown by Case 2 for multiple inputs, the derived flexible-body model was shown to successfully capture the dominant response of a physical system.

Chapter 6:   Conclusions and Future Work

6.1   Summary

The key contribution of this research was the development of a reduced-order, coupled rigid- and flexible-body model that runs in real-time. This 1-DOF continuous beam representation of a flexible-body system was proven to accurately portray the first two flexible system modes of an appendage such as a solar panel or boom, given a particular force and torque input profile. Finally, by adding a description of these flexible-body dynamics to the current RDT rigid-body model, a case study was developed to compare the predicted and actual performance of a given physical system.

A total of three different types of models were developed during this research effort: a model of the purely rigid-body dynamics; a model of the first two flexible-body modes of a satellite; and a model of the first four flexible-body modes of the coupled system. There were also three different platforms used to develop a total of seven models, shown in Figure 6.1. The initial development effort featured satellite dynamics models created in MATLAB, whereas the software validation effort mandated the use of an independent software platform, which was chosen to be ADAMS^{TM}. In order to work towards utilizing a real-time system within

NASA's Robotic Demonstration and Testing (RDT) architecture, it was necessary to convert the flexible-body dynamics code to yet another software package [21], capable of real-time implementation. This platform enabled the use of mutiple robotic demonstration units such as the Motoman SIA-10 robot, utilized during the hardware tests presented in Chapter 5.

It is important to note that the software validation efforts (comparing the MATLAB continuous beam and ADAMS^{TM} finite element simulation results) featured the coupled dynamics and first four flexible-body modes whereas the hardware validation efforts used the simpler, two mode flexible-body model to capture the dominant system dynamics of the physical system. Although it is of future interest to increase the fidelity of the RDT model to include four system modes, this was not a priority during this research effort.

Platform	Rigid Dynamics	Coupled Dynamics 2 System Modes	Coupled Dynamics 4 System Modes
MATLAB	x	x	x
ADAMS		x	x
RDT/C++	x	x	

Fidelity Increases

Figure 6.1: Summary of models created to increase the fidelity of the current RDT satellite dynamics simulations.

6.2   Achievements

This research effort investigated the flexible-body dynamics of a client satellite that might be evoked by the interaction with a robot servicer spacecraft. By describing the coupled rigid- and flexible-body equations governing the motion of this client satellite, it was possible to observe its response due to an external input profile. A continuous beam model was created from these derived dynamic equations, and a set of input types were defined. It was shown how a linear combination of these inputs could produce a more realistic profile as might be seen during a satellite docking maneuver or subsequent servicing tasks on-orbit.

In order to assess the performance of the developed continuous beam model, an independent finite element model was constructed in ADAMS^{TM} for comparison. This software validation effort featured the correlation of both undamped and damped system responses for a range of input profiles and parameters describing different satellite systems. Through this effort, it was proven that the continuous beam model derived in MATLAB was able to accurately model the flexible-body response, for the nominal set of satellite parameters.

Furthermore, a demonstration was conducted to show how the derived continuous beam model can be used to predict the motion of a particular satellite. In this additional effort, the coupled dynamics were incorporated into a real-time system and tested during multiple hardware-in-the-loop simulations utilizing a Motoman SIA-10 robot. By comparing the predicted response as dictated by the derived equations to the actual response of physical appendages, it was possible to prove

that the continuous beam model could simulate a physical system.

In the end, a higher-fidelity simulation was developed which is able to describe the coupled rigid- and flexible-body dynamics of an arbitrary satellite system. Multiple validation efforts were conducted to simulate the response of a client satellite to a given input profile as seen in Figure 6.2, where the addition of real on-orbit data would add the potential for a final correlation effort.
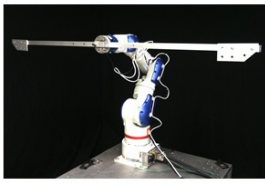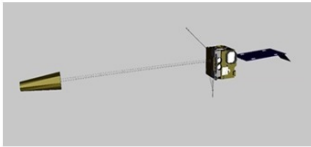
Figure 6.2: Validation effort summary: simulated versus physical components.

6.3 Future Work

This research effort builds the foundation for more realistic simulations, as it is possible to expand the single-DOF flexible-body model to evaluate flight-like systems and entire closed loop simulations. Since flexible bodies have the potential to contribute a significant amount of motion to the spacecraft system, it is imperative

that studies on simulations similar to those presented continue to classify how these dynamics will affect future missions. As one example, it is crucial to understand whether or not the initial contact during grapple will excite the flexible modes of long booms and solar arrays, which might have a direct impact on the success of an end-to-end satellite servicing mission.

6.3.1   More Realistic Simulations

One eventual goal of the developed model is to conduct a closed-loop hardware simulation of an entire grapple maneuver, similar to an actual satellite servicing mission. This would feature a Motoman SIA-10 robot simulating the servicing spacecraft grappling a Rotopod robotic demonstration unit, portraying the characteristics of a client satellite's combined rigid- and flexible-body dynamics. This scenario, seen in Figure 6.3, would supply a more realistic wrench profile, and could act as a platform to test various control logic in an attempt to minimize the effect of excited flexible modes [22]. This also supplies an advanced testbed to determine approach velocities and satellite servicing procedures which might have a lesser chance of exciting the flexible appendages on a client spacecraft, avoiding the possibility of damaging the spacecraft.

Before it is possible to develop such a complex setup, however, a larger sample of test cases must be conducted on the hardware system, starting with the testing of satellites with non-symmetric geometries and non-trivial configurations such as GOES or TDRSS. These spacecraft will not respond as intuitively as the

Figure 6.3: Future grapple sequence test setup.

aforementioned simple satellite model tested in the initial flexible-body motion implementation, which will make for a more extensive validation effort.

One possible future goal of this research might be to import a reduced NASTRAN^{TM} model of a given client satellite like GOES [23], and determine high level mission requirements by observing the interaction with the servicing spacecraft on-orbit. One difficult aspect of this future work will likely be finding a way to extract the necessary information from a NASTRAN^{TM} model, to input into the coupled rigid- and flexible-body dynamic simulation.

These additional simulations will further validate the ability of the derived continuous beam model to simulate a large range of potential client satellites, and can be used to classify how flexible-body motion will impact an end-to-end satellite servicing mission.

As a possible way to mitigate the effect of appendage excitation, it may be of interest to demonstrate the implementation of a spatial filtering method [24]. By using an active material such as a piezo-electric film, it might be possible to sense

and control the given appendage without adding mass or structural complexity. It is notable that this method has been proven to have a high spatial resolution and is capable of achieving on-board processing, self-calibration and self-temperature compensation.

6.3.2 Increasing Fidelity of Current Model

The most natural first extension to the presented research would be to extend the flexible dynamic description to additional degrees-of-freedom, allowing the observation of flexibility about other axes and including torsional and extensional terms. Although this would not add significant motion in the given test cases within the scope of this research project, it is easy to imagine more complicated spacecraft configurations and input profiles. To facilitate additional complexity, it will likely be necessary to develop a convention regarding how various appendages are attached to the satellite hub. Thus for a more complicated satellite configuration, an arbitrary number of appendages could systematically be incorporated at various locations relative to the satellite hub. In addition, more complicated mode shape descriptions might be necessary, including a different boundary condition assumption that is neither purely free-free nor cantilever. A similar effort, it might be of interest to investigate where this transition between boundary conditions takes place for a given satellite system. More complicated damping models can also be added to the current model, which might account for more complicated motion due to arbitrary input profiles and satellite geometries.

6.3.3 Additional Validation Efforts

Since the current version of the flexible-body equations of motion have only been shown to simulate the response of input forces and torques directly applied to either the satellite hub or appendage tip, it is of interest to develop a way to study how the given system would respond to an input with arbitrary temporal and spatial distributions. By studying other input profiles, it might be possible to make more conclusions about the resulting motion of various spacecraft. One example could be to correlate data from a hardware-in-the-loop simulation of an external, time-varying force, where a person is able to interact with the robot as seen in Figure 6.4 to create a more realistic input profile.
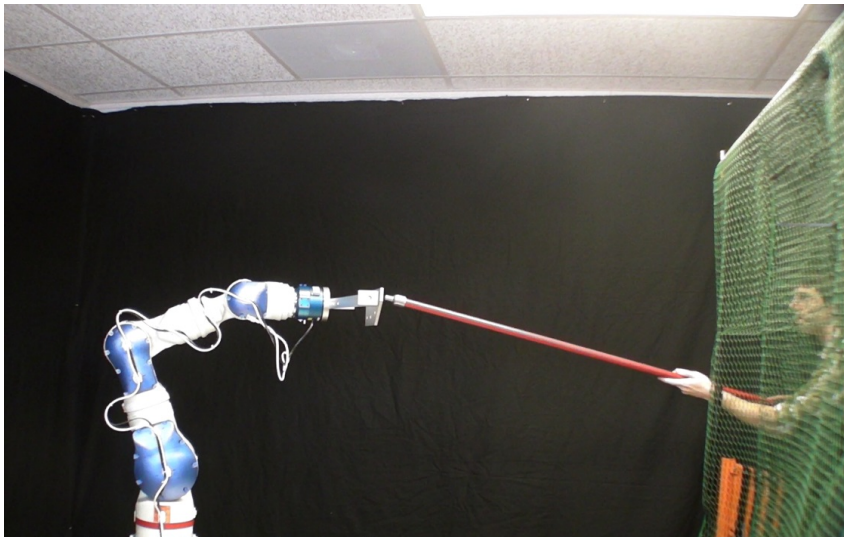
Figure 6.4: Hardware test setup for force input, featuring physical appendages.

In addition, it is suggested that future hardware tests include instrumentation to directly measure the appendage tip location over time. This would allow for a direct comparison of the modal response, and would minimize the error invoked by

the current test setup.

Ultimately, the goal is to work towards the simulation of a realistic satellite system with non-uniform geometries, for which case the current continuous beam model assumptions would no longer be valid. For this reason, a follow-on research effort could involve using finite element analysis as way of describing more complicated appendages. Note that this research is closely related to goal of importing a NASTRAN^{TM} satellite model directly into the simulation, however the method currently used to develop the system equations of motion will likely need to be altered.

6.3.4   Additional Application of Research

One additional way that the technology developed during this research effort could be used is in the design of future spacecraft, which are likely to have larger antennas, booms and/or solar panels. One example of a vehicle dominated by its flexible-body dynamics includes a large hoop antenna satellite built by NASA's Langley Research Center, which has 70 significant modes within a bandwidth of 4.1-6.2 Hz [19]. The proposed simulation capabilities have the potential to simulate whether or not the spacecraft appendages might be excited by environmental forces, and could act as a testbed to study a variety of methods that might mitigate this undesired motion.

Furthermore, future robotic servicing missions have the potential of ensuring the success of many current large-scale missions such as the James Webb Space Tele-

scope (shown in Figure 6.5). Since there are many risks involved in the deployment of such a massive structure, it might be necessary to send a robotic servicing vehicle to fix a catastrophic failure, similar to how human servicing enabled the successful deployment of the Hubble Space Telescope.
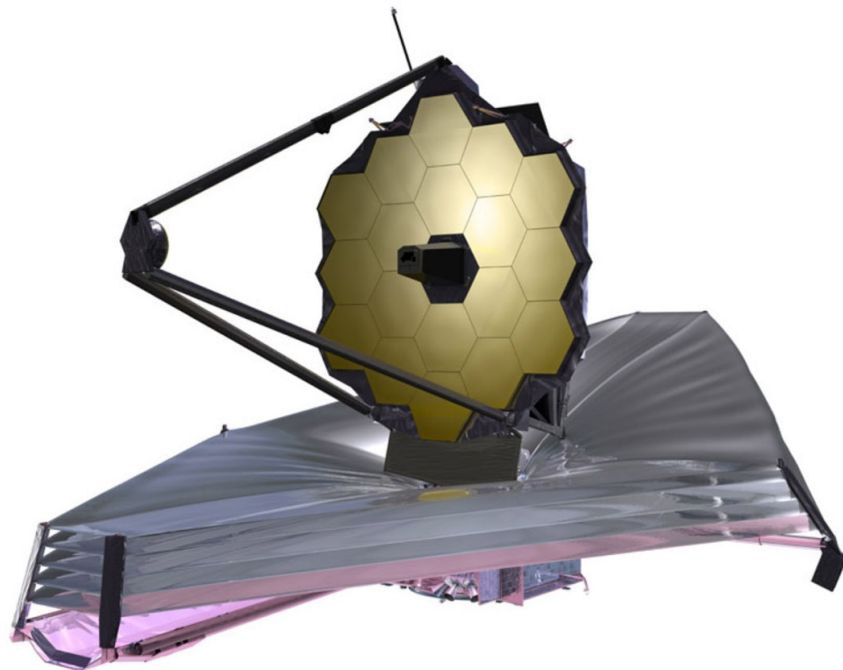
Figure 6.5: James Webb Space Telescope (Courtesy of *www.spie.org*).

Chapter A: Flexible-Body Dynamics: Mass Matrix and Velocity Vector Terms

The following equations represent terms within the flexible-body mass matrix, defined in the body axis [8]:

$$m_{RR} = \int_V \rho_a A A^T dV \tag{A.1}$$

$$\tilde{\bar{S}}_t = \int_V \rho_a \left(\tilde{\bar{u}} \right) dV \tag{A.2}$$

$$\bar{S} = \int_V \rho S dV \tag{A.3}$$

$$\bar{I}_{\theta\theta} = \int_V \rho_a (\tilde{\bar{u}})^T \left(\tilde{\bar{u}} \right) dV \tag{A.4}$$

$$\bar{I}_{\theta f} = \int_V \rho_a \left(\tilde{\bar{u}} \right) S dV \tag{A.5}$$

$$m_{ff} = \int_V \rho_a S^T S dV \tag{A.6}$$

In addition, the following equations represent terms within the flexible-body forcing vector:

$$Q_v^R = -\tilde{\bar{\omega}}\tilde{\bar{\omega}}\bar{S}_t - 2\tilde{\bar{\omega}}\bar{S}\dot{q}_f \tag{A.7}$$

$$Q_v^\theta = -\tilde{\bar{\omega}}\bar{I}_{\theta\theta}\bar{\omega} - \dot{\bar{I}}_{\theta\theta}\bar{\omega} - \tilde{\bar{\omega}}\bar{I}_{\theta f}\dot{q}_f \tag{A.8}$$

$$Q_v^f = -\int_V \rho_a S^T \left(\tilde{\bar{\omega}}^2 \bar{u} + 2\tilde{\bar{\omega}}S\dot{q}_f \right) dV \tag{A.9}$$

Furthermore, the supporting terms for both the mass matrix and forcing vector

are as follows:

$$m_{R\theta} = \int_V \rho_a A \tilde{\bar{u}}^T A^T dV \tag{A.10}$$

$$m_{Rf} = \int_V \rho_a A S dV \tag{A.11}$$

$$m_{\theta\theta} = -\int_V \rho_a A \tilde{\bar{u}} \tilde{\bar{u}} A^T dV \tag{A.12}$$

$$m_{\theta f} = \int_V \rho_a A \tilde{\bar{u}} S dV \tag{A.13}$$

$$\bar{S}_t = \int_V \rho_a \bar{u} dV \tag{A.14}$$

$$\dot{\bar{I}}_{\theta\theta} = \left(2 \int_V \rho \bar{u}_o^T S dV \right) \dot{q}_f + \left(2 \int_V \rho S^T S dV \right) \dot{q}_f q_f \tag{A.15}$$

Once each of these terms is defined, it is possible to express the flexible-body

equations of motion in body frame as:

$$\begin{bmatrix} m_{RR} & \tilde{\bar{S}}_t^T & \bar{S} \\ \tilde{\bar{S}}_t & \bar{I}_{\theta\theta} & \bar{I}_{\theta f} \\ \bar{S}^T & \bar{I}_{\theta f}^T & m_{ff} \end{bmatrix} \begin{bmatrix} \ddot{R} \\ \bar{\alpha} \\ \ddot{q}_f \end{bmatrix} = \begin{bmatrix} Q_v^R \\ Q_v^\theta \\ Q_v^f - k_{ff} q_f - b \dot{q}_f \end{bmatrix} + \begin{bmatrix} \bar{F}_{ext} \\ \bar{T}_{ext} \\ \bar{Q}_{ext} \end{bmatrix} \tag{A.16}$$

Similarly, the flexible-body equations of motion can be expressed in inertial frame

as:

$$\begin{bmatrix} m_{RR} & m_{R\theta} & m_{Rf} \\ m_{R\theta}^T & m_{\theta\theta} & m_{\theta f} \\ m_{Rf}^T & m_{\theta f}^T & m_{ff} \end{bmatrix} \begin{bmatrix} \ddot{R} \\ \alpha \\ \ddot{q}_f \end{bmatrix} = \begin{bmatrix} AQ_v^R \\ AQ_v^\theta \\ Q_v^f - k_{ff} q_f - b \dot{q}_f \end{bmatrix} + \begin{bmatrix} F_{ext} \\ T_{ext} \\ Q_{ext} \end{bmatrix} \tag{A.17}$$

Chapter B: Supporting Analysis

B.1 Development of Models

B.1.1 Euler-Bernouilli Beam Derivation: Mode Shape Constants

It can be shown that the mode shape for a clamped-free beam resembles the description in (4.1), where the constants k_{c_i} and λ_i are given in Table B.1 [17]. A similar table can be produced for free-free boundary conditions, shown in Table B.2 [17]. The mode shape for a free-free beam differs from the cantilever case given by (4.1), and instead is described as:

$$\phi_i = \cosh\left(\frac{\lambda_i x_a}{L_a}\right) + \cos\left(\frac{\lambda_i x_a}{L_a}\right) - k_{c_i}\left(\sinh\left(\frac{\lambda_i x_a}{L_a}\right) + \sin\left(\frac{\lambda_i x_a}{L_a}\right)\right) \qquad (B.1)$$

Table B.1: Mode shape constants describing cantilever Euler-Bernoulli beam.

Mode Number	λ_i	k_{c_i}
1	1.8751	0.7341
2	4.6941	1.0185
3	7.8548	0.9992
4	10.9955	1.0000
5	14.1372	1.0000

Table B.2: Mode shape constants describing free-free Euler-Bernoulli beam.

Mode Number	λ_i	k_{c_i}
1	4.7300	0.9825
2	7.8532	1.0008
3	10.9956	1.0000
4	14.1372	1.0000
5	17.2788	1.0000

B.1.2   FEM Beam Analysis: Sufficient Number of Elements

An analysis was conducted to determine how many elements should be used in the ADAMS^{TM} finite element model used during this research effort [25]. From Tables B.3 and B.4, it is evident that with 80 elements, the finite element model is able to accurately model the first four modes to less than 0.1% of the true known value. It is recommended that a follow-on experiment be conducted to determine the accuracy of this model when more complicated geometries are involved, but this proves that this modeling technique can accurately predict the dominant modal response of the satellite system studied during this research effort.

B.1.3   NASTRAN^{TM}/ADAMS^{TM} Modal Comparison

Now that it has been proven that an 80 element NASTRAN^{TM} model can sufficiently model the appendages specified in this research, a full chart detailing the frequencies of various test cases is outlined in Fig. B.1 [25]. Since the finite element model features a NASTRAN^{TM} model imported into ADAMS^{TM}, it is necessary to show the differences in modal response based on the boundary conditions and

Table B.3: Analysis on sufficient number of elements in NASTRAN^{TM} model (magnitude comparison) [25].

Flex Mode	1	2	3	4	5
Known Freq (Hz) [17]	0.2500	1.5667	4.3869	8.5965	14.2107
20 Element Model	0.2497	1.5604	4.3577	8.5159	14.0377
40 Element Model	0.2499	1.5651	4.3791	8.5746	14.1630
80 Element Model	0.2500	1.5662	4.3845	8.5894	14.1943
120 Element Model	0.2500	1.5665	4.3841	8.5921	14.2002
160 Element Model	0.2500	1.5665	4.3858	8.5931	14.2022

Table B.4: Analysis on sufficient number of elements in NASTRAN^{TM} model (error comparison) [25].

Flex Mode	1	2	3	4	5
Known Freq (Hz) [17]	0.2500	1.5667	4.3869	8.5965	14.2107
20 Element Model	0.115%	0.402%	0.664%	0.937%	1.217%
40 Element Model	0.030%	0.105%	0.177%	0.255%	0.336%
80 Element Model	0.008%	0.031%	0.055%	0.083%	0.115%
120 Element Model	0.004%	0.017%	0.063%	0.051%	0.074%
160 Element Model	0.003%	0.012%	0.024%	0.040%	0.060%

simulation platform.

This data agrees with intuition, that the frequency of an appendage with pure cantilever boundary conditions will differ from a free-free beam with a concentrated mass located at the center. This is how the finite element model interprets the flexible satellite problem, which serves as an independent verification effort to compare directly to the continuous beam model.

Note that the free-free modes used in this finite element analysis can be rep-

Free-Free Modes	Freq (Hz)/Flex Mode	1	2	3	4	5	6	7	8	9	10	11	12	13	14
NASTRAN Single Body Model	Free Free System Modes - All Modes - NASTRAN	0.2752	0.2752	0.8580	0.8580	1.6200	1.6200	1.9927	1.9927	4.4383	4.4383	4.5339	4.5339	8.6441	8.6441
	Fixed CM System Modes - All Modes - NASTRAN	0.2500	0.2500	0.2500	0.2500	1.5662	1.5662	1.5662	1.5662	4.3845	4.3845	4.3845	4.3845	8.5894	8.5894
ADAMS Single Body Model	Free Free System Modes - All Modes - ADAMS	0.2752	0.2752	0.8580	0.8580	1.6200	1.6200	1.9928	1.9928	4.4385	4.4385	4.5341	4.5341	8.6453	8.6453
	Fixed CM System Modes - All Modes - ADAMS	0.2500	0.2500	0.2500	0.2500	1.5662	1.5662	1.5663	1.5663	4.3845	4.3845	4.3849	4.3849	8.5894	8.5894
NASTRAN Half Beam Component Modes	Free Free Component Modes - NASTRAN & MNF	0.8618	0.8618	2.0184	2.0184	4.5838	4.5838	8.7162	8.7162	14.2927	14.2927	21.2806	21.2806	29.6695	29.6695
	Fixed Free Component Modes - NASTRAN	0.2500	0.2500	1.5662	1.5662	4.3845	4.3845	8.5894	8.5894	14.1943	14.1943	21.1964	21.1964	29.5933	29.5933
ADAMS Three Body Model	Free Free System Modes all Modes Enabled ADAMS	0.2752	0.2752	0.8580	0.8580	1.6200	1.6200	1.9927	1.9927	4.4383	4.4383	4.5339	4.5339	8.6443	8.6443
	Fixed System Modes - All Modes - ADAMS	0.2500	0.2500	0.2500	0.2500	1.5662	1.5662	1.5662	1.5662	4.3845	4.3845	4.3845	4.3845	8.5895	8.5895
	Free Free System Modes - App Mode 8 Enabled ADAMS	0.2921	0.8580												
	Free Free System Modes - App Mode 10 Enabled ADAMS	0.7426	1.9926												
	Free Free System Modes - App Mode 8 & 10 Enabled ADAMS	0.2757	0.8580	1.6238	1.9929										
	Fixed Free System Modes - App Mode 8 & 10 Enabled ADAMS	0.2506	0.2506	1.5718	1.5718										

Figure B.1: Comparison of modal response frequencies for various modes, given different boundary conditions [25].

resented by the two cantilever beams used in the continuous beam model. For example, the first free-free symmetric or asymmetric system modes can be produced by observing the first cantilever mode of each appendage, which are symmetric or asymmetric to one another, accordingly. To observe the second order terms, (i.e., the combination of additional modes), it is necessary to enable more modes per appendage. For example, to represent the first four free-free system modes (two symmetric and two asymmetric), two cantilever modes would have to be modeled for each of the two appendages. Further research is necessary to fully determine how this corresponds to more complicated input profiles that feature both a force and torque input.

B.1.4 Equivalent Appendage Parameters

In the development of the simple uniform appendage models used in the software validation effort of this research, it was necessary to define the exact geometry of the assumed cylindrical shape. Although the length and mass of the appendage are given based on the simulation parameters, the radius of the cylindrical appendage must be calculated. Since it is of interest to match a 0.25 Hz first mode frequency of the appendage, (4.3) was used to derive the necessary structural rigidity (EI) for a given appendage.

For a five meter long appendage with 100 kg mass, the calculated value for EI is approximately 2495 (Nm^2), assuming λ_i of the first mode is 1.875 [17]. Assuming that the appendage is made out of steel for this preliminary analysis, the approx-

imated modulus of elasticity is 200 GPa. Thus, the inertia value is approximately 1.25×10^{-8} m^4, which results in a radius of the uniform cylindrical beam of 0.0112 m, according to:

$$I_x = \frac{\pi}{4} r^4 \tag{B.2}$$

B.1.5 System Response Comparison: Infinite Versus Finite Satellite Hub Mass

In order to better understand the discrepancy in the damped response shown in Fig. 4.15, it is necessary to investigate how a non-infinite satellite hub mass affects the system response frequency. Since the damping term is proportional to the effective mass of the system, an intuitive understanding must be shown as to how the effective mass might be calculated. In Fig. B.2, two systems are compared, one resembling a cantilever beam, represented by a mass-spring system attached to a wall, and the other resembling a more realistic boundary condition for a finite satellite hub mass, where both the satellite hub (m_1) and appendage (m_2) move in response to a given input. This is used to prove why (4.4) and (4.5) need to be modified to account for the fact that the satellite appendages do not exhibit a purely cantilever boundary condition, but instead portray a boundary condition somewhere between a cantilever and free-free case.
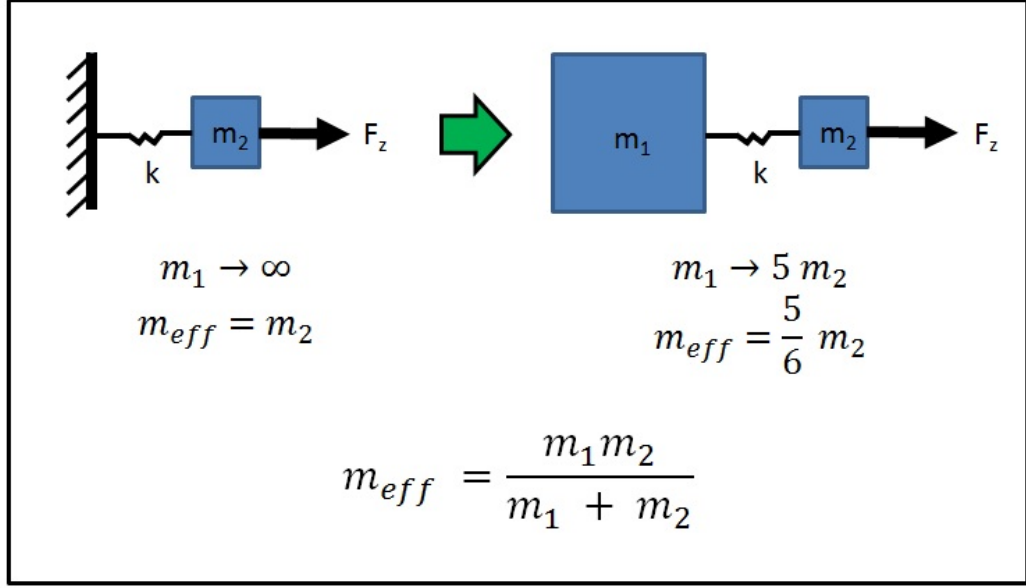
Figure B.2: Example system comparison between infinite and finite satellite hub mass, experiencing a force input.

B.1.6 Dynamic Analysis of Planar Satellite with Two Flexible Appendages

This planar analysis contains the equations of motion for a satellite with symmetric flexible appendages in the ZY plane, as provided by Dr. Craig Carignan [20].

B.1.6.1 Component Equations of Motion

The planar satellite parameters are the mass, m_s, center of mass positions, $\bar{y}$ and $\bar{z}$, and the inertia about the body frame x-axis, I_{xx}. The equations of motion for a rigid body satellite are given by:

$$
\begin{bmatrix} m_s & 0 & -m_s\bar{z} \\ 0 & m_s & m_s\bar{y} \\ -m_s\bar{z} & m_s\bar{y} & I_{xx} \end{bmatrix} \begin{bmatrix} \ddot{y} \\ \ddot{z} \\ \dot{\omega}_x \end{bmatrix} = \begin{bmatrix} -m_s\bar{y}\omega_x^2 \\ -m_s\bar{z}\omega_x^2 \\ 0 \end{bmatrix} + \begin{bmatrix} f_y \\ f_z \\ \tau_x \end{bmatrix} \tag{B.3}
$$

where $\dot{y}$, $\dot{z}$ and ω_x are inertial velocities and f_y, f_z, and τ_x are external forces in the body frame.

The appendage parameters are the mass, m, length, L, the mode shape integrals $\bar{\phi} \equiv \int_0^1 \phi(\xi)d\xi$ and $\bar{\phi}_\xi \equiv \int_0^1 \phi(\xi)\xi d\xi$, where the mode shape is $\phi(\xi)$ and $\xi \equiv y/L$. The planar equations of motion for the appendage on the right side ($y > 0$) are given by:

$$
\begin{bmatrix} m & 0 & -m\bar{\phi}q_{f_r} & 0 \\ 0 & m & \frac{1}{2}mL & m\bar{\phi} \\ -m\bar{\phi}q_{f_r} & \frac{1}{2}mL & m(\frac{1}{3}L^2 + q_{f_r}^2) & mL\bar{\phi}_\xi \\ 0 & m\bar{\phi} & mL\bar{\phi}_\xi & m \end{bmatrix} \begin{bmatrix} \ddot{y} \\ \ddot{z} \\ \dot{\omega}_x \\ \ddot{q}_{f_r} \end{bmatrix} = \begin{bmatrix} \frac{1}{2}mL\omega_x^2 + 2m\bar{\phi}\dot{q}_{f_r}\omega_x \\ m\bar{\phi}q_{f_r}\omega_x^2 \\ -2mq_{f_r}\dot{q}_{f_r}\omega_x \\ mq_{f_r}\omega_x^2 - k_f q_{f_r} - b_f \dot{q}_{f_r} \end{bmatrix} + \begin{bmatrix} 0 \\ 0 \\ 0 \\ Q_{f_r} \end{bmatrix} \tag{B.4}
$$

where q_{f_r} represents modal coordinate for the right appendage. It is assumed that no external forces or torques are applied to the appendages except the generalized modal force, Q_{f_r}.

The planar equations of motion for the appendage on the left side ($y < 0$) are given by:

$$
\begin{bmatrix} m & 0 & -m\bar{\phi}q_{f_\ell} & 0 \\ 0 & m & -\frac{1}{2}mL & m\bar{\phi} \\ -m\bar{\phi}q_{f_\ell} & -\frac{1}{2}mL & m(\frac{1}{3}L^2 + q_{f_\ell}^2) & -mL\bar{\phi}_\xi \\ 0 & m\bar{\phi} & -mL\bar{\phi}_\xi & m \end{bmatrix} \begin{bmatrix} \ddot{y} \\ \ddot{z} \\ \dot{\omega}_x \\ \ddot{q}_{f_\ell} \end{bmatrix} = \begin{bmatrix} -\frac{1}{2}mL\omega_x^2 + 2m\bar{\phi}\dot{q}_{f_\ell}\omega_x \\ m\bar{\phi}q_{f_\ell}\omega_x^2 \\ -2mq_{f_\ell}\dot{q}_{f_\ell}\omega_x \\ -mq_{f_\ell}\omega_x^2 - k_f q_{f_\ell} - b_f \dot{q}_{f_\ell} \end{bmatrix} + \begin{bmatrix} 0 \\ 0 \\ 0 \\ Q_{f_\ell} \end{bmatrix} \tag{B.5}
$$

where q_{f_ℓ} represents modal coordinate for the left appendage.

B.1.6.2   System Equations of Motion

The system equations of motion are obtained by adding the rigid body components of equations (B.3), (B.4), and (B.5) and appending the two modal equations as follows:

$$
\begin{bmatrix}
m_s + 2m & 0 & -m_s\bar{z} - m\bar{\phi}(q_{f_r} + q_{f_\ell}) & 0 & 0 \\
0 & m_s + 2m & m_s\bar{y} & m\bar{\phi} & m\bar{\phi} \\
-m_s\bar{z} - m\bar{\phi}(q_{f_r} + q_{f_\ell}) & m_s\bar{y} & I_{xx} + m(\frac{2}{3}L^2 + q_{f_r}^2 + q_{f_\ell}^2) & mL\bar{\phi}_\xi & -mL\bar{\phi}_\xi \\
0 & m\bar{\phi} & mL\bar{\phi}_\xi & m & 0 \\
0 & m\bar{\phi} & -mL\bar{\phi}_\xi & 0 & m
\end{bmatrix}
\begin{bmatrix}
\ddot{y} \\
\ddot{z} \\
\dot{\omega}_x \\
\ddot{q}_{f_r} \\
\ddot{q}_{f_\ell}
\end{bmatrix}
$$

$$
=
\begin{bmatrix}
-m_s\bar{y}\omega_x^2 + 2m\bar{\phi}(\dot{q}_{f_r} + \dot{q}_{f_\ell})\omega_x \\
-m_s\bar{z}\omega_x^2 + m\bar{\phi}(q_{f_r} + q_{f_\ell})\omega_x^2 \\
-2m(q_{f_r}\dot{q}_{f_r} + q_{f_\ell}\dot{q}_{f_\ell})\omega_x \\
mq_{f_r}\omega_x^2 - k_f q_{f_r} - b_f\dot{q}_{f_r} \\
-mq_{f_\ell}\omega_x^2 - k_f q_{f_\ell} - b_f\dot{q}_{f_\ell}
\end{bmatrix}
+
\begin{bmatrix}
f_y \\
f_z \\
\tau_x \\
Q_{f_r} \\
Q_{f_\ell}
\end{bmatrix}
\tag{B.6}
$$

Writing the equations out in scalar form and assuming $\bar{y} = \bar{z} = 0$ gives the following:

$$
(m_s + 2m)\ddot{y} - m\bar{\phi}(q_{f_r} + q_{f_\ell})\dot{\omega}_x = 2m\bar{\phi}(\dot{q}_{f_r} + \dot{q}_{f_\ell})\omega_x \tag{B.7}
$$

$$
(m_s + 2m)\ddot{z} + m\bar{\phi}(\ddot{q}_{f_r} + \ddot{q}_{f_\ell}) = m\bar{\phi}(q_{f_r} + q_{f_\ell})\omega_x^2 \tag{B.8}
$$

$$\left[I_{xx} + m(\frac{2}{3}L^2 + q_{f_r}^2 + q_{f_\ell}^2)\right]\dot{\omega}_x - m\bar{\phi}(q_{f_r} + q_{f_\ell})\ddot{y} + mL\bar{\phi}_\xi(\ddot{q}_{f_r} - \ddot{q}_{f_\ell})$$

$$= -2m(q_{f_r}\dot{q}_{f_r} + q_{f_\ell}\dot{q}_{f_\ell})\omega_x \qquad \text{(B.9)}$$

$$m\ddot{q}_{f_r} + m\bar{\phi}\ddot{z} + mL\bar{\phi}_\xi\dot{\omega}_x = mq_{f_r}\omega_x^2 - k_f q_{f_r} - b_f \dot{q}_{f_r} \qquad \text{(B.10)}$$

$$m\ddot{q}_{f_\ell} + m\bar{\phi}\ddot{z} - mL\bar{\phi}_\xi\dot{\omega}_x = -mq_{f_\ell}\omega_x^2 - k_f q_{f_\ell} - b_f \dot{q}_{f_\ell} \qquad \text{(B.11)}$$

B.1.6.3 Symmetric Appendage Motion

For symmetric motion, the appendage deflections are equal in magnitude and direction so that $q_{f_r} = q_{f_\ell}$. This produces oscillatory motion in the z-direction, and there should be a steady-state solution for $\omega_x = 0$. Substituting $\omega_x = 0$ into the above equations results in $\ddot{y} = 0$ in (B.7) and $\dot{\omega}_x = 0$ in (B.9) since $\ddot{q}_{f_r} = \ddot{q}_{f_\ell}$. Substituting $\omega_x = 0$ into (B.8) gives the following relation between the modal and z accelerations:

$$\ddot{z} = \frac{-m\bar{\phi}}{m_s + 2m}(\ddot{q}_{f_r} + \ddot{q}_{f_\ell}) \qquad \text{(B.12)}$$

Summing (B.10) and (B.11) gives the following equation

$$m(\ddot{q}_{f_r} + \ddot{q}_{f_\ell}) + 2m\bar{\phi}\ddot{z} = -k_f(q_{f_r} + q_{f_\ell}) - b_f(\dot{q}_{f_r} + \dot{q}_{f_\ell}) \qquad \text{(B.13)}$$

Substituting $\ddot{z}$ from (B.12) into (B.13) and combining modal acceleration terms gives

$$m_{eff}(\ddot{q}_{f_r} + \ddot{q}_{f_\ell}) + b_f(\dot{q}_{f_r} + \dot{q}_{f_\ell}) + k_f(q_{f_r} + q_{f_\ell}) = 0 \qquad \text{(B.14)}$$

where the "effective" mass is given by

$$m_{eff} \equiv \left[1 - \frac{2m}{m_s + 2m} \bar{\phi}^2 \right] m \qquad (B.15)$$

B.1.6.4 Asymmetric Appendage Motion

For asymmetric motion, the appendage deflections are equal in magnitude but opposite in direction so that $q_{f_r} = -q_{f_\ell}$. This should produce oscillatory rotation about the x-axis and no translation. Substituting $q_{f_r} = -q_{f_\ell}$ into (B.7) and (B.8) verifies that $\ddot{y} = 0$ and $\ddot{z} = 0$, and solving (B.9) for $\dot{\omega}_x$ results in

$$\dot{\omega}_x = -\frac{mL\bar{\phi}_\xi}{I_{eff}} (\ddot{q}_{f_r} - \ddot{q}_{f\ell}) - \frac{2m}{I_{eff}} (q_{f_r} \dot{q}_{f_r} + q_{f\ell} \dot{q}_{f\ell}) \omega_x \qquad (B.16)$$

where $I_{eff} \equiv I_{xx} + m(\frac{2}{3}L^2 + q_{f_r}^2 + q_{f\ell}^2)$. Subtracting (B.11) from (B.10) gives

$$m(\ddot{q}_{f_r} - \ddot{q}_{f\ell}) + 2mL\bar{\phi}_\xi \dot{\omega}_x = -k_f(q_{f_r} - q_{f\ell}) - b_f(\dot{q}_{f_r} - \dot{q}_{f\ell}) \qquad (B.17)$$

Substituting $\dot{\omega}_x$ from (B.16) into (B.17) and combining modal acceleration terms yields

$$m_{eff}(\ddot{q}_{f_r} - \ddot{q}_{f\ell}) + b_f(\dot{q}_{f_r} - \dot{q}_{f\ell}) + k_f(q_{f_r} - q_{f\ell}) = \frac{4m^2 L\bar{\phi}_\xi}{I_{eff}} (q_{f_r} \dot{q}_{f_r} + q_{f\ell} \dot{q}_{f\ell}) \omega_x \qquad (B.18)$$

where the "effective" mass is given by

$$m_{eff} \equiv \left[1 - \frac{2mL^2}{I_{eff}} \bar{\phi}_\xi^2 \right] m \qquad (B.19)$$

Note that the effective mass is no longer constant as in symmetric motion because I_{eff} depends upon the modal deflection.

B.2   Hardware Validation Effort

B.2.1   Derivation of Satellite Parameters

For the testing of this HIL simulation, a number of structural parameters of a physical system are derived to resemble realistic satellite parameters. The simplified set of appendages that were constructed is shown in Figure B.3, and were constructed to be mirror images of one another. The stiffness, damping ratio, mass, and geometry of the physical appendage structure are examples of such inputs, and are hereby described.
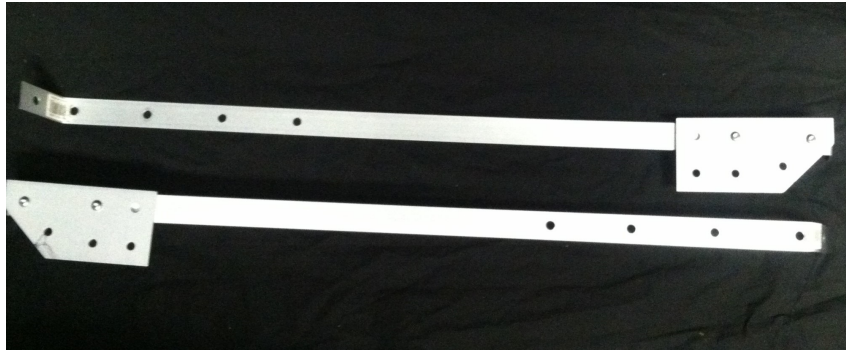
Figure B.3: Physical appendages built for the hardware validation effort.

B.2.1.1   Structural Rigidity

In order to develop a model of the physical appendages contructed during this hardware validation effort, it was necessary to derive the structural rigidity,

which governs its frequency response. The structural rigidity is directly related to the stiffness of the structure and therefore the frequency of its modal response over time. This parameter is characteristic to the structure's geometry and material properties and can be calculated from the product of the appendage's modulus of elasticity and area moment of inertia.

Since the material properties were unknown, however, a loading test was conducted to find a representative value, where the appendages were each clamped to a table and the deflection was measured due to a varied set of weights hung from the end of the beam. Note that the tip masses as seen in Figure B.3 were not attached to the physical appendages during this test effort, since the desired value of structural rigidity is characteristic of the beam itself. A simplified skematic of the test setup is shown in Figure B.4, and the measured geometry of each appendage is given in Table B.5.
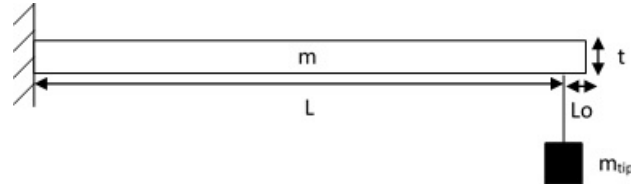
Figure B.4: Load test setup showing mass that will cause tip deflection of beam.

By finding the force of the weight exerted on the beam and the resulting tip deflection (δ_{tip}), it is possible to calculate the structural rigidity (EI) for each value of weight used, via (B.20). The results of this experiment are shown in Figure B.5, and the average calculated value for structural rigidity is documented in Table 5.1.

Table B.5: Measured appendage hardware geometry.

	Appendage 1	Appendage 2
Mass	108 g	108 g
Thickness	0.062 in	0.063 in
Width	1.187 in	1.193 in
Length $(L + L_o)$	9 7/16 in	9 1/2 in
L_o	15/16 in	15/16 in

$$EI = \frac{F_{tipmass}L^3}{3\delta_{tip}} \tag{B.20}$$
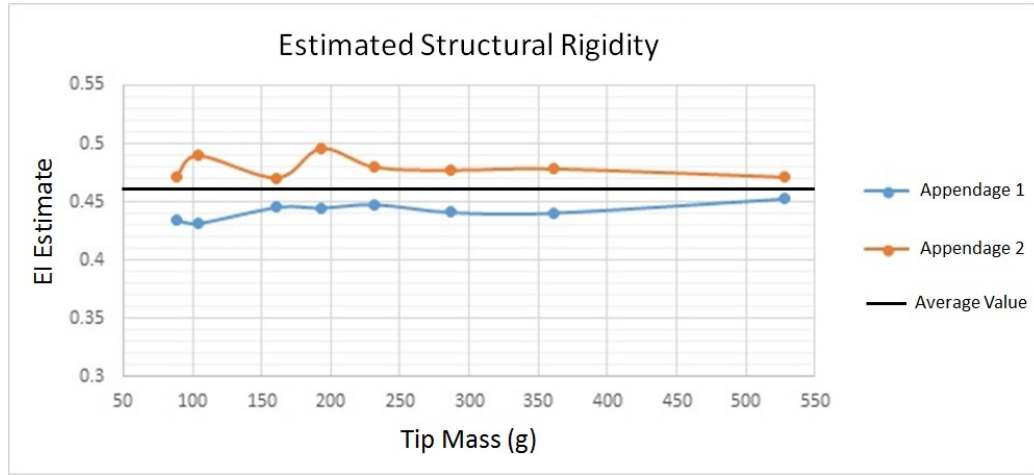
Figure B.5: Load test results showing estimated structural rigidity.

After verifying that the appendage response was within its elastic limit, a first-order error analysis was conducted, which found that less than a one percent error was expected purely due to experimental error. The specific results of this analysis include the margin of error of each data point measured in Figure B.5, such that the expected error from each measured value (purely due to experimental error) is only expected to be off by the quantity dEI. Seperate calculations were produced for the

two appendages, shown in Table B.6, and the parameters used in this analysis are given in Table B.7. The average margin of error of each data point is approximately half of a percent of the calculated value, calculated according to (B.21).

$$\delta\left(EI\right) = \sqrt{\left(\frac{d(EI)}{d\delta}\right)^2 (d\delta)^2 + \left(\frac{d(EI)}{dm}\right)^2 (dm)^2} \qquad \text{(B.21)}$$

Table B.6: Margin of error in calculation of structural rigidity.

Data Point	Appendage 1 dEI (Nm^2)	Appendage 2 dEI (Nm^2)
1	0.00691	0.01060
2	0.00296	0.00303
3	0.00259	0.00283
4	0.00244	0.00265
5	0.00207	0.00235
6	0.00138	0.00146
7	0.00115	0.00128
8	0.00096	0.00103
9	0.00077	0.00083
10	0.00061	0.00066
11	0.00043	0.00045

Table B.7: Parameters used in error analysis of structural rigidity derivation.

$d\delta$ (in)	dm (kg)	g $(\frac{m}{s})^2$	L (m)
$\frac{1}{64}$	0.0005	9.81	0.2167

B.2.1.2 Response Frequency

In order to have the derived satellite model resemble a more realistic spacecraft system, it was desired to have the appendage's first mode exhibit a near 1 Hz

98

frequency. Since the constructed beam itself had a much higher frequency than this desired value, a tip mass was added to the physical structure as seen in Figure B.3. With this tip mass, the overall structure was able to resemble the modal frequency of a realistic solar panel or boom.

Since there is still a desire to model the physical appendages as simple uniform, slender beams, an approximation was made to convert this lumped mass to its effective distributed mass, which can be applied along the beam itself [26]. This additional structure only affects the total mass of each appendage, by adding the term given in (B.22), which is taken into account in the total mass of the modeled beam given in Table 5.1.

$$m_{distributed} = \frac{m_{lumped}}{0.23} \tag{B.22}$$

B.2.1.3   Damping Ratio

In order to simulate the damped response of the given system, it is necessary to determine an accurate value for the damping ratio, characteristic of the physical appendages attached to the Motoman robot (Fig. 5.3). To accomplish this task, an initial test was conducted to observe the pure modal response by exciting the appendages without allowing the satellite hub to translate or rotate. In effect, the inactive robot resembled a fixed boundary condition, and as such, each appendage acted as if it was a simple cantilever beam. By exerting a force impulse on each appendage, it was possible to observe the damped, oscillatory response and classify

the appendage's damping characteristics by using the log-decrement method.

Figure B.6 shows the decay profile as measured during the testing of the physical appendages. By averaging the first twenty peaks, it was possible to estimate the damping ratio from this data, which is provided in Table 5.1. This value represents the damped response profile, which is a function of the material properties of the constructed appendage itself along with the method used to attach the appendages to the robot base.
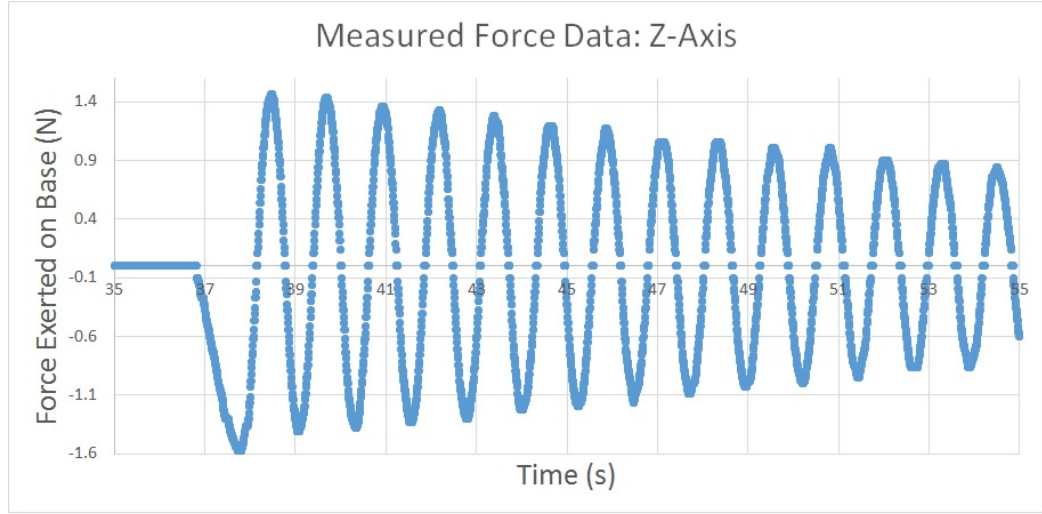
Figure B.6: Measured force response of physical appendages, used to extract damping characteristics.

The measured values that were used to calculate the damping ratio were directly taken from Figure B.6 and are given in Table B.8. By averaging the ζ_i values, a damping ratio of 0.00715 was found to characterize the constructed appendages. Note that the value, x_{peak_i}, is the magnitude of the response at peak number i_{peak}.

Table B.8: Table of values used to derive damping ratio of constructed appendage.

i_{peak}	x_{peak_i}	$\frac{x_{i+1}}{x_i}$	δ_i	ζ_i
1	1.466	1.019	0.019	0.00298
2	1.439	1.060	0.058	0.00927
3	1.358	1.020	0.020	0.00322
4	1.330	1.043	0.042	0.00663
5	1.276	1.068	0.066	0.01049
6	1.195	1.023	0.023	0.00367
7	1.167	1.103	0.098	0.01554
8	1.059	1	0	0
9	1.059	1.054	0.053	0.00838
10	1.005	1	0	0
11	1.005	1.121	0.114	0.01821
12	0.896	1.031	0.031	0.00489
13	0.869	1.032	0.032	0.00506
14	0.842	1.033	0.033	0.00521
15	0.815	1.035	0.034	0.00541
16	0.787	1.074	0.071	0.01137
17	0.733	1.080	0.077	0.01225
18	0.679	1.042	0.041	0.00649
19	0.652	1.044	0.043	0.00679
20	0.624	—	—	—

B.2.2   Motoman SIA-10 Bandwidth Calculation

Although the Motoman SIA-10 robot is simply following the commanded motion as dictated by the satellite simulation, this platform enables a direct comparison between the predicted response to that of an actual, physical system. Since the robot is running a real-time simulation, there are a few limitations including the robot bandwidth itself, which can introduce delay into the system. An example of this is shown in Figure B.7, where the robot follows a trajectory dictated by the satellite dynamics model. In this comparison, a delay is evident of approximately

0.1 seconds. Although this delay is not joint-specific, it provides insight to the magnitude of delay present in the system as depicted in Figure B.8.
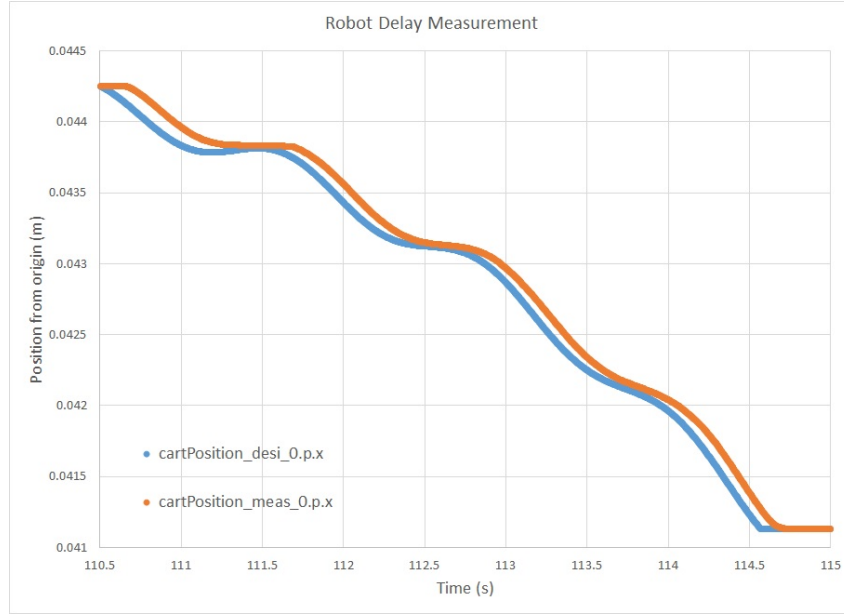
Figure B.7: Comparison between the desired and measured position of the Motoman SIA-10 robot, in the x-direction, for a given test case.
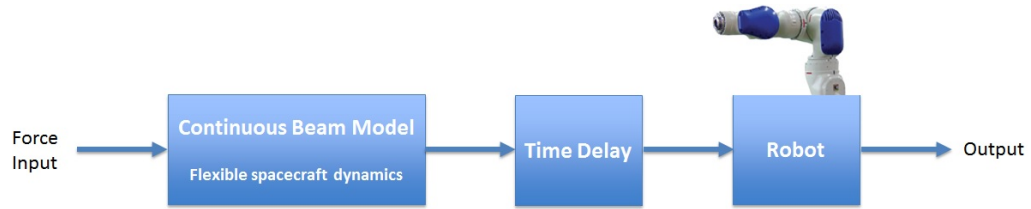
Figure B.8: Location of time delay in flexible-body simulation where Motoman SIA-10 robot follows predicted response.

Chapter C: Coupled Satellite Dynamic Simulation Code

The following are the MATLAB scripts used in the development of the flexible-body dynamic simulations produced during this research. The file satellite6-2DOF.m is the main file, which is run by the user. It is in this file that the parameters for a particular satellite system must be entered, at which point a new ConstantIntegrals-2DOF file must be created that corresponds to this system. The nominal, 500 kg GOES-class satellite parameters (used in the software validation effort in Chapter 4 of this research) are given in the example code shown in the following section, however these are easily changed to describe the physical hardware constructed for the validation efforts presented in Chapter 5 of this research.

C.1   Satellite6 2DOF

```
% File: satellite6_2DOF.m

% Abstract:
%   Calculates and plots the state of a satellite with two appendages vs t

% Support Files:
%{
    Vectorops:
        atan2_zeromod.m         matcross.m          QuatDot.m
```

```
          QuatInv.m                QuatMult.m              QuatNorm.m
          QuatToRot.m              QuatVec.m               RotToRPY.m
     RungeKuttaVeh6_2DOF.m
     inertia_convert.m
     satnewstate6_2DOF.m
     satplot2_2DOF.m
     ConstantIntegrals6_2DOF.m
     ConstantIntegrals6_2DOF_HWTEST.m


****************
NOTE: For the HW test runs, must change satnewstate6_2DOF reference to
use "ConstantIntegrals6_2DOF_HWTEST" instead of "ConstantIntegrals6_2DOF".
Must also change variables below (m,L,EI,ICs,z) to match hardware
****************


%}



%%%%%%%%%%%%%%%%%%%%%%%%%%%%%%%%%%%%%%%%%%%%%%%%%%%%%%%%%%%%%%%%%%%%%%%%%%%%%%%%
% ****************************************************************************
%% NOTE: ONLY CHANGE WHAT IS IN THIS BOX

% State Initialization (Inertial Frame)
    x_veh=[0;0;0];                      % Initial hub position (m)
    qu_veh=[0;0;0;1];                   % Initial rotation: quaternion
    xdot_veh=[0;0;0];                  % Initial hub velocity (m/s)
    w_veh=[0;0;0];                      % Initial angular velocity (rad/s)
    qf_veh=[0;0];                       % Initial modal position: app1 (m)
    qfdot_veh=[0;0];                    % Initial modal velocity: app1(m/s)
    qf_vehn=[0;0];                      % Initial modal position: app2 (m)
    qfdot_vehn=[0;0];                   % Initial modal velocity: app2(m/s)

% Define External Forces
    force_thrust=[0;0;100];        % (N)
    torque_thrust=[0;0;0];         % (Nm)
    modal_thrust=[0;0];
    modal_thrustn=[0;0];
        % Note: All forces are defined in body frame

% Define Damping Parameters
    zeta=0.025;                         % Damping ratio for appendage 1
    zetan=zeta;                         % Damping ratio for appendage 2

% Define Satellite Hub Parameter
    msat=500;                           % Mass of satellite (kg)
```

```matlab
    Lsat=1;                                 % Length of satellite (m)
        % Note: assume hub is a cube shape with side length Lsat

% Define Appendage Parameters
    m_a=100;                                % Mass of appendage (kg)
    L_a=5;                                  % Length of appendage (m)
    EIa=2494.871955;                        % Structural rigidity (Nm^2)
        % Note: assume appendage is uniform, cylinder shape

% Define Time Parameters
    dt=0.01;                                % Timestep for propagation
    N=1000;                                 % Number of steps to perform
    t_end=1;                                % Time when to stop input (s)

% Enter File Name to Save Data
    Filename='SimData_Fz_100_Damp_0p025_dt_p01_N_1000.txt';
% ****************************************************************************
%%%%%%%%%%%%%%%%%%%%%%%%%%%%%%%%%%%%%%%%%%%%%%%%%%%%%%%%%%%%%%%%%%%%%%%%%%%%%%

%% OTHER ASSUMPTIONS
%{

- Appendages are located on positive/negative y-axis and only allowed to
    flex about a single axis (z-axis)
- Assumed mode shape of each appendage is a cantilever beam
- Only the first four system modes (first two in-phase and first two
    out-of-phase modes) are observed during this analysis
- Two appendages are identical in mass, geometry and structural parameters

%}

%% Satellite

% Initialize State
x=[x_veh; qu_veh; xdot_veh; w_veh; qf_veh; qfdot_veh; qf_vehn; qfdot_vehn];
    % State vector
u=[force_thrust; torque_thrust; modal_thrust; modal_thrustn];
    % Control (force) vector

[TOTAL(:,1)]=x;             % Begin saving state for every time step
[FTQ(:,1)]=u;               % Begin saving input for every time step

% Assume appendage 2 is identical to appendage 1 (for given test cases)
m_an=m_a;                   % Mass of appendage 2
L_an=L_a;                   % Length of appendage 2
```

```matlab
EIan=EIa;                          % Structural rigidity of appendage 2

% Satellite
rcmsat=[0;0;0];                    % Satellite center of mass location
Iosat_cm=(1/6)*msat*Lsat^2*eye(3);        % Inertia of satellite hub
Iosat=inertia_convert(Iosat_cm,msat,rcmsat);
    % Converts satellite inertia tensor from CM frame to Body frame

%% Propagate to Next State: Runge Kutta

t=0;
[TIME(:,1)]=t;

% Continuously run through states:
for i=1:N,...
    [x,t,F_base,T_base]=RungeKuttaVeh6_2DOF(x,u,msat,rcmsat,Iosat,...
    L_a,m_a,EIa,L_an,m_an,EIan,dt,t,zeta,zetan);

    % Stop external forces after t_end seconds
    if t>t_end;
        u=[0;0;0;0;0;0;0;0;0;0]; % Ie. F/T only for first second if t_end=1
    end

    % Save state etc. for current time step
        [TOTAL(:,i+1)]=x;
        [FTQ(:,i+1)]=u;
        [TIME(:,i+1)]=t;
        [F_base_TOT(:,i+1)]=F_base;
        [T_base_TOT(:,i+1)]=T_base;

    % Output iteration number and state at each point in simulation
    Iterations_Left = N-i
    if i == 1,
        PREOUTPUT = sprintf('TIME  STATE: x,qu,xdot,w,qf,qfdot,qfn,qfndot');
        disp(PREOUTPUT)
    end
    OUTPUT = sprintf('%i     %d %d %d %d %d %d %d %d %d %d',...
        t,x(1),x(2),x(3),x(4),x(5),x(6),x(7),x(8),x(9),x(10),x(11),...
        x(12),x(13),x(14),x(15),x(16),x(17),x(18),x(19),x(20),x(21));
    disp(OUTPUT)

  if i == N,
      OUTPUT2 = sprintf('Params: %d %d %d %d %d %d',msat,Lsat,...
          Iosat(1,1),m_a,L_a,EIa);
      disp(OUTPUT2)
```

```
    end
end

%% Plot State Over Time and Base F/T

figure
satplot2_2DOF(TOTAL,N+1,dt)

figure
plot(TIME,F_base_TOT)
title 'Force Exerted on Base vs. Time'
xlabel 'Time (s)'
ylabel 'F_b_a_s_e (N)'
legend ('F_x','F_y','F_z')

figure
plot(TIME,T_base_TOT)
title 'Torque Exerted on Base vs. Time'
xlabel 'Time (s)'
ylabel 'T_b_a_s_e (N)'
legend ('T_x','T_y','T_z')
```

C.2   RungeKutta6 2DOF

```
% File: RungeKuttaVeh6_2DOF.m

% Abstract:
%   Calculates the propagation of state, x over time via Runge Kutta method
%   Note: this requires a function to be called, to compute the xdot term
%   multiple times.  This is a more accurate way of computing the x2 term,
%   instead of simply computing "x2=x+xdot*dt"

% Support Files:
%   satnewstate6_2DOF.m

% Notes:
%   This code is embedded in the satellite6_2DOF.m file
%   From Craig Carignan's "satellite.m"
```

```
%% Begin Code

function [x2,t,Qv0,Qvn0,Fba0,Fbb0,Tba0,Tbb0]=RungeKuttaVeh6_2DOF(x,u,...
    msat,rcmsat,Iosat,L_a,m_a,EIa,uo_b,L_an,m_an,EIan,uo_bn,dt,t,...
    zeta,zetan,NUMBER_MODES,DEBUG_J,HW_TEST)

ti = t;                    % Set initial time

[k0,Qv0,Qvn0,Fba0,Fbb0,Tba0,Tbb0]=satnewstate6_2DOF(x,u,ti,msat,...
        rcmsat,Iosat,L_a,m_a,EIa,uo_b,L_an,m_an,EIan,uo_bn,zeta,...
        zetan,NUMBER_MODES,DEBUG_J,HW_TEST);
    ti = t + dt/2.0 ;
for i=1:size(x,1),      xi(i) = x(i) + k0(i)*dt/2.0;    end

    [k1,Qv1,Qvn1,Fba1,Fbb1,Tba1,Tbb1]=satnewstate6_2DOF(xi',u,ti,msat,...
        rcmsat,Iosat,L_a,m_a,EIa,uo_b,L_an,m_an,EIan,uo_bn,zeta,...
        zetan,NUMBER_MODES,DEBUG_J,HW_TEST);
ti = t + dt/2.0 ;
for i=1:size(x,1),  xi(i) = x(i) + k1(i)*dt/2.0;    end

    [k2,Qv2,Qvn2,Fba2,Fbb2,Tba2,Tbb2]=satnewstate6_2DOF(xi',u,ti,msat,...
        rcmsat,Iosat,L_a,m_a,EIa,uo_b,L_an,m_an,EIan,uo_bn,zeta,...
        zetan,NUMBER_MODES,DEBUG_J,HW_TEST);
    ti = t + dt ;
for i=1:size(x,1),     xi(i) = x(i) + k2(i)*dt;        end

    [k3,Qv3,Qvn3,Fba3,Fbb3,Tba3,Tbb3]=satnewstate6_2DOF(xi',u,ti,msat,...
        rcmsat,Iosat,L_a,m_a,EIa,uo_b,L_an,m_an,EIan,uo_bn,zeta,...
        zetan,NUMBER_MODES,DEBUG_J,HW_TEST);

for i=1:size(x,1),     x2(i) = x(i) + ...
            (k0(i)+2.0*k1(i)+2.0*k2(i)+k3(i))*dt/6.0;  end

    % Normalize Vehicle Quaternion
    x2(4:7)=QuatNorm(x2(4:7));

    x2=x2';

    t = t + dt;
```

C.3 Satnewstate6 2DOF

```
% File: satnewstate6_2DOF.m

% Abstract:
%   Calculates the derivative of the satellite's current state, xdot.
%   This is used within the RungeKutta propagation and is repeated over
%   every timestep, calculating the new mass and forcing matrices and then
%   using these to derive the derivative of satellite state.

% Notes:
%   This file is embedded in satellite6_2DOF.m and RungeKuttaVeh6_2DOF.m
%   Currently hardcoded to assume z-axis flexibility
%   It is known that something is incorrect with the implementation of
%     the viscous damping terms
%   It is possible that the base force and torque calculations are not
%     accurate; more time is needed to prove the derivation of these terms

%{
****************
NOTE: For the HW test runs, must change satnewstate6_2DOF reference to
use "ConstantIntegrals6_2DOF_HWTEST" instead of "ConstantIntegrals6_2DOF".
Must also change variables in satellite6_2DOF (m,L,EI,ICs,z)
****************
%}

%% Declare Function
function [xdot,Qv,Qvn,F_base_a,F_base_b,T_base_a,T_base_b]=...
    satnewstate6_2DOF(x,u,ti,msat,rcmsat,Iosat,L_a,m_a,...
    EIa,uo_b,L_an,m_an,EIan,uo_bn,zeta,zetan,NUMBER_MODES,DEBUG_J,HW_TEST)

%% Redefine State Values
x_veh        = x(1:3);
qu_veh       = x(4:7);
xdot_veh     = x(8:10);
w_veh        = x(11:13);
qf_veh       = x(14:15);
qfdot_veh    = x(16:17);
qf_vehn      = x(18:19);
qfdot_vehn   = x(20:21);
```

```
A_bi = QuatToRot(qu_veh);

%% Matrix Calculations: Rigid-body Satellite Hub
qBI = QuatInv(qu_veh);
w_veh_b = QuatVec(qBI,w_veh)';

if msat~=0 && L_a~=0,        % Avoid singularity for ill-conditioned input
    Msat = [msat*eye(3) -msat*matcross(rcmsat) zeros(3,2) zeros(3,2); ...
        msat*matcross(rcmsat) Iosat zeros(3,2) zeros(3,2); ...
        zeros(2,3) zeros(2,3) zeros(2,2) zeros(2,2); ...
        zeros(2,3) zeros(2,3) zeros(2,2), zeros(2,2)];
    Qvsat = [msat*matcross(w_veh_b)*(matcross(w_veh_b)*rcmsat); ...
        matcross(w_veh_b)*Iosat*w_veh_b; 0; 0; 0; 0];
else
    Msat = zeros(8+2,8+2);
    Qvsat = zeros(8+2,1);
end

%% FIRST APPENDAGE

if m_a~=0 && L_a~=0, % Add condition to check that m_app DNE 0

%% Preliminary Calculations: Appendage 1
w_b = w_veh_b;                % angular velocity in body frame
wx_b = matcross(w_b);        % matrix cross product of w_b

%% Mass Matrix Calculation: Appendage 1

if HW_TEST == 0,
[IntUoxT,IntUfxT,IntUox2,IntUoxUfx,IntUfx2,IntUoxS,IntUfxS,IntUo,IntSTS,...
    IntUoxSdqx,IntSdqxUox,IntSdqxSqx,IntSqxSdqx,...
    IntUf,IntS,IntSTUo,IntSTUf,IntSTSdq,IntD2Phi1,IntD2Phi2,...
    IntUoxTn,IntUfxTn,IntUox2n,IntUoxUfxn,IntUfx2n,IntUoxSn,IntUfxSn,...
    IntUon,IntSTSn,IntUoxSdqxn,IntSdqxUoxn,IntSdqxSqxn,IntSqxSdqxn,...
    IntUfn,IntSn,IntSTUon,IntSTUfn,IntSTSdqn,IntD2Phi1n,IntD2Phi2n] = ...
    ConstantIntegrals6_2DOF(qf_veh,qf_vehn,qfdot_veh,qfdot_vehn,...
    NUMBER_MODES,DEBUG_J);
elseif HW_TEST == 1,
[IntUoxT,IntUfxT,IntUox2,IntUoxUfx,IntUfx2,IntUoxS,IntUfxS,IntUo,IntSTS,...
    IntUoxSdqx,IntSdqxUox,IntSdqxSqx,IntSqxSdqx,...
    IntUf,IntS,IntSTUo,IntSTUf,IntSTSdq,IntD2Phi1,IntD2Phi2,...
    IntUoxTn,IntUfxTn,IntUox2n,IntUoxUfxn,IntUfx2n,IntUoxSn,IntUfxSn,...
    IntUon,IntSTSn,IntUoxSdqxn,IntSdqxUoxn,IntSdqxSqxn,IntSqxSdqxn,...
    IntUfn,IntSn,IntSTUon,IntSTUfn,IntSTSdqn,IntD2Phi1n,IntD2Phi2n] = ...
```

```
        ConstantIntegrals6_2DOF_HWTEST(qf_veh,qf_vehn,qfdot_veh,qfdot_vehn,...
        NUMBER_MODES,DEBUG_J);
end


mff  = (m_a/L_a)*IntSTS;
mrr  = (m_a/L_a)*L_a*eye(3);
Stx_b = (m_a/L_a)*(IntUoxT+IntUfxT)';
S_b  = (m_a/L_a)*IntS;
Itt_b = -(m_a/L_a)*(IntUox2+(IntUoxUfx+IntUoxUfx')+IntUfx2);
Itf_b = (m_a/L_a)*(IntUoxS+IntUfxS);

M=[mrr Stx_b' S_b zeros(3,2);...
    Stx_b Itt_b Itf_b zeros(3,2);...
    S_b' Itf_b' mff zeros(2,2);...
    zeros(2,3) zeros(2,3) zeros(2,2) zeros(2,2)];

%% Forcing Matrix Calculation: Appendage 1
St_b = (m_a/L_a)*(IntUo+IntUf);
Itt_bdot = -(m_a/L_a)*(IntUoxSdqx+IntSdqxUox+IntSdqxSqx+IntSqxSdqx);

Qvr = -wx_b*wx_b*St_b-2*wx_b*(S_b*qfdot_veh);
Qvt = -wx_b*(Itt_b*w_b)-Itt_bdot*w_b-wx_b*(Itf_b*qfdot_veh);
Qvf = (m_a/L_a)*...
    [(IntSTS(1,1)*qf_veh(1) + IntSTS(1,2)*qf_veh(2))*...
    (w_b(1)*w_b(1) + w_b(2)*w_b(2)) - IntUoxS(1,1)*w_b(2)*w_b(3);...
     (IntSTS(2,1)*qf_veh(1) + IntSTS(2,2)*qf_veh(2))*...
     (w_b(1)*w_b(1) + w_b(2)*w_b(2)) - IntUoxS(1,2)*w_b(2)*w_b(3)];

% Define kff Term
kff = [IntD2Phi1 0; 0 IntD2Phi2]*EIa;

% Define Damping Term
z1 = zeta;
for i=1:2,
    for j=1:2,
        if abs(mff(i,j))<1e-6,
            wn1(i,j) = 0;
            Dff(i,j) = 0;
        else
            wn1(i,j) = sqrt(kff(i,j)/mff(i,j));
            Dff(i,j) = 2*z1*wn1(i,j)*mff(i,j);
        end
    end
end
damp = Dff;
```

```
% Combine Forcing Terms
Qv = [Qvr;Qvt;Qvf-damp*qfdot_veh-kff*qf_veh;0;0];

%% End Condition
else
    M = zeros(8+2,8+2);
    Qv = zeros(8+2,1);
end

%% SECOND APPENDAGE

if m_an~=0 && L_an~=0, % Add Condition to check that m_an DNE 0

%% Mass Matrix Calculation: Appendage 2

mffn   = (m_an/L_an)*IntSTSn;
mrrn   = (m_an/L_an)*L_an*eye(3);
Stx_bn = (m_an/L_an)*(IntUoxTn+IntUfxTn)';
S_bn   = (m_an/L_a)*IntSn;
Itt_bn = -(m_an/L_an)*(IntUox2n+(IntUoxUfxn+IntUoxUfxn')+IntUfx2n);
Itf_bn = (m_an/L_an)*(IntUoxSn+IntUfxSn);

Mn=[mrrn Stx_bn' zeros(3,2) S_bn;...
    Stx_bn Itt_bn zeros(3,2) Itf_bn;...
    zeros(2,3) zeros(2,3) zeros(2,2) zeros(2,2);...
    S_bn' Itf_bn' zeros(2,2) mffn];

%% Forcing Matrix Calculation: Appendage 2

St_bn = (m_an/L_an)*(IntUon+IntUfn);
Itt_bdotn = -(m_an/L_an)*(IntUoxSdqxn+IntSdqxUoxn+IntSdqxSqxn+IntSqxSdqxn);

Qvrn = -wx_b*wx_b*St_bn-2*wx_b*(S_bn*qfdot_vehn);
Qvtn = -wx_b*(Itt_bn*w_b)-Itt_bdotn*w_b-wx_b*(Itf_bn*qfdot_vehn);
Qvfn = (m_an/L_an)*...
    [(IntSTSn(1,1)*qf_vehn(1) + IntSTSn(1,2)*qf_vehn(2))*...
    (w_b(1)*w_b(1) + w_b(2)*w_b(2)) - IntUoxSn(1,1)*w_b(2)*w_b(3);...
     (IntSTSn(2,1)*qf_vehn(1) + IntSTSn(2,2)*qf_vehn(2))*...
     (w_b(1)*w_b(1) + w_b(2)*w_b(2)) - IntUoxSn(1,2)*w_b(2)*w_b(3)];

% Define kff Term
kffn = [IntD2Phi1n 0; 0 IntD2Phi2n]*EIan;

% Define Damping Term
```

```
z2 = zetan;

for i=1:2,
    for j=1:2,
        if abs(mffn(i,j))<1e-6,
            wn2(i,j) = 0;
            Dffn(i,j) = 0;
        else
            wn2(i,j) = sqrt(kffn(i,j)/mffn(i,j));
            Dffn(i,j) = 2*z2*wn2(i,j)*mffn(i,j);
        end
    end
end
dampn = Dffn;

% Combine Forcing Terms
Qvn = [Qvrn;Qvtn;0;0;Qvfn-dampn*qfdot_vehn-kffn*qf_vehn];

%% End Condition
else
    Mn = zeros(8+2,8+2);
    Qvn = zeros(8+2,1);
end

%% Calculate Acceleration Terms
vecTDOF_Flex    = u-Qvsat+Qv+Qvn;
accel           = pinv(Msat+M+Mn)*(vecTDOF_Flex);
xdotdot_veh_b   = accel(1:3);
wdot_veh_b      = accel(4:6);
qfdotdot_veh_b  = accel(7:8);
qfdotdot_veh_bn = accel(9:10);

%% Convert Acceleration to Inertial Coordinates
xdotdot_veh     = QuatVec(qu_veh,xdotdot_veh_b)';   % outputs 3x1 vector
wdot_veh        = QuatVec(qu_veh,wdot_veh_b)';      % outputs 3x1 vector
qudot_veh       = QuatDot(qu_veh,w_veh_b)';         % outputs 4x1 vector
qfdotdot_veh    = qfdotdot_veh_b;                   % outputs 2x1 vector
qfdotdot_vehn   = qfdotdot_veh_bn;                  % outputs 2x1 vector

%% Find Forces on Base (from 1st appendage only)
F_base_a = mrr*xdotdot_veh_b ;
F_base_b = Qvr-Stx_b'*wdot_veh-S_b*qfdotdot_veh;
T_base_a = Itt_b*wdot_veh_b+wx_b*(Itt_b*w_b) ;
T_base_b = (Qvt+wx_b*(Itt_b*w_b))-Stx_b*xdotdot_veh_b-Itf_b*qfdotdot_veh_b;
```

```
%% Assign the Derivative of the State Vector
xdot = [xdot_veh;qudot_veh;xdotdot_veh;wdot_veh;qfdot_veh;...
    qfdotdot_veh;qfdot_vehn;qfdotdot_vehn];
```

C.4   ConstantIntegrals 2DOF

```
% File: ConstantIntegrals6_2DOF.m

% Abstract: Explicitly declare constant integrals for the case of two mode
% shapes, which are found using the Mathematica script given in Appendix D.

% INPUTS: qf1, qf2, dq1, dq2
% ASSUMES: L_a = L_an = 5 <m>, appendages are on y-axis and flex about z,
%   considers first and second modes of each appendage
% NOTE: it is known that something is incorrect in the way that this code
%   changes if you only want to observe a single mode

function ...
[IntUoxT,IntUfxT,IntUox2,IntUoxUfx,IntUfx2,IntUoxS,IntUfxS,IntUo,IntSTS,...
    IntUoxSdqx,IntSdqxUox,IntSdqxSqx,IntSqxSdqx,...
    IntUf,IntS,IntSTUo,IntSTUf,IntSTSdq,IntD2Phi1,IntD2Phi2,...
    IntUoxTn,IntUfxTn,IntUox2n,IntUoxUfxn,IntUfx2n,IntUoxSn,IntUfxSn,...
    IntUon,IntSTSn,IntUoxSdqxn,IntSdqxUoxn,IntSdqxSqxn,IntSqxSdqxn,...
    IntUfn,IntSn,IntSTUon,IntSTUfn,IntSTSdqn,IntD2Phi1n,IntD2Phi2n] = ...
    ConstantIntegrals6_2DOF(qf_veh,qf_vehn,qfdot_veh,qfdot_vehn,...
    NUMBER_MODES)

% ************************************************************
% INCLUDE CHANGES IF ONLY WANT TO OBSERVE A SINGLE MODE (part I of II)
if NUMBER_MODES==1,
    qf_veh(2) = 0;    qfdot_veh(2) = 0;
    qf_vehn(2) = 0;   qfdot_vehn(2) = 0;
elseif NUMBER_MODES==2,
    qf_veh(1) = 0;    qfdot_veh(1) = 0;
    qf_vehn(1) = 0;   qfdot_vehn(1) = 0;
end
% ************************************************************

%% Define 2DOF Constant Integrals (Body Frame)
```

114

```
% Appendage 1:
IntUoxT = [0 0 -12.5; 0 0 0; 12.5 0 0];
IntUfxT = [0 (3.914958784*qf_veh(1)+2.169679470*qf_veh(2)) 0; ...
    -(3.914958784*qf_veh(1)+2.169679470*qf_veh(2)) 0 0; 0 0 0];
IntUox2 = [-125/3 0 0; 0 0 0; 0 0 -125/3];
IntUoxUfx = [0 0 0; 0 0 0; 0 (14.22064360*qf_veh(1)+...
    2.269169651*qf_veh(2)) 0];
IntUfx2 = [(-5.000000008*qf_veh(1)^2+1.372622286e-8*qf_veh(1)*...
    qf_veh(2)-5.000000005*qf_veh(2)^2) 0 0;...
    0 (-5.000000008*qf_veh(1)^2+1.372622286e-8*qf_veh(1)*qf_veh(2)...
    -5.000000005*qf_veh(2)^2) 0; 0 0 0];
IntUoxS = [14.22064360 2.269169651; 0 0; 0 0];
IntUfxS = zeros(3,2);
IntUo = [0; 12.5; 0];
IntSTS = [5.000000008 -6.863043535e-9; -6.863043535e-9 5.000000005];
IntUoxSdqx = [0 0 0; 0 0 0; 0 (14.22064360*qfdot_veh(1)+...
    2.269169651*qfdot_veh(2)) 0];
IntSdqxUox = [0 0 0; 0 0 (14.22064360*qfdot_veh(1)+2.269169651*...
    qfdot_veh(2)); 0 0 0];
IntSdqxSqx = [(-5.000000008*qfdot_veh(1)*qf_veh(1)+...
    6.86311143e-9*(qfdot_veh(2)*qf_veh(1)+qfdot_veh(1)*qf_veh(2))-...
    5.000000005*qfdot_veh(2)*qf_veh(2)) 0 0;...
    0 (-5.000000008*qfdot_veh(1)*qf_veh(1)+6.86311143e-9*...
    (qfdot_veh(2)*qf_veh(1)+qfdot_veh(1)*qf_veh(2))-...
    5.000000005*qfdot_veh(2)*qf_veh(2)) 0; 0 0 0];
IntSqxSdqx = IntSdqxSqx;
IntUf = [0; 0; (3.914958784*qf_veh(1)+2.169679470*qf_veh(2))];
IntS = [0 0; 0 0; 3.914958784 2.169679470];
IntSTUo = [0;0];
IntSTUf = [5.000000008*qf_veh(1) - 6.86301080e-9*qf_veh(2); ...
    -6.862992642e-9*qf_veh(1) + 5.000000005*qf_veh(2)];
IntSTSdq = [5.000000008*qfdot_veh(1) - 6.86301080e-9*qfdot_veh(2); ...
    -6.862992642e-9*qfdot_veh(1) + 5.000000005*qfdot_veh(2)];
IntD2Phi1 = 0.098899;
IntD2Phi2 = 3.8841505;

% Appendage 2:
IntUoxTn = -IntUoxT;
IntUfxTn = [0 (3.914958784*qf_vehn(1)+2.169679470*qf_vehn(2)) 0; ...
    -(3.914958784*qf_vehn(1)+2.169679470*qf_vehn(2)) 0 0; 0 0 0];
IntUox2n = IntUox2;
IntUoxUfxn = -[0 0 0; 0 0 0; 0 (14.22064360*qf_vehn(1)+...
    2.269169651*qf_vehn(2)) 0];
IntUfx2n = [(-5.000000008*qf_vehn(1)^2+1.372622286e-8*qf_vehn(1)*...
```

```
    qf_vehn(2)-5.000000005*qf_vehn(2)^2) 0 0;...
    0 (-5.000000008*qf_vehn(1)^2+1.372622286e-8*qf_vehn(1)*qf_vehn(2)-...
    5.000000005*qf_vehn(2)^2) 0; 0 0 0];
IntUoxSn = -IntUoxS;
IntUfxSn = IntUfxS;
IntUon = -IntUo;
IntSTSn = IntSTS;
IntUoxSdqxn = -[0 0 0; 0 0 0; 0 (14.22064360*qfdot_vehn(1)+...
    2.269169651*qfdot_vehn(2)) 0];
IntSdqxUoxn = -[0 0 0; 0 0 (14.22064360*qfdot_vehn(1)+...
    2.269169651*qfdot_vehn(2)); 0 0 0];
IntSdqxSqxn = [(-5.000000008*qfdot_vehn(1)*qf_vehn(1)+...
    6.86311143e-9*(qfdot_vehn(2)*qf_vehn(1)+qfdot_vehn(1)*qf_vehn(2))-...
    5.000000005*qfdot_vehn(2)*qf_vehn(2)) 0 0;...
    0 (-5.000000008*qfdot_vehn(1)*qf_vehn(1)+6.86311143e-9*...
    (qfdot_vehn(2)*qf_vehn(1)+qfdot_vehn(1)*qf_vehn(2))-...
    5.000000005*qfdot_vehn(2)*qf_vehn(2)) 0; 0 0 0];
IntSqxSdqxn = IntSdqxSqxn;
IntUfn = [0;0;(3.914958784*qf_vehn(1)+2.169679470*qf_vehn(2))];
IntSn = IntS;
IntSTUon = IntSTUo;
IntSTUfn = [5.000000008*qf_vehn(1) - 6.86301080e-9*qf_vehn(2); ...
    -6.862992642e-9*qf_vehn(1) + 5.000000005*qf_vehn(2)];
IntSTSdqn = [5.000000008*qfdot_vehn(1) - 6.86301080e-9*qfdot_vehn(2); ...
    -6.862992642e-9*qfdot_vehn(1) + 5.000000005*qfdot_vehn(2)];
IntD2Phi1n = IntD2Phi1;
IntD2Phi2n = IntD2Phi2;

% **********************************************************
% INCLUDE CHANGES IF ONLY WANT TO OBSERVE A SINGLE MODE (part II of II)
if NUMBER_MODES==1,
    IntUoxS = [14.22064360 0; 0 0; 0 0];
    IntSTS = [5.000000008 0; 0 0];
    IntS = [0 0; 0 0; 3.914958784 0];
    IntD2Phi2 = 0;
    IntSTUf = [5.000000008*qf_veh(1); -6.862992642e-9*qf_veh(1)];
    IntSTSdq = [5.000000008*qfdot_veh(1); -6.862992642e-9*qfdot_veh(1)];
    IntUoxSn = -IntUoxS;
    IntSTSn = IntSTS;
    IntSn = IntS;
    IntD2Phi2n = IntD2Phi2;
    IntSTUfn = [5.000000008*qf_vehn(1); -6.862992642e-9*qf_vehn(1)];
    IntSTSdqn = [5.000000008*qfdot_vehn(1); -6.862992642e-9*qfdot_vehn(1)];

elseif NUMBER_MODES==2,
```

116

```
        IntUoxS = [0 2.26917269169651; 0 0; 0 0];
        IntSTS = [0 0; 0 5.000000005];
        IntS = [0 0; 0 0; 0 2.169679470];
        IntD2Phi1 = 0;
        IntSTUf = [-6.86301080e-9*qf_veh(2); 5.000000005*qf_veh(2)];
        IntSTSdq = [-6.86301080e-9*qf_veh(2); 5.000000005*qfdot_veh(2)];
        IntUoxSn = -IntUoxS;
        IntSTSn = IntSTS;
        IntSn = IntS;
        IntD2Phi2n = IntD2Phi2;
        IntSTUfn = [-6.86301080e-9*qf_vehn(2); 5.000000005*qf_vehn(2)];
        IntSTSdqn = [-6.86301080e-9*qf_vehn(2); 5.000000005*qfdot_vehn(2)];
end
% ****************************************************************
```

C.5   ConstantIntegrals 2DOF HWTEST

```
% File: ConstantIntegrals6_2DOF_HWTEST.m

% Abstract: Explicitly declare constant integrals for the case of two mode
% shapes, which are found using the Mathematica script given in Appendix D.
% This set of integrals describes the constructed appendages used in the
% hardware validation effort, explained in Chapter 5.

% INPUTS: qf1, qf2, dq1, dq2
% ASSUMES: L_a = L_an = 5 <m>, appendages are on y-axis and flex about z,
%   considers first and second modes of each appendage
% NOTE: it is known that something is incorrect in the way that this code
%   changes if you only want to observe a single mode

function ...
[IntUoxT,IntUfxT,IntUox2,IntUoxUfx,IntUfx2,IntUoxS,IntUfxS,IntUo,IntSTS,...
    IntUoxSdqx,IntSdqxUox,IntSdqxSqx,IntSqxSdqx,...
    IntUf,IntS,IntSTUo,IntSTUf,IntSTSdq,IntD2Phi1,IntD2Phi2,...
    IntUoxTn,IntUfxTn,IntUox2n,IntUoxUfxn,IntUfx2n,IntUoxSn,IntUfxSn,...
    IntUon,IntSTSn,IntUoxSdqxn,IntSdqxUoxn,IntSdqxSqxn,IntSqxSdqxn,...
    IntUfn,IntSn,IntSTUon,IntSTUfn,IntSTSdqn,IntD2Phi1n,IntD2Phi2n] = ...
    ConstantIntegrals6_2DOF_HWTEST(qf_veh,qf_vehn,qfdot_veh,qfdot_vehn,...
    NUMBER_MODES)
```

117

```matlab
% ***********************************************************
% INCLUDE CHANGES IF ONLY WANT TO OBSERVE THE FIRST MODE (part I of II)
if NUMBER_MODES==1,
    qf_veh(2) = 0;
    qfdot_veh(2) = 0;
    qf_vehn(2) = 0;
    qfdot_vehn(2) = 0;
elseif NUMBER_MODES==2,
    qf_veh(1) = 0;
    qfdot_veh(1) = 0;
    qf_vehn(1) = 0;
    qfdot_vehn(1) = 0;
end
% ***********************************************************

%% Define 2DOF Constant Integrals (Body Frame)

% Appendage 1:
IntUoxT = [0 0 -0.201612; 0 0 0; 0.201612 0 0];
IntUfxT = [0 (0.4972*qf_veh(1)+0.275549*qf_veh(2)) 0; ...
    -(0.4972*qf_veh(1)+0.275549*qf_veh(2)) 0 0; 0 0 0];
IntUox2 = [-0.0853493 0 0; 0 0 0; 0 0 -0.0853493];
IntUoxUfx = [0 0 0; 0 0 0; 0 (0.229365*qf_veh(1)+0.0365994*qf_veh(2)) 0];
IntUfx2 = [(-0.635*qf_veh(1)^2+1.74323e-9*qf_veh(1)*qf_veh(2)-...
    0.635*qf_veh(2)^2) 0 0;...
    0 (-0.635*qf_veh(1)^2+1.74323e-9*qf_veh(1)*qf_veh(2)-...
    0.635*qf_veh(2)^2) 0; 0 0 0];
IntUoxS = [0.229365 0.0365994; 0 0; 0 0];
IntUfxS = zeros(3,2);
IntUo = [0; 0.201612; 0];
IntSTS = [0.635 -8.71606e-10; -8.71606e-10 0.635];
IntUoxSdqx = [0 0 0; 0 0 0; 0 (0.229365*qfdot_veh(1)+...
    0.0365994*qfdot_veh(2)) 0];
IntSdqxUox = [0 0 0; 0 0 (0.229365*qfdot_veh(1)+0.0365994*...
    qfdot_veh(2)); 0 0 0];
IntSdqxSqx = [(-0.635*qfdot_veh(1)*qf_veh(1)+8.71616e-10*(qfdot_veh(2)*...
    qf_veh(1)+qfdot_veh(1)*qf_veh(2))-0.635*qfdot_veh(2)*qf_veh(2)) 0 0;...
    0 (-0.635*qfdot_veh(1)*qf_veh(1)+8.71616e-10*(qfdot_veh(2)*...
    qf_veh(1)+qfdot_veh(1)*qf_veh(2))-0.635*qfdot_veh(2)*qf_veh(2)) 0;...
    0 0 0];
IntSqxSdqx = IntSdqxSqx;
IntUf = [0; 0; (0.4972*qf_veh(1)+0.275549*qf_veh(2))];
IntS = [0 0; 0 0; 0.4972 0.275549];
IntSTUo = [0;0];
```

```
IntSTUf = [0.635*qf_veh(1) - 8.71604e-10*qf_veh(2); -8.71604e-10*...
    qf_veh(1) + 0.635*qf_veh(2)];
IntSTSdq = [0.635*qfdot_veh(1) - 8.71604e-10*qfdot_veh(2); ...
    -8.71604e-10*qfdot_veh(1) + 0.635*qfdot_veh(2)];
IntD2Phi1 = 48.2815;
IntD2Phi2 = 1.8962e+003;


% Appendage 2:
IntUoxTn = -IntUoxT;
IntUfxTn = [0 (0.4972*qf_vehn(1)+0.275549*qf_vehn(2)) 0; -(0.4972*...
    qf_vehn(1)+0.275549*qf_vehn(2)) 0 0; 0 0 0];
IntUox2n = IntUox2;
IntUoxUfxn = -[0 0 0; 0 0 0; 0 (0.229365*qf_vehn(1)+...
    0.0365994*qf_vehn(2)) 0];
IntUfx2n = [(-0.635*qf_vehn(1)^2+1.74323e-9*qf_vehn(1)*qf_vehn(2)-...
    0.635*qf_vehn(2)^2) 0 0;...
    0 (-0.635*qf_vehn(1)^2+1.74323e-9*qf_vehn(1)*qf_vehn(2)-...
    0.635*qf_vehn(2)^2) 0; 0 0 0];
IntUoxSn = -IntUoxS;
IntUfxSn = IntUfxS;
IntUon = -IntUo;
IntSTSn = IntSTS;
IntUoxSdqxn = -[0 0 0; 0 0 0; 0 (0.229365*qfdot_vehn(1)+...
    0.0365994*qfdot_vehn(2)) 0];
IntSdqxUoxn = -[0 0 0; 0 0 (0.229365*qfdot_vehn(1)+0.0365994*...
    qfdot_vehn(2)); 0 0 0];
IntSdqxSqxn = [(-0.635*qfdot_vehn(1)*qf_vehn(1)+8.71616e-10*...
    (qfdot_vehn(2)*qf_vehn(1)+qfdot_vehn(1)*qf_vehn(2))-0.635*...
    qfdot_vehn(2)*qf_vehn(2)) 0 0;...
    0 (-0.635*qfdot_vehn(1)*qf_vehn(1)+8.71616e-10*(qfdot_vehn(2)*...
    qf_vehn(1)+qfdot_vehn(1)*qf_vehn(2))-0.635*qfdot_vehn(2)*...
    qf_vehn(2)) 0; 0 0 0];
IntSqxSdqxn = IntSdqxSqxn;
IntUfn = [0; 0; (0.4972*qf_vehn(1)+0.275549*qf_vehn(2))];
IntSn = IntS;
IntSTUon = IntSTUo;
IntSTUfn = [0.635*qf_vehn(1) - 8.71604e-10*qf_vehn(2); -8.71604e-10*...
    qf_vehn(1) + 0.635*qf_vehn(2)];
IntSTSdqn = [0.635*qfdot_vehn(1) - 8.71604e-10*qfdot_vehn(2); ...
    -8.71604e-10*qfdot_vehn(1) + 0.635*qfdot_vehn(2)];
IntD2Phi1n = IntD2Phi1;
IntD2Phi2n = IntD2Phi2;
```

```
% ***********************************************************
% INCLUDE CHANGES IF ONLY WANT TO OBSERVE THE FIRST MODE (part II of II)
if NUMBER_MODES==1,
    IntUoxS = [0.229365 0; 0 0; 0 0];
    IntSTS = [0.635 0; 0 0];
    IntS = [0 0; 0 0; 0.4972 0];
    IntD2Phi2 = 0;
    IntSTUf = [0.635*qf_veh(1); -8.71604e-10*qf_veh(1)];
    IntSTSdq = [0.635*qfdot_veh(1); -8.71604e-10*qfdot_veh(1)];
    IntUoxSn = -IntUoxS;
    IntSTSn = IntSTS;
    IntSn = IntS;
    IntD2Phi2n = IntD2Phi2;
    IntSTUfn = [0.635*qf_vehn(1); -8.71604e-10*qf_vehn(1)];
    IntSTSdqn = [0.635*qfdot_vehn(1); -8.71604e-10*qfdot_vehn(1)];

elseif NUMBER_MODES==2,
    IntUoxS = [0 0.0365994; 0 0; 0 0];
    IntSTS = [0 0; 0 0.635];
    IntS = [0 0; 0 0; 0 0.275549];
    IntD2Phi1 = 0;
    IntSTUf = [-8.71604e-10*qf_veh(2); 0.635*qf_veh(2)];
    IntSTSdq = [-8.71604e-10*qf_veh(2); 0.635*qfdot_veh(2)];
    IntUoxSn = -IntUoxS;
    IntSTSn = IntSTS;
    IntSn = IntS;
    IntD2Phi2n = IntD2Phi2;
    IntSTUfn = [-8.71604e-10*qf_vehn(2); 0.635*qf_vehn(2)];
    IntSTSdqn = [-8.71604e-10*qfdot_vehn(2); 0.635*qfdot_vehn(2)];
end
% ***********************************************************
```

C.6   Supporting Math Files

```
% Justin Brannan
% University of Maryland, 2014

% File: Supporting_Math_Files.m

% Abstract:
% The following mathematical operations were used to support the
% satellite6_2DOF.m script, which calculates and plots the state of a
```

```
% satellite over time (9 functions total)


function rc=atan2_zeromod(y,x)
% Abstract: Provides a safer version of atan2
% Returns: if x==0.0 and y==0.0 then 0.0, otherwise atan2(y,x)
% Created by: Stephen Roderick

if(x == 0.0 && y == 0.0)
rc = 0.0;
    else
rc = atan2(y, x);
    end
end



function [xmatcross] = matcross(x)
    % Abstract: Computes the matrix cross product form of a vector
    % Created by: Justin Brannan

    xmatcross=[0 -x(3) x(2); x(3) 0 -x(1); -x(2) x(1) 0];
end



function [qdot]=QuatDot(q,w)
    % Abstract: This program computes the time derivative of the quaternion
    % INPUT: q[4]: the quaternion, w[3]: the angular velocity
    % OUTPUT: qdot[4]: dq/dt
    % Created by: Craig Carignan

qdot(1) = (w(1)*q(4)-w(3)*q(2)+w(2)*q(3))/2.0 ;
qdot(2) = (w(2)*q(4)+w(3)*q(1)-w(1)*q(3))/2.0 ;
qdot(3) = (w(3)*q(4)-w(2)*q(1)+w(1)*q(2))/2.0 ;
qdot(4) = -(w(1)*q(1)+w(2)*q(2)+w(3)*q(3))/2.0 ;
end



function [qinv]=QuatInv(q)
    % Abstract: This program computes the quaternion inverse
    % INPUT: q(4) - quaternion
    % OUTPUT: qinv(4) - inverse quaternion
    % Created by: Craig Carignan

qinv(1) = -q(1) ;
qinv(2) = -q(2) ;
```

```
qinv(3) = -q(3) ;
qinv(4) = q(4) ;
end



function [q]=QuatMult(q1,q2)
    % Abstract: This program computes the product of two quaternions
    % INPUT: q1(4): quaternion 1, q2(4): quaternion 2
    % OUTPUT: q = q1 q2
    % Created by: Craig Carignan

    q(1) = q1(4)*q2(1) + q1(1)*q2(4) + q1(2)*q2(3) - q1(3)*q2(2) ;
q(2) = q1(4)*q2(2) - q1(1)*q2(3) + q1(2)*q2(4) + q1(3)*q2(1) ;
q(3) = q1(4)*q2(3) + q1(1)*q2(2) - q1(2)*q2(1) + q1(3)*q2(4) ;
q(4) = q1(4)*q2(4) - q1(1)*q2(1) - q1(2)*q2(2) - q1(3)*q2(3) ;
end



function [qnorm]=QuatNorm(q)
    % Abstract: This program normalizes a quaternion
    % INPUT: q[4] - quaternion
    % OUTPUT: qnorm[4] - normalized quaternion
    % Created by: Craig Carignan

qmag = 0.0 ;
    for i=1:4, qmag = qmag + q(i)*q(i) ; end
    qmag = sqrt(qmag) ;
for j=1:4, qnorm(j) = q(j)/qmag ; end
end



function R=QuatToRot(q)
    % Abstract: Converts a quaternion into a rotation matrix
    % Created by: Craig Carignan

q1 = q(1);
q2 = q(2);
q3 = q(3);
q4 = q(4);
R(1,1) = q1 * q1 - q2 * q2 - q3 * q3 + q4 * q4;
R(1,2) = 2.0 * (q1 * q2 - q3 * q4);
R(1,3) = 2.0 * (q1 * q3 + q2 * q4);
R(2,1) = 2.0 * (q1 * q2 + q3 * q4);
R(2,2) = -q1 * q1 + q2 * q2 - q3 * q3 + q4 * q4;
R(2,3) = 2.0 * (q2 * q3 - q1 * q4);
```

```
R(3,1) = 2.0 * (q1 * q3 - q2 * q4);
R(3,2) = 2.0 * (q2 * q3 + q1 * q4);
R(3,3) = -q1 * q1 - q2 * q2 + q3 * q3 + q4 * q4;
end


function [qx]=QuatVec(q,x)
    % Abstract: This program multiplies a vector by a quaternion
    % INPUT: q(4): quaternion, x(3): vector
    % OUTPUT: qx(3): quaternion x vector
    % Created by: Craig Carignan

    qx(1) = x(1) * ( q(4)*q(4) + q(1)*q(1) - q(2)*q(2) - q(3)*q(3) )...
            + 2.0 * q(4) * ( x(3)*q(2) - x(2)*q(3) )...
            + 2.0 * q(1) * ( x(2)*q(2) + x(3)*q(3) ) ;
    qx(2) = x(2) * ( q(4)*q(4) - q(1)*q(1) + q(2)*q(2) - q(3)*q(3) )...
            + 2.0 * q(4) * ( x(1)*q(3) - x(3)*q(1) )...
+ 2.0 * q(2) * ( x(3)*q(3) + x(1)*q(1) ) ;
    qx(3) = x(3) * ( q(4)*q(4) - q(1)*q(1) - q(2)*q(2) + q(3)*q(3) )...
            + 2.0 * q(4) * ( x(2)*q(1) - x(1)*q(2) )...
            + 2.0 * q(3) * ( x(1)*q(1) + x(2)*q(2) ) ;
end


function [rpy]=RotToRPY(R)
    % Abstract: This version of RotToRPY uses the current value of RPY on
    % input to determine which solution to use
    % INPUT: R = 3x3 rotation matrix
    % OUTPUT:   rpy = current 3-vector of roll-pitch-yaw angles (rad)
    % Created by: Craig Carignan

    rpy=[0;0;0];
if(abs(R(3,1) - 1.0) < 0.00000001)
  % Increased the resolution of this test otherwise the move "jumps" at
  % 90 degrees of pitch
% t2 = -90deg:  s2 = -1
% R(0)(1) = - c3 s1 - s3 c1 = - sin(t1+t3)
% R(1)(1) = - s3 s1 + c3 c1 =   cos(t1+t3)
% t1+t3 = atan2(-R(0)(1), R(1)(1))

singular = -1;
rpy(2) = -M_PI_2;
rpy(1) = atan2_zeromod(-R(1,2), R(2,2)) - rpy(3);

    else
```

```
% t2 = +90deg:   s2 = +1
% R(0)(1) = c3 s1 - s3 c1 = sin(t1-t3)
% R(1)(1) = s3 s1 + c3 c1 = cos(t1-t3)
% t1-t3 = atan2(R(0)(1), R(1)(1))

if(abs(R(3,1) + 1.0) < 0.00000001)
  % Increased the resolution of this test otherwise the move "jumps" at
  % 90 degrees of pitch
  % pitch is at +90 deg
singular = 1;
rpy(2) = M_PI_2 ;
rpy(1) = atan2_zeromod(R(1,2), R(2,2)) + rpy(3);


         else
% not singular
singular = 0;
c2mag = sqrt(R(1,1) * R(1,1) + R(2,1) * R(2,1));

% calculate positive c2 solution (-pi/2 < t2 < pi/2)
rpy_plus(1) = atan2_zeromod(R(3,2), R(3,3));
rpy_plus(2) = atan2_zeromod(-R(3,1), c2mag);
rpy_plus(3) = atan2_zeromod(R(2,1), R(1,1));

% calculate negative c2 solution (t2 > pi/2 or t2 < -pi/2)
rpy_minus(1) = atan2_zeromod(-R(3,2), -R(3,3));
rpy_minus(2) = atan2_zeromod(-R(3,1), -c2mag);
rpy_minus(3) = atan2_zeromod(-R(2,1), -R(1,1));

% pick solution closest to current value rpy
rpy_plus_error = sqrt((rpy_plus(1) - rpy(1)) * (rpy_plus(1)...
                - rpy(1)) + (rpy_plus(2) - rpy(2)) * (rpy_plus(2) -...
                rpy(2)) + (rpy_plus(3) - rpy(3)) * (rpy_plus(3) - rpy(3)));
rpy_minus_error = sqrt((rpy_minus(1) - rpy(1)) *...
                (rpy_minus(1) - rpy(1)) + (rpy_minus(2) - rpy(2)) *...
                (rpy_minus(2) - rpy(2)) + (rpy_minus(3) - rpy(3)) *...
                (rpy_minus(3) - rpy(3)));

if rpy_plus_error < rpy_minus_error
for i = 1:3,rpy(i) = rpy_plus(i);    end
            else
for i = 1:3,rpy(i) = rpy_minus(i);   end
              end
          end
      end
end
```

C.7 Supplementary Files

```
% Justin Brannan
% University of Maryland, 2014

% File: Supplementary_Files.m

% Abstract:
%   Two additional files used to convert inertia and plot the final
%   satellite state over time


function [inertia_B]=inertia_convert(inertia_A,m,p_AB)
    % Abstract: Finds the inertia in equivalent frame translated using
    % parallel axis theorem
    % Created by: Craig Carignan

rcTrc=p_AB'*p_AB ;
rcrcT=p_AB*p_AB' ;
rcTrcI = rcTrc*eye(3);

mrr=m*(rcTrcI-rcrcT);

inertia_B=inertia_A + mrr;
end


function satplot2(TOTAL,N,dt)
    % Abstract: Plots the state over time in 8 subplots including position,
    % orientation, modal displacements of two appendages and rates
    % Note: need to run satellite6_2DOF.m first, to declare variables
    % Created by: Justin Brannan

    time_ref=(0:N-1)*dt;

    hold on
    subplot(2,4,1), plot(time_ref,TOTAL(1:3,:),'x')
    xlabel 'time';   ylabel 'x veh';  title 'Vehicle Position (m)'
    hold off
```

```
        hold on
        subplot(2,4,2), plot(time_ref,TOTAL(4:7,:),'x')
        xlabel 'time';    title 'Vehicle Orientation'
        ylabel 'q veh'  % (Quat representation of vehicle rotation)
        hold off
        legend ('x-axis', 'y-axis', 'z-axis')

        hold on
        uf_1temp = (TOTAL(14,:)+TOTAL(15,:))*2;    % Convert qf to uf
        subplot(2,4,3), plot(time_ref,uf_1temp,'x')
        xlabel 'time';    ylabel 'uf_1 veh';    title 'Deformed Position uf_1 (m)'
        hold off

        hold on
        uf_2temp = (TOTAL(18,:)+TOTAL(19,:))*2;    % Convert qf to uf
        subplot(2,4,4), plot(time_ref,uf_2temp,'x')
        xlabel 'time';    ylabel 'uf_2 veh';    title 'Deformed Position uf_2 (m)'
        hold off

        hold on
        subplot(2,4,5), plot(time_ref,TOTAL(8:10,:),'x')
        xlabel 'time';    ylabel 'xdot veh';    title 'Vehicle Velocity (m/s)'
        hold off

        hold on
        subplot(2,4,6), plot(time_ref,TOTAL(11:13,:),'x')
        xlabel 'time';    ylabel 'w veh'
        title 'Vehicle Angular Velocity (rad/s)'
        hold off

        hold on
        ufdot_1temp = (TOTAL(16,:)+TOTAL(17,:))*2;    % Convert qfdot to ufdot
        subplot(2,4,7), plot(time_ref,ufdot_1temp,'x')
        xlabel 'time';    ylabel 'ufdot_1 veh'
        title 'Deformed Velocity uf_d_o_t_1 (m/s)'
        hold off

        hold on
        ufdot_2temp = (TOTAL(20,:)+TOTAL(21,:))*2;    % Convert qfdot to ufdot
        subplot(2,4,8), plot(time_ref,ufdot_2temp,'x')
        xlabel 'time';     ylabel 'ufdot_2 veh'
        title 'Deformed Velocity uf_d_o_t_2 (m/s)'
        hold off
end
```

Chapter D: Mathematica Modal Integral Code

```
(* File: Final_2Mode_ConstInt_Calculations_MoreAccurate.nb *)

(* Abstract: Mathematica derivation of constant integral *)
(* terms, to input into ConstantIntegrals6_2DOF *)

(* **********************************************************************

CONSTANT INTEGRAL CALCULATIONS: 2 Modes, 2 Symmetric Appendages

**********************************************************************\
 *)

(* DEFINE MODE SHAPES *)

L = 5; (* The length of a particular appendage *)

(* Describe First Mode Shape of Cantilever Beam *)
\[Lambda] = 1.87510407;
kc = 0.734095514 ;
\[Phi]1 = (Cosh[\[Lambda]*Abs[x]/L] - Cos[\[Lambda]*Abs[x]/L]) -
   kc*(Sinh[\[Lambda]*Abs[x]/L] - Sin[\[Lambda]*Abs[x]/L]) ;

(* Describe Second Mode Shape of Cantilever Beam *)
\[Lambda] = 4.69409113;
kc = 1.018467319;
\[Phi]2 = (Cosh[\[Lambda]*Abs[x]/L] - Cos[\[Lambda]*Abs[x]/L]) -
   kc*(Sinh[\[Lambda]*Abs[x]/L] - Sin[\[Lambda]*Abs[x]/L]) ;


(* DEFINE NEW, 2DOF FUNCTION *)
```

```
CalcConstIntegralExpressions2DOF[uob_, S_] := {
  (* Preliminary Calculations *)
  qf = {{qf1}, {qf2}}; (* Only looking at first 2 modes *)
  qfdot = {{dq1}, {dq2}};
  uf = S.qf;
  uobx = VecCrossProd[uob];
  ufx = VecCrossProd[uf];

  (* MASS MATRIX -- CHANGED FOR 2DOF *)
  IntUoxT = SetPrecision[Integrate[Transpose[uobx], {x, 0, L}], 10];
  IntUfxT = SetPrecision[Integrate[Transpose[ufx], {x, 0, L}], 10];
  IntUox2 = SetPrecision[Integrate[uobx.uobx, {x, 0, L}], 10];
  IntUoxUfx = SetPrecision[Integrate[uobx.ufx, {x, 0, L}], 10];
  IntUfx2 = SetPrecision[Integrate[ufx.ufx, {x, 0, L}], 10];
  IntUoxS = SetPrecision[Integrate[uobx.S, {x, 0, L}], 10];
  IntUfxS = SetPrecision[Integrate[ufx.S, {x, 0, L}], 10];
  IntUo = SetPrecision[Integrate[uob, {x, 0, L}], 10];
  IntUf = SetPrecision[Integrate[uf, {x, 0, L}], 10];
  IntS = SetPrecision[Integrate[S, {x, 0, L}], 10];
  IntSTS = SetPrecision[Integrate[Transpose[S].S, {x, 0, L}], 10];

  (* FORCING VECTOR *)
  Sqfdot = S.qfdot;
  Sqfdotx = VecCrossProd[Sqfdot];
  IntUoxSdqx = SetPrecision[Integrate[uobx.Sqfdotx, {x, 0, L}], 10];
  IntSdqxUox = SetPrecision[Integrate[Sqfdotx.uobx, {x, 0, L}], 10];
  IntSdqxSqx = SetPrecision[Integrate[Sqfdotx.ufx, {x, 0, L}], 10];
  IntSqxSdqx = SetPrecision[Integrate[ufx.Sqfdotx, {x, 0, L}], 10];
  IntSTUo = SetPrecision[Integrate[Transpose[S].uob, {x, 0, L}], 10];
  IntSTUf = SetPrecision[Integrate[Transpose[S].uf, {x, 0, L}], 10];
  IntSTSdq =
  SetPrecision[Integrate[Transpose[S].S.qfdot, {x, 0, L}], 10];

  (* STIFFNESS AND DAMPING *)
  IntD2Phi1 =
  SetPrecision[Integrate[D[D[\[Phi]1]].D[D[\[Phi]1]], {x, 0, L}], 10];
      IntD2Phi2 =
  SetPrecision[Integrate[D[D[\[Phi]2]].D[D[\[Phi]2]], {x, 0, L}], 10];

  (* PRINT RESULTS *)
  Print["IntUoxT = ", MatrixForm[Simplify[IntUoxT]]];
  Print["IntUfxT = ", MatrixForm[Simplify[IntUfxT, L > 0]]];
  Print["IntUox2 = ", MatrixForm[Simplify[IntUox2]]];
  Print["IntUoxUfx = ", MatrixForm[Simplify[IntUoxUfx]]];
  Print["IntUfx2 = ", MatrixForm[Simplify[IntUfx2]]];
```

```
    Print["IntUoxS = ", MatrixForm[Simplify[IntUoxS, L > 0]]];
    Print["IntUfxS = ", MatrixForm[Simplify[IntUfxS, L > 0]]];
    Print["IntUo = ", MatrixForm[Simplify[IntUo]]];
    Print["IntSTS = ", MatrixForm[Simplify[IntSTS, L > 0]]];

    Print["IntUoxSdqx = ", MatrixForm[Simplify[IntUoxSdqx, L > 0]]];
    Print["IntSdqxUox = ", MatrixForm[Simplify[IntSdqxUox, L > 0]]];
    Print["IntSdqxSqx = ", MatrixForm[Simplify[IntSdqxSqx, L > 0]]];
    Print["IntSqxSdqx = ", MatrixForm[Simplify[IntSqxSdqx, L > 0]]];
    Print["IntUf = ", MatrixForm[Simplify[IntUf]]];
    Print["IntS = ", MatrixForm[Simplify[IntS]]];
    Print["IntSTUo = ", MatrixForm[Simplify[IntSTUo, L > 0]]];
    Print["IntSTUf = ", MatrixForm[Simplify[IntSTUf, L > 0]]];
    Print["IntSTSdq = ", MatrixForm[Simplify[IntSTSdq, L > 0]]];

    Print["IntD2Phi1 = ", MatrixForm[Simplify[IntD2Phi1, L > 0]]];
    Print["IntD2Phi2 = ", MatrixForm[Simplify[IntD2Phi2, L > 0]]];
  }


(* TRY NOMINAL EXAMPLE *)
uob2DOF = {{0}, {x}, {0}};  (* Assumes appendage is on y-axis *)
S2DOF = {{0, 0}, {0, 0}, {\[Phi]1, \[Phi]2}};
(* Assumes appendage only flexes in z-direction *)

VecCrossProd[
   x_] := {{0, -x[[3, 1]], x[[2, 1]]}, {x[[3, 1]],
     0, -x[[1, 1]]}, {-x[[2, 1]], x[[1, 1]], 0}};
(* ONLY VALID FOR 3x1 VECTOR INPUTS!! *)

CalcConstIntegralExpressions2DOF[uob2DOF, S2DOF];


(* Now, Calculate Negative appendage case *)

CalcConstIntegralExpressions2DOF[-uob2DOF, S2DOF];


(* TRY NOMINAL EXAMPLE WITH ONLY 1 MODE *)
uob2DOF = {{0}, {x}, {0}};  (* Assumes appendage is on y-axis *)
S2DOF = {{0, 0}, {0, 0}, {\[Phi]1, 0}};
(* Assumes appendage only flexes in z-direction *)

CalcConstIntegralExpressions2DOF[uob2DOF, S2DOF];
```

```
(* TRY NOMINAL EXAMPLE WITH ONLY MODE 2 *)
uob2DOF = {{0}, {x}, {0}};  (* Assumes appendage is on y-axis *)
S2DOF = {{0, 0}, {0, 0}, {0, \[Phi]2}};
(* Assumes appendage only flexes in z-direction *)

CalcConstIntegralExpressions2DOF[uob2DOF, S2DOF];
```

Bibliography

[1] Joanne L. Walsh. Optimization procedure to control the coupling of vibration modes in flexible space structures. NASA Technical Memorandum 89115, NASA Langley Research Center, February 1987.

[2] Scott R. Ploen, Fred Y. Hadaegh, and Daniel P. Scharf. Rigid body equations of motion for modeling and control of spacecraft formations - part 1: Absolute equations of motion. In *Proc. of American Control Conference*, pages 3646–3653, Boston, 2004.

[3] Patrick A. Tobbe Ph.D, Alex L. Matras Ph.D, and Heath E. Wilson. Modeling and simulation of variable mass, flexible structures. AIAA, 1996.

[4] Dario Izzo, Lorenzo Pettazzi, and Chiara Valente. A comparison between models of flexible spacecrafts. Unpublished research paper.

[5] L. Meirovitch and R. D. Quinn. Equations of motion for maneuvering flexible spacecraft. *AIAA Guidance*, 10:453–465, 1987.

[6] Shengjian Bai, Xinsheng Huang, and Yuhao Liu. Dynamic modeling and simulation of a flexible satellite. In *Asia Simulation Conference - 7th International Conference on System Simulation and Scientific Computing*, China, 2008. IEEE.

[7] Ahmed A. Shabana. *Dynamics of Multibody Systems, 3rd Ed.* Cambridge University Press, New York, 2005.

[8] Francesco Schiavo, Luca Vigano, and Gianni Ferretti. Object-oriented modelling of flexible beams. *Multibody System Dynamics*, 15:263–286, 2006.

[9] Kevin A. Ford. *Reorientations of Flexible Spacecraft Using Momentum Exchange Devices*. PhD thesis, Air Force Institute of Technology, 1997.

[10] Anthony Green and Jurek Sasiadek. Dynamics and trajectory tracking control of a two-link robot manipulator. *Journal of Vibration and Control*, 10:1415–1440, 2004.

[11] Masazumi Ueba. Dynamics of an antenna pointing control system with flexible structures. *AIAA Guidance*, 14:1123–1128, 1991.

[12] L. Meirovitch and M. K. Kwak. On the modeling of flexible multi-body systems by the rayleigh-ritz method. AIAA, 1990.

[13] Aravindh Krishnamoorthy and Deepak Menon. Matrix inversion using cholesky decomposition. Unpublished research paper, 2009.

[14] S. Hanagud and S. Sarkar. Problem of the dynamics of a cantilever beam attached to a moving base. *Journal of Guidance Control and Dynamics*, 12:438–441, 1988.

[15] Norman Wereley Ph.D. Vibration and aeroelasticity. Lecture notes, Fall 2011.

[16] John Sudey Jr., Wayne Dellinger, and Make Hagopian. On-orbit jitter performance of the goes spacecraft and instruments. In *Proc. SPIE 2812, GOES-8 and Beyond*, 1996.

[17] Robert Blevins. *Formulas for Natural Frequency and Mode Shape*. Krieger Publishing Company, 2001.

[18] James Wertz, David F. Everett, and Jeffery J. Puschell. *Space Mission Engineering: The New SMAD*. Microcosm Press, 2011.

[19] James Hubbard. Introduction to advanced structural dynamics. Lecture notes, Spring 2014.

[20] Craig Carignan. Dynamic analysis of planar satellite with two flexible appendages. Personal communication, April 2014.

[21] Justin C. Brannan and Craig R. Carignan. Modeling flexible-body dynamics in real-time robotic systems used in satellite servicing simulations. In *AIAA Modeling and Simulation Technologies Conference*, number AIAA 2013-5157, Boston, Aug 2013. AIAA.

[22] Peter Meckl. Robust motion control of flexible systems using feedforward forcing functions. *Control Systems Technology, IEEE*, 2:245–254, 1994.

[23] Boeing. *GOES N Data Book*, 2006. Unpublished work.

[24] J.E. Hubbard. *Spatial Filtering for the Control of Smart Structures: An Introduction*. Springer, 2009.

[25] Badri Shirgur. Fem beam analysis: Sufficient number of elements. Personal communication, 2013.

[26] R. Budynas and K. Nisbett. *Shigley's Mechanical Engineering Design*. Mcgraw-Hill series in mechanical engineering. McGraw-Hill Education, 1977.